공학박사 학위논문

인공신경망 발전량 예측 불확실성을 고려한 가상발전소 모델예측제어

Cost-Optimal Model Predictive Control for Virtual Power Plant with Uncertainty in Neural Network Power Forecasting

2022년 2월

서울대학교 대학원

기계공학부

최 종 우

인공신경망 발전량 예측 불확실성을 고려한 가상발전소 모델예측제어

Cost-Optimal Model Predictive Control for Virtual Power Plant with Uncertainty in Neural Network Power Forecasting

지도교수 차 석 원

이 논문을 공학박사 학위논문으로 제출함
2021년 10월

서울대학교 대학원
기계공학부
최 종 우

최종우의 박사 학위논문을 인준함
2021년 12월

위 원 장	안 성 훈	(인)
부위원장	차 석 원	(인)
위 원	송 한 호	(인)
위 원	윤 용 태	(인)
위 원	이 일 우	(인)

Abstract

This study presents statistical and control analyses for grid resources to enhance the stability and efficiency on their operations. More specifically, this study focuses on cost-optimal model predictive control for a virtual power plant with the uncertainty in neural network power forecasting.

Chapter 2 analyzes the monitoring data of solar photovoltaic power plants (PVs) distributed throughout Korea. Errors within the raw data are categorized according to their causes and symptoms. The effect of typical errors on the statistical analysis is particularly evaluated for a day-ahead hourly PV power forecast study.

Chapter 3 addresses a control strategy for an energy storage system (ESS). A virtual power plant or a microgrid with a commercial building load, PV generation, and ESS charge/discharge operation is targeted as a behind-the-meter consumer-generator. Economic dispatch scheduling problem for the ESS is formulated as a mixed-integer linear program. The main goal of the control problem is optimizing the economic benefit under the time-of-use tariff and future uncertainties. Peak control as a regulation ancillary market service can be also applied during the optimization. The resulting control schedule robustly guarantees the economic benefit even under the forecast uncertainties in load power consumption and PV power generation patterns.

Chapter 4 presents a more specific case of day-ahead hourly ESS scheduling. An integration of a PV and ESS is considered as a control target. Power transactions between the grid and resources are normally settled according to the time-of-use tariff. Additional incentive is provided with respect to the imbalance between the forecasted-scheduled power and actual dispatch power. This incentive policy stands

for the imbalance tariff of a regulation ancillary service market. Accurate forecasting and robust scheduling functions are required for the energy management system to maximize both revenues. The PV power forecast model, which is based on a recurrent neural network, uses a convolutional neural network discriminator to decrease the gap between its open-loop one-step-ahead training and closed-loop multi-step-ahead test dynamics. This generative adversarial network concept for the model training process ensures a stable day-ahead hourly forecast performance. The robust ESS scheduling model handles the remaining forecast error as a box uncertainty set to consider the cost-optimality and cost-robustness of the control schedule. The scheduling model is formulated as a concise mixed-integer linear program to enable fast online optimization with the consideration for both transaction and incentive revenues.

Keywords: energy management, mixed-integer linear programming, neural network, cost-optimization, forecasting, solar photovoltaic power plant, energy storage system.
Student Number: 2019-30142

Table of Contents

List of Figures

List of Tables

Chapter 1

Introduction

The grid is an interconnected group of power lines and associated equipment for moving electrical energy between points of supply and points of consumption [1]. Electrical energy that is generated in the supply side is transmitted and distributed via the grid to be consumed or stored on the demand side. The basic structure of an electrical power grid is presented in Fig. 1.1 [2].

The stability of a grid operation is closely related to the operation of interconnected energy resources. For example, momentary imbalance between the power supply and demand results in a frequency stability problem. The rapid increase of demand that exceeds the active power supply induces a downward drift of the grid

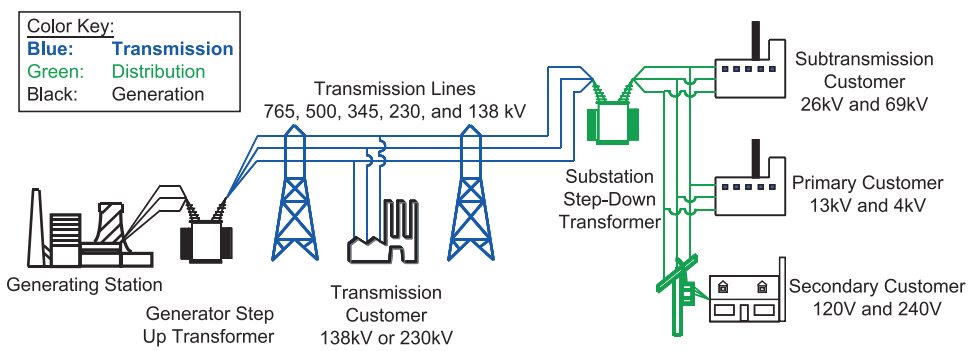

Figure 1.1: Basic structure of an U.S. electrical power grid [2].

frequency [3] because of the inversely proportional speed-load curves of synchronous generators [4]. Conversely, the oversupply of power by distributed energy resources (DERs) results in a voltage stability problem; an overvoltage is applied at the point of a DER connection to export remaining power as a reverse power flow [5, 6].

The grid of today faces an increasing penetration of DERs driven by the needs of reduced line losses [7], sustainable generation [8], energy bill management on the consumer side, and reliable power supply for the fault protection [9]. Despite these advantages, the increasing penetration of DERs requires complicated considerations for the grid management. In case of the frequency stability, conventional synchronous generators, i.e., motor-based generators that convert mechanical power into electrical one, help decrease the amount of frequency drift with their high inertia. However, they are largely displaced with power electronics-based generators such as solar photovoltaic power plants (PVs) with DC-to-AC inverters and wind turbine plants (WTs) with back-to-back AC-to-AC converters. To compensate the grid inertia for these inertia-less generators, additional equipment such as a synchronous condenser with a rotating motor [10] is required for the grid management.

The increasing penetration of variable renewable energy resources (VREs) such as PVs and WTs also becomes a crucial problem for grid power balancing. The grid operator has to manage dispatchable generators to match the power supply with the varying power demand. However, VREs are generally operated in a non-dispatchable manner. In case of a grid with large PVs, the daily peak power occurs at noon, while the daily peak demand occurs in the evening. This peak power imbalance is known as duck curve [11]. The effect of weather conditions on the power generation capacity is also a well-known problem for VREs. A grid with a large VRE penetration even

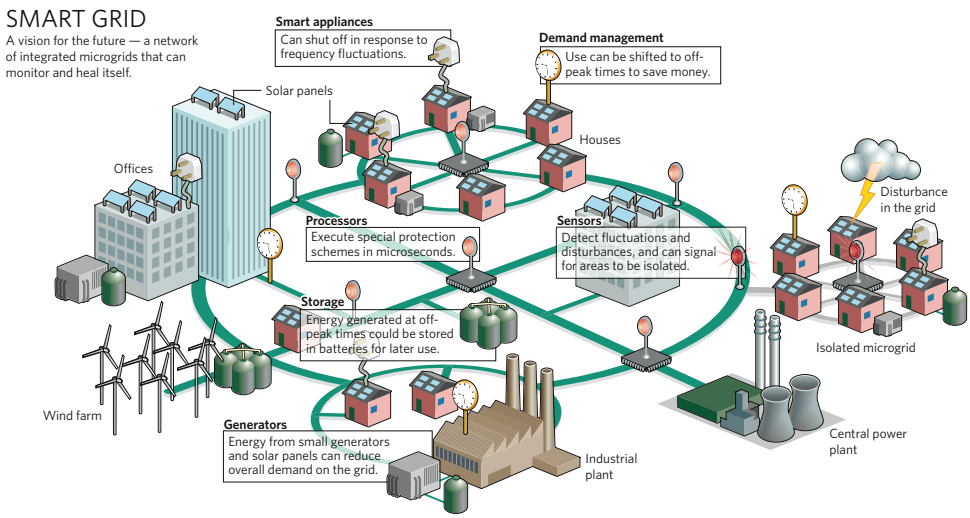

Figure 1.2: The concept of a smart grid [13].

faces new types of threats on the supply side such as a solar eclipse for PVs [12] and strong wind for WTs.

Communications and interactions between the demand and supply sides are encouraged for a grid to achieve opportunities for controlling possible instabilities. The concept of a smart grid, which is presented in Fig. 1.2, has its basis on these two operations. According to the definition of the European Commision, a smart grid is an electricity network that can integrate the actions of all users, including generators, consumers (customers), and customer-generators [14]. It aims to provide an economically efficient, sustainable system with the consideration for the power quality and safety. The Energy Independence and Security Act of the United States Congress in 2007 identifies the smart grid as a modernized version of the transmission and distribution system with the consideration for the reliability and safety [15]. Specific characteristics for a smart grid are also defined: DER deployments, increased use of digital information, and dynamic optimization for grid operations and resources.

The introduction of a smart grid with the increased deployment of DERs and their control technologies provides an opportunity to enhance the management for a grid through market-based approaches. This concept is known as transactive energy [16]. Transactive energy refers to a combination of economic and control approaches for the reliability and efficiency of the grid operation [17]. Transactive energy is not a new concept because of the traditional power market and other policies such as power purchase agreement, time-of-use tariff, and net energy metering; it rather stands for the existence of traditional approaches and possibilities for future approaches. Economic constructs for transactive energy and a smart grid, or a traditional grid that are related to this study are follows:

- Electricity market, a.k.a. power exchange, is a system that enables to purchase or sell electricity. A wholesale market uses a contract-based predefined price or an auction-based clearing price to settle the trades between generators and resellers. Trades between a reseller and its consumers are proceed within a retail market. In case of a grid with many resellers, consumers can choose their resellers, i.e., retail electricity providers, according to power purchasing options that are provided by resellers [18].

- Time-of-use tariff refers to a policy in a retail market to charge the electricity use with different prices for each hour of the day. A price schedule is generally determined according to the peak and off-peak hours [19], or can be a dynamic one as real-time pricing [20]. Customers under the time-of-use tariff may shift their non-critical power usage for off-peak hours, thereby contributing the grid stability. Consequently, time-of-use tariff can be classified as a demand response strategy that uses the price as a control signal [20].

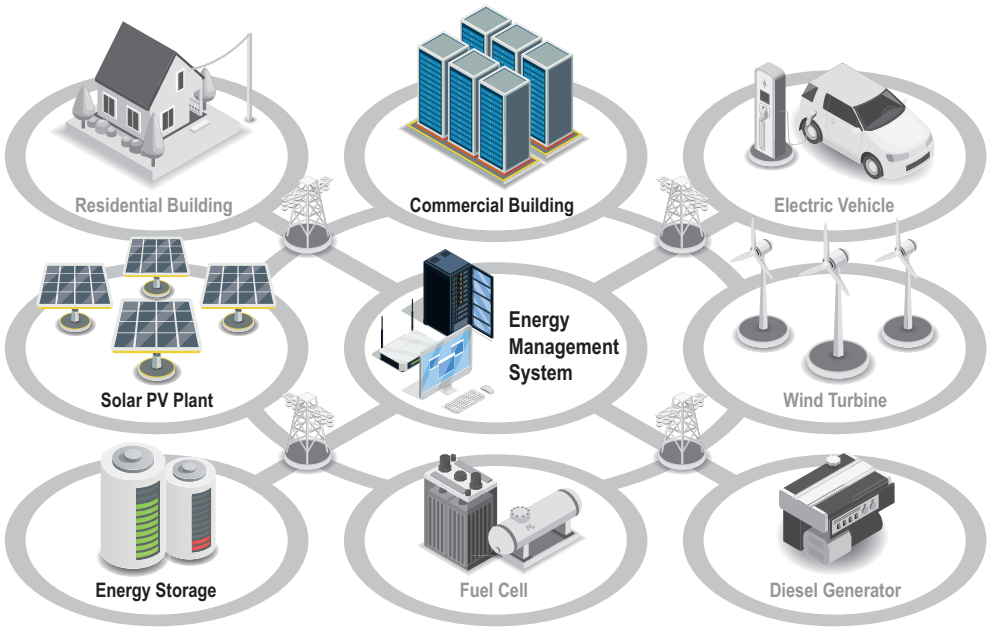

Figure 1.3: Distributed energy resources with their energy management system.

- Grid ancillary services are a set of special grid services beyond generation and transmission [21]. They are procured by transmission or distribution system operators [22] to support stable operations of the electricity network. Ancillary services may include regulation and reserve markets to compensate small-scale and large-scale power imbalances, respectively [23]. Dispatchable DERs and demand-response resources can participate an ancillary service market to achieve economic benefits by providing proper services.

This study presents statistical and control analyses for grid resources to enhance the stability and efficiency on their operations. Loads and DERs that are focused in this study are presented in Fig. 1.3. The result of this study would help to develop an energy management system (EMS) for DERs within or without a smart grid.

Chapter 2 analyzes the monitoring data of PVs distributed throughout Korea.

Errors within the raw data are categorized according to their causes and symptoms. The effect of typical errors on the statistical analysis is particularly evaluated for a day-ahead hourly PV power forecast study.

Chapter 3 addresses a control strategy for an energy storage system (ESS). A virtual power plant or a microgrid with a commercial building load, PV generation, and ESS charge/discharge operation is targeted as a behind-the-meter consumer-generator. Economic dispatch scheduling (planning) problem for the ESS is formulated as a mixed-integer linear program. The main goal of the control problem is optimizing the economic benefit under the time-of-use tariff. Peak control as a regulation ancillary market service can be also applied during the optimization. The resulting control schedule robustly guarantees the economic benefit even under the forecast uncertainties in load power consumption and PV power generation patterns.

Chapter 4 presents a more specific case of day-ahead hourly ESS scheduling. An integration of a PV and ESS is considered as a control target. Power transactions between the grid and resources are normally settled according to the time-of-use tariff. Additional incentive is provided with respect to the imbalance between the forecasted-scheduled power and actual dispatch power. This incentive policy stands for the imbalance tariff of a regulation ancillary service market. The EMS requires accurate forecasting and robust scheduling functions to maximize both revenues. The PV power forecast model, which is based on a recurrent neural network, uses a convolutional neural network discriminator to decrease the gap between its open-loop one-step-ahead training and closed-loop multi-step-ahead test dynamics. The application of this generative adversarial network concept to the model training process ensures a stable day-ahead hourly forecast performance. The robust ESS scheduling

model handles the remaining forecast error as a box uncertainty set to consider the cost-optimality and cost-robustness of the control schedule. The scheduling model is formulated as a concise mixed-integer linear program to enable fast online optimization with the consideration for both transaction and incentive revenues.

Chapter 2

Analysis of Data Errors in the Solar Photovoltaic Power Plant Monitoring System Database

Management services for solar photovoltaic power plants (PVs) have become an important issue in today's era of increasing PV installations. The existence of error-free data is necessary for data-driven PV management; however, real-world data contain an unignorable portion of errors, thereby reducing the reliability of corresponding analyses. A report on the plausible errors within the data is necessary to help PV administrators configure proper data cleaning algorithms. This study provides an error case report derived from an analysis of nearly 2,000 PVs distributed throughout Korea. Real error cases are categorized according to their causes and symptoms. The effect of typical errors on the data-driven PV analysis is particularly evaluated for the day-ahead hourly PV power forecast. Errors in the system specification data significantly decrease the forecast accuracy, thereby addressing the impact of human errors. Regression imputation in the time domain demonstrates acceptable results as a simple ad-hoc method in most error situations.

2.1 Background

Solar photovoltaic power plants (PVs) have been widely installed with support from various public policies that encourage sustainable production of energy [24, 25, 26, 27]. Many governments have tried to replace traditional power plants with PVs because they are simple to install [28], have carbon-free operation [29], and are sustainable [8]. However, the increase in PV installation has also aroused debates regarding the tradeoff between their environmental effect and economic feasibility [30].

Operation and maintenance (O&M) services for a PV can be a solution to enhance economic feasibility while conserving the environmental advantages. Real-time monitoring of a PV is considered as a minimal version of the O&M service. Fault detection and diagnosis using the monitoring data helps the PV administrator to deal with major failures in real time, thereby maintaining the system performance within an allowable level [31, 32]. Although the installation and operation costs of monitoring devices negatively affect plant economics [32, 33, 34, 35], the expected benefit tends to be higher than its introduction cost [31].

The reliability of data is an important issue to be considered prior to introducing an O&M service. The performance of a PV can be correctly analyzed only with reliable data. PV analyses such as economic dispatch [36, 37], power forecasting [38, 39, 40], fault and electricity theft detection [32, 40, 41, 42, 43] are mostly performed using data-driven approaches. It is inherently assumed that the data used for deciding control strategies, learning artificial neural networks, or developing detection rules are error-free. However, real-world data may contain an unignorable portion of complex errors that are difficult to be identified by simple filtering. Even in the medical field, several studies have found that medical data, directly related to human

health, contain many types of errors such as duplication, inconsistency, unclearness, and programming inaccuracies [44, 45]. Although it is a reasonable assumption that industrial data contain more errors than medical ones, only a few studies have focused on the reliability of meter data [46, 47, 48, 49, 50, 51, 52].

This chapter provides a simplified version of the white paper on PV data errors, particularly those that are closely related to the monitoring process. Real-time monitoring of a PV suffers from various problems caused by hardware, software, and human issues. Missing data is a common symptom for these problems. Engineers in the real world try to identify and fix the cause of a problem with their empirical knowledge. Although some of the issues can be typical among PVs, it is difficult to find a generalized error-handling document because of the lack of error cases for each plant and the reluctance to share data among plant owners. An analysis of dozens or hundreds of systems is insufficient to create such documents. To deal with insufficient error data, a massive monitoring system for PVs is developed in this project.

The monitoring system of this project has collected data from nearly 2,000 PVs nationwide in South Korea. The errors that were found during operation are categorized according to their causes and symptoms. Data communication problems are identified as typical errors among PVs, thereby disrupting the continuity of time-series data. Errors within system specification information data are also found for some PVs. The results suggest that human or system errors are not seriously concerned by PV administrators.

This chapter also evaluates the effect of typical errors on the PV study, particularly for the PV power forecast study using statistical models. The parameters of a statistical model can be accurately and robustly estimated only if there is a suf-

ficient amount of error-free historical data [53]. Data cleaning [54] and imputation [55] during data preprocessing are essential for such data-driven approaches to remedy the effect of errors within the training data. The exclusion of multivariate error records, which is known as list-wise deletion or complete-case analysis, is the simplest cleaning method but it reduces the data size and corresponding statistical power [55, 56, 57]. Substituting the error value with a reasonable one may produce a better result. Several imputation methods were tested to prepare error-free training data for the data-driven PV power forecast study. Regression imputation in the time domain demonstrated good results as a simple ad-hoc method in most monitoring data error situations. The results will provide insights for PV administrators who decide to introduce their own monitoring systems along with error handling algorithms.

The remainder of this chapter is organized as follows. General policies and statistics for the PVs in Korea are briefly described in Section 2.2. An overview of the PVs analyzed in this study is provided in Section 2.3. Analyses of the errors found within the monitoring system database are presented in Sections 2.4 and 2.5, depending on the data type. The effect of errors on the PV power forecast study is analyzed in Section 2.6. The chapter summary is presented in Section 2.7.

2.2 Solar Photovoltaic Power Plants in Korea

The increase in PVs and other renewable power plants has been promoted in Korea through national policies ranging from *Alternative Energy Development Promotion Act 1987* [58] to *The Third National Energy Master Plan 2019* [59]. The latest policy aims to supply 30%–35% of national electric power by renewable sources by 2040. With the help of government support, the power supplied by PVs increased from

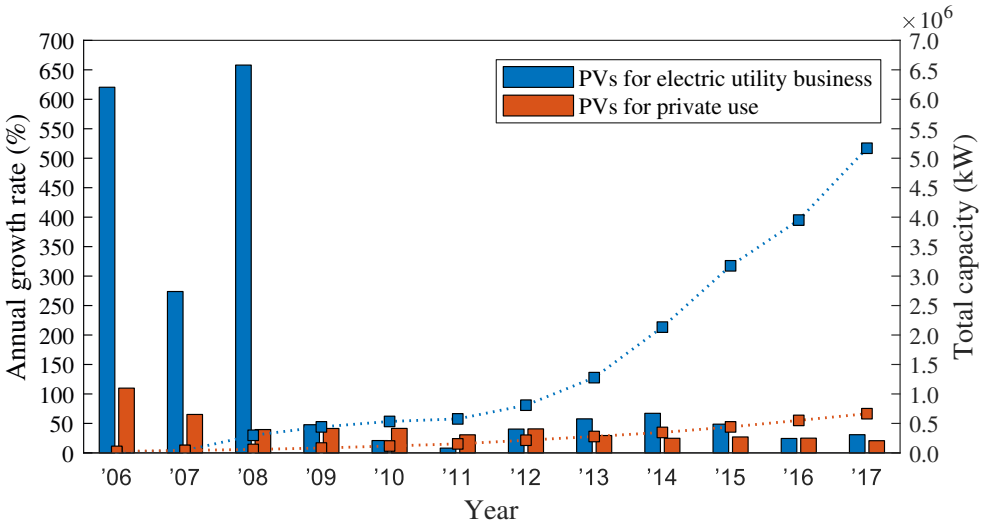

Figure 2.1: Annual growth of solar photovoltaic power plant (PV) power generation capacities in Korea.

7.0 GWh to 7,056.2 GWh between 2002 and 2017 [60]. The annual growth of PV installations as their total installed power capacity [61] is presented in Fig. 2.1.

There are around 386,000–430,000 PVs in Korea, according to government announcements in 2018 [62, 63]. Each PV is classified into one of three categories depending on its size and purpose [64]. PVs *for electric utility business*, i.e., plants that sell their power to the national electricity market, are nationally managed by the Korea Power Exchange, the market operator. The exact number of these large-scale PVs is 30,271 [62]. PVs *for private use*, i.e., plants with the primary goal of supporting private facilities, are managed by the Korea Electric Power Corporation, the operator of the national electric sales business. There are 356,195 plants of this type [62]. The remaining small-scale PVs are classified as those *for general use*. Their numbers are roughly estimated to be 1000–110,000 [65, 66]. A summary of legal classifications and the following statistics are presented in Table 2.1.

Table 2.1: Legal Classifications and Statistics of PVs in Korea

Classification	Capacity	Cash balancing with			Numbers (ea)
		Electricity Market	Power Purchase Agreement	Net Metering	
For electric utility business	> 1 MW	Mandatory	Impossible	Impossible	30,271
	≤ 1 MW	Possible	Possible	Impossible	
For private use	> 1 MW	Possible[a]	Impossible	Impossible	356,195
	≤ 1 MW	Possible[a]	Possible[a]	Possible[b,c]	
For general use	≤ 10 kW	Impossible	Impossible	Possible[b]	$\sim$110,000

[a] Balancing is allowed only for the excess power after private use.

[b] Net excess generation is carried forward to the next month.

[c] Net excess generation can be redeemed under a fixed unit price.

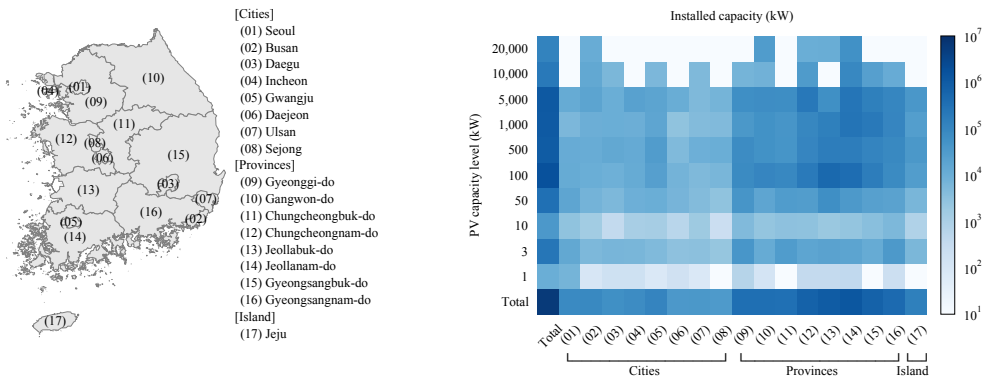

Figure 2.2: Capacity distribution of PVs by region and capacity level (2017).

The distribution of PVs by region and capacity level [67] is presented in Fig. 2.2. Most power generation capacities are located in the flat regions of the south where there is high solar irradiance but low population density. PVs with capacities ranging 50–100 kW make up 29.3% of the total installed capacity, which implies a significant number of small-scale plants.

2.3 Solar Photovoltaic Power Plants for Analysis

Figure 2.3: Web-based user interface of the monitoring system for nationwide PVs.

This study was conducted for a project to develop a unified monitoring system for PVs in Korea, as presented in Fig. 2.3. It has an internal goal of accommodating 1% of nationwide PVs to the system. PVs participating in this project had reached nearly 2,000 in number, 0.5% of the total in mid-2019. Most of them are small- and mid-scale PVs with capacities lower than 1 MW, and it is economically infeasible for them to have their own monitoring systems. Meanwhile, large-scale ones for electric utility business or private use tend to have their own management systems because they have a duty to interact with public or governmental systems. Consequently, only 3.5% of the participating PVs have a capacity higher than 1 MW.

The spatial distribution of monitoring PVs, as presented in Fig. 2.4, is not concentrated in high solar irradiance regions; both nationwide and monitoring PVs have

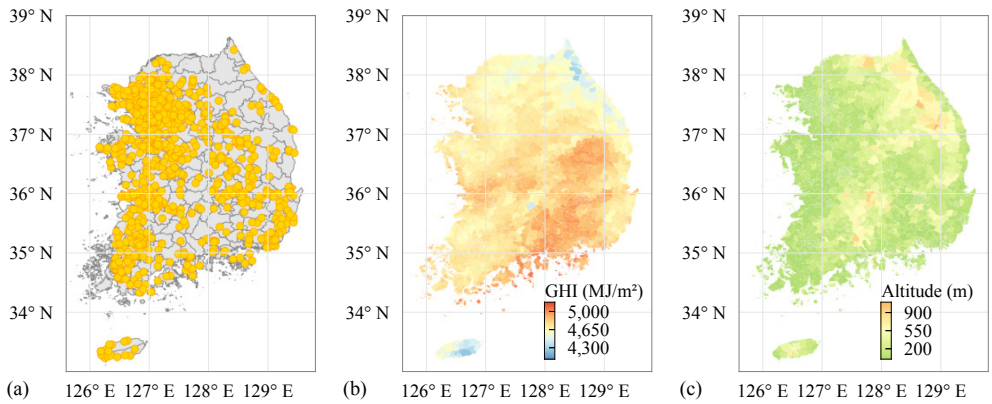

Figure 2.4: Spatial distribution of monitoring PVs and geographical conditions. (a) Locations of the PVs. (b) Annual sum of global horizontal irradiance provided by the Korea Meteorological Administration in 2010. (c) Altitude of the Korean Peninsula provided by the National Spatial Data Infrastructure Portal of Korea in 2015.

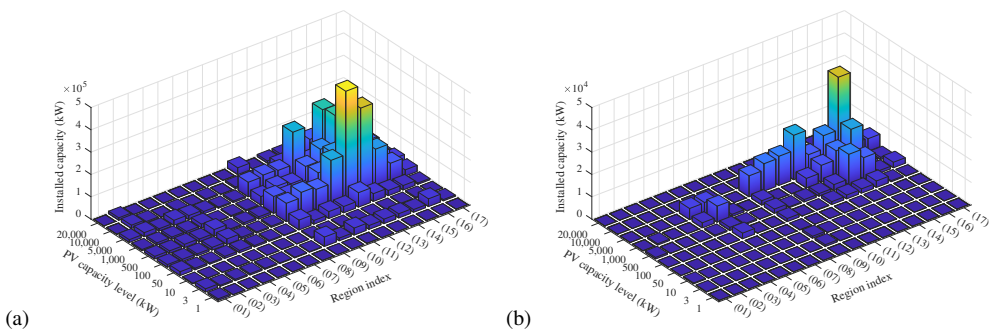

Figure 2.5: Capacity distribution of PVs by region and capacity level. (a) Nationwide plants (2017). (b) Monitoring plants.

a wide spatial distribution to avoid mountainous terrains of the Korean Peninsula. A comparison between the distributions of nationwide and monitoring PVs is presented in Fig. 2.5. The notable difference, shown by a sharp peak, is caused by the limited number and distribution of large-scale PVs participating in the project. Without this difference, both distributions show similar concentrations in rural regions, between the ninth and sixteenth, as mid-scale PVs.

The monitoring system provides a representational state transfer application programming interface (API) to collect data from remote PVs. PV administrators can freely send their facility data (e.g. inverter power or status ones) through the API if they want. Any privacy information is not collected by the API nor the monitoring system. Moreover, the researchers of this study strictly agreed not to discuss sensitive information such as degradations or failures on each PV. In accordance with the agreement, this study only addresses the data errors that are identified during the development and analysis of the monitoring system.

2.4 Errors in Static Information Data

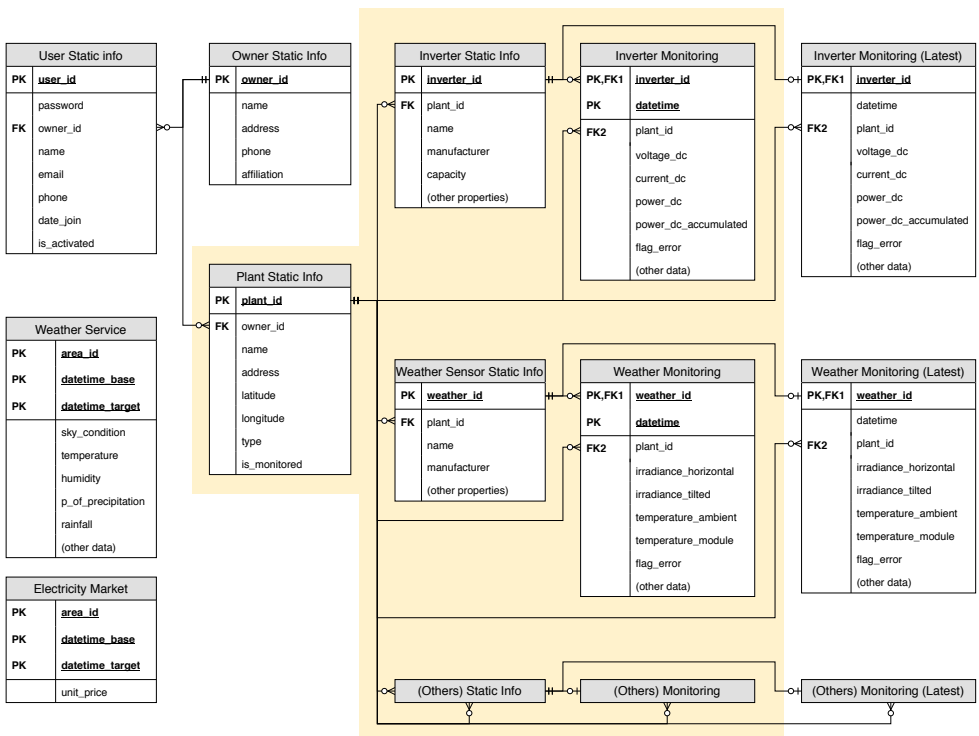

Figure 2.6: Physical entity-relationship diagram for the relational database schema of the developed monitoring system.

Table 2.2: Summary for the Data Stored in the Monitoring System Database

Data Classification	Volume		Inserted Rows	
	(MiB)	(%)	Total (thousands)	Max. Growth Rate (thousands per day)
Static information	2.56	0.0026	16.77	-
Monitoring data	60,113.75	61.58	226,786.83	652.66
Internal service	6,871.05	7.04	38,697.85	154.20
External service	30,625.59	31.37	79,362.99	358.16
Others	2.64	0.0027	19.99	-
Total	97,615.59	100.00	344,884.42	1,165.02

The monitoring system developed in this project manages each PV and its facilities as individual objects with associations, which is a common concept for relational databases. Each object registers its specification information to the system database as static data. Static information data of a PV object include information about the location, capacity, owner, legal classification, and monitoring data transmission period. Static information data of a facility object include information regarding facility type, manufacturer, installed date, and facility-specific data such as efficiency, operation range, and monitoring data resolution.

The monitoring system assigns a unique identifier to each object that has been registered. Facility objects additionally take the identifier of their parent PV object. A physical entity–relational diagram [68] for the relational database schema of the system is presented in Fig. 2.6. Static and monitoring data tables are highlighted in yellow. The system matches the identifiers in the static and monitoring data tables to find plant and facility objects associated with the received monitoring data. Insertion of a duplicated record [51] for both the static and monitoring data is systematically

prevented by unique primary keys including identifiers and datetime.

The monitoring system database also contains tables for internal system operations, such as the latest monitoring data table for the user interface, and those for external system interactions, such as national weather service and electricity market data tables. The total volume of the database reached 95.3 GiB from June 2018 to August 2019. Table 2.2 summarizes the statistics of the data stored in the database. The total volume of the real-time monitoring data consistently grows at a maximum rate of 652,000 rows per day, roughly 173 MiB. Static information data, occupying only a small amount of volume, are first analyzed. A flowchart for the error identification process is presented in Fig. 2.7.

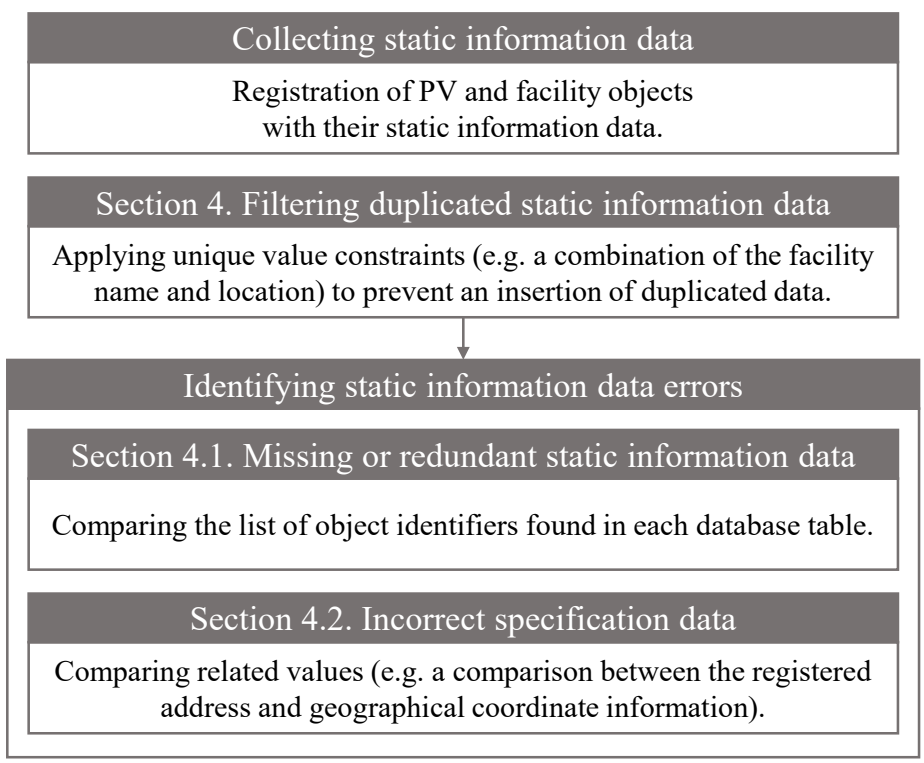

Figure 2.7: Error identification process for the static information data.

2.4.1 Errors: Missing or Redundant Static Information Data

Table 2.3: Number of Distinct PV Identifiers in Static and Monitoring Data Tables

Static Data Table		PV Monitoring Data Existence Level (ea)				
PV	Inverter	0	100	1,000	$>$ 1,000	Total
Found	Found	4	1	1	1,866	1,872
Found	Missing	11	-	-	1	12
Missing	Found	-	-	-	1	1
Missing	Missing	-	7	2	57	66
Total		15	8	3	1,925	1,951

There are 1,951 PVs, 3,150 inverters, and other facilities registered in the monitoring system. Registration and deregistration of PV or facility objects commonly occur during monitoring system operation. Although most of these processes are performed as expected, they sometimes comprise errors because of connection timeout or invalid request parameters. Furthermore, some PV administrators forget to register/deregister their PVs and just start/stop sending the monitoring data to the system.

The monitoring system can have a functionality of registering a missing object with expected static information. However, the result may be meaningless without the official confirmation. Automatic deregistration of a long-term disconnected object is also discouraged; it results in cascade deletion of static information and monitoring data without an approval. Consequently, the monitoring system of this study just warns about missing or redundant objects without altering their data.

Missing or redundant static information as a result of improper registration was checked by comparing the distinct identifiers in the PV static data, inverter static data, and inverter monitoring data tables. A summary of this comparison is presented

in Table 2.3. Missing PV static data was found for 67 identifiers; 9 of which with less than a thousand monitoring data were considered as system testing data. 17 registered PV objects were assumed to be redundant owing to the same reason. One additional PV was identified as the one just missed the inverter static information.

2.4.2 Errors: Incorrect Specification Data

Specification data, which are necessary to register an object to the monitoring system, are mostly collected and inserted manually by PV administrators. The resulting data can suffer from value errors because of the risk of inaccuracy in human processes: i.e., mistyping, referencing outdated documents, or misunderstanding of the facility. Although some systematic solutions such as cyber-physical systems enable the automatic creation of static information, they are only applicable to vendor-specific devices. In most cases, double-checking the collected and registered data is the only way to determine the existence of value errors.

Three types of double-checking were performed using the registered data. A comparison between the registered address and geographical coordinate information found 14 PV objects with conflicting data. Introducing the national address database additionally found two typos in the registered address information. Facility identifiers, which are assigned to reflect facility type and parent PV information, were checked again with the parent PV identifier; a conflict within one PV object was found within a few seconds. This concept of joint information for the facility identifier definition is particularly useful as the size of the database increases.

2.5 Errors in Monitoring Data

The monitoring system uses a wide area network to collect data from PVs distributed throughout South Korea. Long-range data transmission from a remote PV to the monitoring system has an inherent risk of being halted or corrupted by various systematic or environmental issues. The resulting errors in the monitoring data can be categorized as value or communication errors. A flowchart for the error identification process is presented in Fig. 2.8.

2.5.1 Errors: Invalid Peak Power Values

Value errors, denote invalid or incorrect data values, are often caused by faults in measurement devices or their installations. In case of an electromechanical watt-hour meter [69], dirt on the disk or bearing will cause a bias error by introducing friction

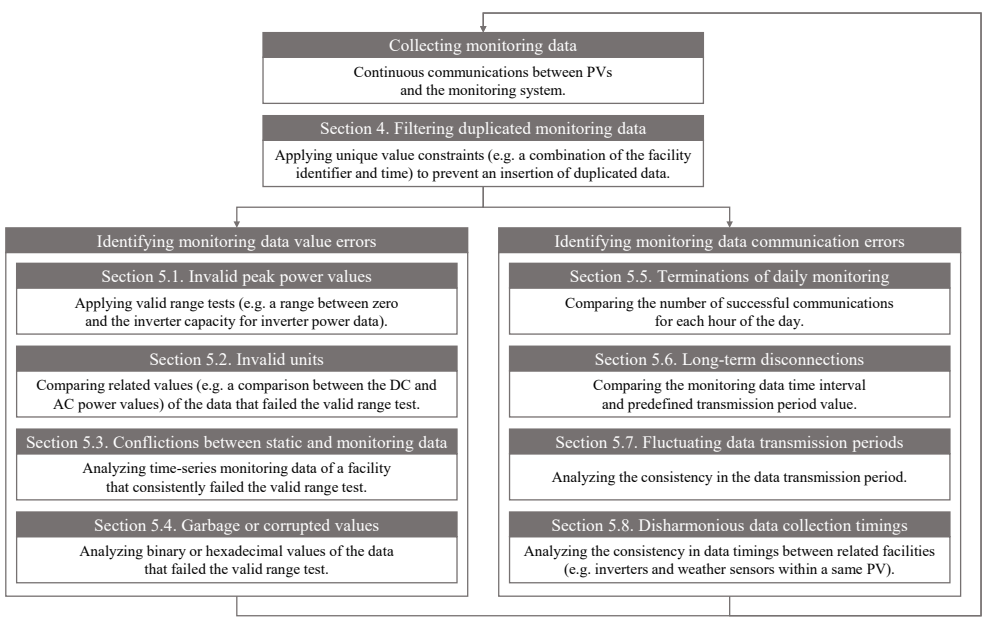

Figure 2.8: Error identification process for the monitoring data.

Table 2.4: Statistics for the Intermittent Peak Power Value error

Error Rate	PV Capacity Level (kW)				Total	
(%)	10	100	1,000	10,000	(ea)	(%)
0.0	79	36	75	12	202	10.96
0.1	1,235	108	128	52	1,524	82.64
0.2	89	6	6	1	102	5.53
1.0	13	-	-	-	13	0.71
10.0	3	-	-	-	3	0.16
Total	1,419	150	209	65	1,843	100.00

to the disk rotation. Vibration of the meter mounting point, which can be occurred by wind or facility operation, may cause a variance error. A data acquisition system can also generate garbage or corrupted values as described in Section 2.5.4.

The detection of a value error is difficult in most cases because the real value is unknown. Duplicate installation of measurement devices for each monitoring data can be a solution, but is unrealistic. A plausible alternative for error detection is the use of the known distribution of the data.

The PV power generation data have a valid value range between zero and its capacity. Measurement failures, often caused by electrical sparks or foreign matter on electrometers, can result in values that exceed the valid range. Such intermittent peak value errors were analyzed for 1,866 normally monitored PVs that are free from missing and redundant static information errors, as shown in Table 2.3. During the analysis, 23 PVs were excluded because they exhibited more serious problems, which are described in the following subsections 2.5.2–2.5.4.

The analysis results for the power value error are presented in Table 2.4. A total of 99.1% of PVs had a negligible error rate, lower than 0.2%. Only three small PVs

suffered from high error rates of 5.65%, 7.06%, and 9.47%. All three have inverters that only measure accumulated generation values; their operators then manually developed software to calculate hourly averaged power values and send them to the monitoring system. The comparison between the accumulated and calculated power data identified bugs in the calculation algorithm that caused the errors.

2.5.2 Errors: Invalid Units

Although the monitoring system officially accepts kW-unit data, some PVs were identified as sending W-unit data. Most of them even use different units for DC, AC, and accumulated power values. The monitoring system has an internal logic to handle this problem because it was expected during the system design. However, a comparison between the capacity and monitoring data found eight PVs with 100 W-unit data, which were not expected. The invalid unit error of this type may lead to a serious economic feasibility problem: the monitoring data multiplied by ten can make the owner of a low-performance PV believe its normal operation.

2.5.3 Errors: Conflictions Between Static and Monitoring Data

Conflictions within the static information of a PV has been analyzed in Section 2.4.2. A comparison between the capacity information and real-time monitoring data additionally found eight PVs that continuously generate higher power than their capacities. Two of these with deviations of less than a kW are believed to have inverters with unreported capacity margins, as shown in Fig. 2.9. Another six of these PVs registered invalid capacity information; for example, one PV with two inverters registered swapped capacities to the system.

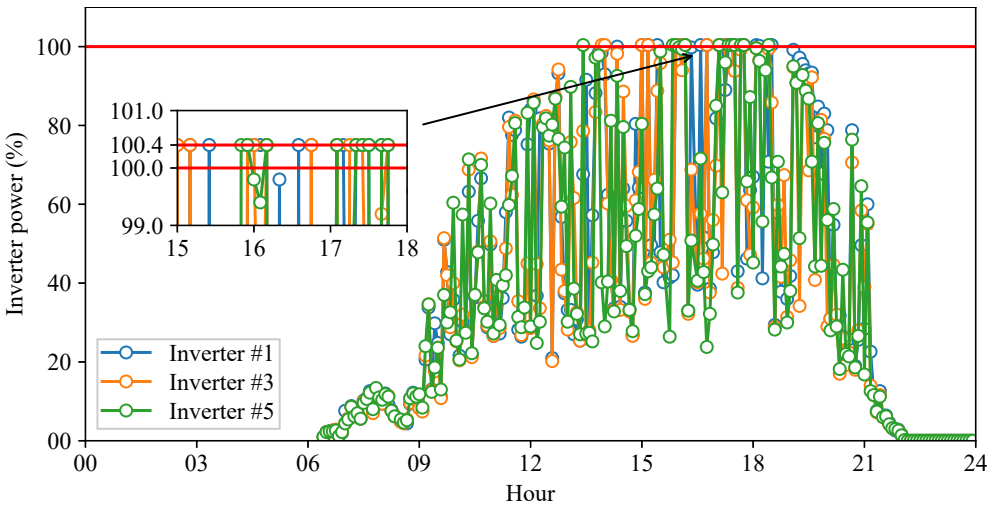

Figure 2.9: PV power generation with an unreported capacity margin.

2.5.4 Errors: Garbage or Corrupted Values

Garbage or corrupted values in data occur as a result of invalid memory operation in computer engineering. Accessing an unallocated memory address, possible in a low-level programming language like C, causes an undefined behavior [70, 71] including uninitialized garbage value return. Moreover, buffer [72] or integer overflows [73], well-known buggy conditions in backend software such as communication device firmware, result in corrupted values for not only the target data but also nearby data.

Three types of memory-related error values were found within the database, particularly for eight PVs managed by the same company. Five of these sent a value of 65,535 during night hours, which is equal to the maximum value of the unsigned 16-bit short integer 0xffff. Another PV sent the maximum value of the unsigned 24-bit integer 0xffffff, 16,777,215. It is expected that their inverters do not assign values to the memory if no power is generated, whereas communication firmware tries to send the memory value. The remaining two plants, including the one also presented an

Table 2.5: Reset of Accumulated Power Generation Value

Datetime	DC Power (kW)	AC Power (kW)	Accumulated Generation (kWh)
2019-04-14 11:55:00	251.8	243.4	4,294,898.0
2019-04-14 12:00:00	275.2	267.0	4,294,919.5
2019-04-14 12:05:00	311.4	301.3	4,294,944.5
2019-04-14 12:10:00	221.3	213.6	0.204
2019-04-14 12:15:00	166.7	161.5	16.704
2019-04-14 12:20:00	134.0	129.7	29.204
2019-04-14 12:25:00	93.7	90.5	38.204
2019-04-14 12:30:00	47.5	45.8	43.204
2019-04-14 12:35:00	39.6	38.0	46.704
2019-04-14 12:40:00	47.4	44.8	52.704

invalid capacity problem, showed some corrupted values higher than their capacities. Firmware bugs, such as accessing incorrect memory addresses or memory overflows, were suspected as the reason behind these errors. Garbage or corrupted values corresponding to these errors can also be zeros [51] or replications of the last valid values depending on firmware logic.

One additional error was found for some inverters with accumulation (watt-hour) meters. Because the accumulated power generation in time has a non-decreasing value, the meter should reset its value after an interval of time to avoid overflows. The time to reset is presented in Table 2.5. The accumulated power generation value was reset near the maximum value of the unsigned 32-bit long integer 0xffffffff, 4,294,967,295, divided by one thousand. Corruption in the accumulated value occurred during reset: an unknown value 0xcc, 204, divided by one thousand, was continuously added to the value after the reset.

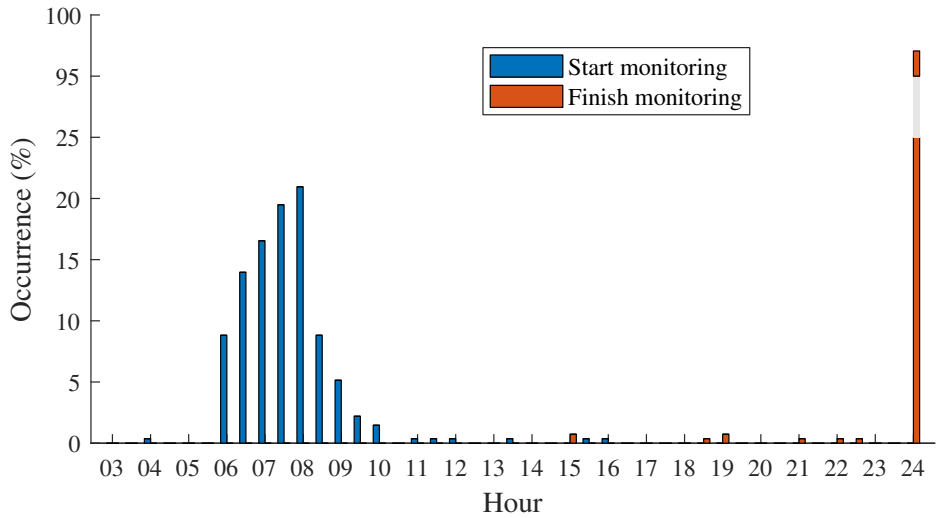

Figure 2.10: Distribution of manually controlled start and finish time for daily monitoring of one PV.

2.5.5 Errors: Terminations of Daily Monitoring

Continuous communications for real-time PV monitoring were occasionally disconnected owing to various software and hardware problems, including processing timeout, power outage, and device replacement. Missing data as a result of the disconnection is undesirable because it disrupts the continuity of time-series data. However, even manual termination of the monitoring process was observed among PVs.

Large-scale PVs tend to maintain the monitoring service the whole day because the prevention of plant failure has a higher priority than the saving of a small portion of the energy used by monitoring devices. By contrast, small-scale PVs may decide to turn off their monitoring devices during midnight hours to reduce energy consumption and enhance economic feasibility. Further, some PVs provide the power for monitoring devices through their own generation; monitoring at night or cloudy hours is physically impossible in such cases.

Table 2.6: Statistics for the Missing of Monitoring Data in Night Hours

Missing Ratio	PV Capacity Level (kW)				Total	
(%)	10	100	1,000	10,000	(ea)	(%)
5	5	120	143	65	333	17.85
10	1	4	1	-	6	0.32
20	7	-	-	-	7	0.38
30	809	2	1	-	812	43.52
40	596	-	-	-	596	31.94
100	1	30	77	4	112	6.00
Total	1,419	156	222	69	1,866	100.00

A real-world example of the manual termination of PV monitoring is presented in Fig. 2.10. The termination time was mostly observed at five to midnight; while the restart time was widely distributed in each day morning. Changes in human behavior or device startup duration may cause such variations.

Statistics for the missing monitoring data at night are presented in Table 2.6. Most small-scale PVs terminated monitoring during night hours. Completely missing night data for some mid- and large-scale PVs imply that these PVs are systematically controlled by the administrators to terminate monitoring in idle hours.

2.5.6 Errors: Long-term Disconnections

Most intermittent disconnections in monitoring can be recovered within a short time after their causes are removed by themselves. A simple iterative loop with exception handling is sufficient for the monitoring system to retry disconnected communications. The automatic restart function of the monitoring device is also helpful in dealing with power or firmware failures.

Disconnections that last more than a week are classified as long-term ones in this study. These are caused by unexpected serious system failures. For example, several monitoring devices in the real world experienced issues related to a lack of firmware memory because of rapidly increasing log file sizes. Some of them took a week to find these unexpected failures and recover normal communications. Analysis of the monitoring database found that 1,858 out of 1,866 PVs suffered from long-term disconnections at least once during their operations.

The longest disconnection found in the database lasted 134 days, roughly one-third of a year. However, approximately 60% of disconnections were solved by the operator within 10 days; whereas 99.5% of the disconnections were solved within 35 days, which is approximately a month.

2.5.7 Errors: Fluctuating Data Transmission Periods

Continuous communications between PVs and the monitoring system are established by a periodic data transmission. Each PV has its own data transmission period of 5–60 min. The length of the transmission period defines the tradeoff between the system load and data quality; a long period results in insufficient data resolution but decreases the system network and storage loads. Changing the period length has to be done after serious deliberations because it breaks the consistency between the preceding and succeeding data. Therefore, data transmission period changes are not common after the installation of monitoring devices.

The consistency in the data transmission period was analyzed as Table 2.7. Many small PVs suffer from fluctuations as a result of intermittent, manual, and long-term disconnections. Some of them even presented a permanent change in period without

Table 2.7: Statistics for the Data Transmission Period Consistency

Consistency	PV Capacity Level (kW)				Total	
(%)	10	100	1,000	10,000	(ea)	(%)
70	61	2	1	-	64	3.43
80	579	-	-	-	579	31.03
90	774	-	1	-	775	41.53
100	5	154	220	69	448	24.01
Total	1,419	156	222	69	1,866	100.00

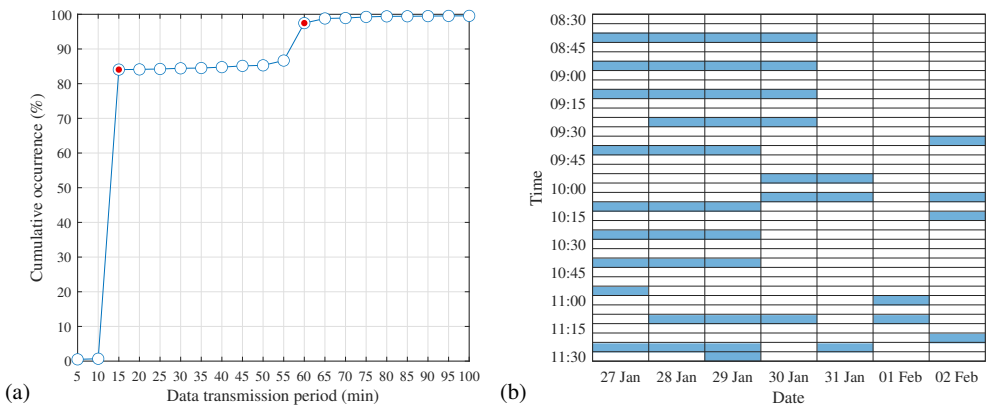

Figure 2.11: Fluctuation in data transmission period. (a) Cumulative distribution of the data transmission period for one PV. (b) Time-slots of the corresponding monitoring data.

any notification. The analysis result of one PV with both fluctuating and permanently changed data transmission period is presented in Fig. 2.11. The data transmission period had permanently changed from 15 min to 1 h on January 30, 2019. The time slots of the collected monitoring data show additional intermittent fluctuations.

Fluctuations in the data transmission period occur for various reasons. Lack of network bandwidth during peak hours results in delayed or missing data. The limitation of data processing speed in a server or monitoring device is also a reason. A

Table 2.8: Sensor Data with Delayed Data Transmission Period in a Sensor Network

Datetime	Value
2017-02-20 00:24:59	21.100
2017-02-20 00:25:59	21.100
2017-02-20 00:26:59	21.100
2017-02-20 00:28:00	21.100
2017-02-20 00:29:00	21.100
2017-02-20 00:30:00	21.100

sample of these error data was collected from a sensor network with a lower data transmission period for better understanding.

Table 2.8 presents part of the monitoring data collected from a sensor network. It has a fixed data transmission period of 1 min; however, the real period slightly exceeds this by a few milliseconds because of the monitoring device processing time. The device firmware did not consider the time difference and naively cast the millisecond-based time-series as the minute-based one. As a result, missing monitoring data was periodically observed when the accumulated time loss reached a multiple of one minute.

2.5.8 Errors: Disharmonious Data Collection Timings

Several types of communication failures are analyzed at the PV site level. However, facilities such as inverters and weather sensors in each PV may face different situations. Samples of monitoring data were collected for a PV with multiple inverters. Each inverter has a data transmission period of 15 min. The occurrence of different failures at different times and facilities, as presented in Fig. 2.12(b), (c), and (d), results in disharmonious time-series data with inconsistent data collection timings

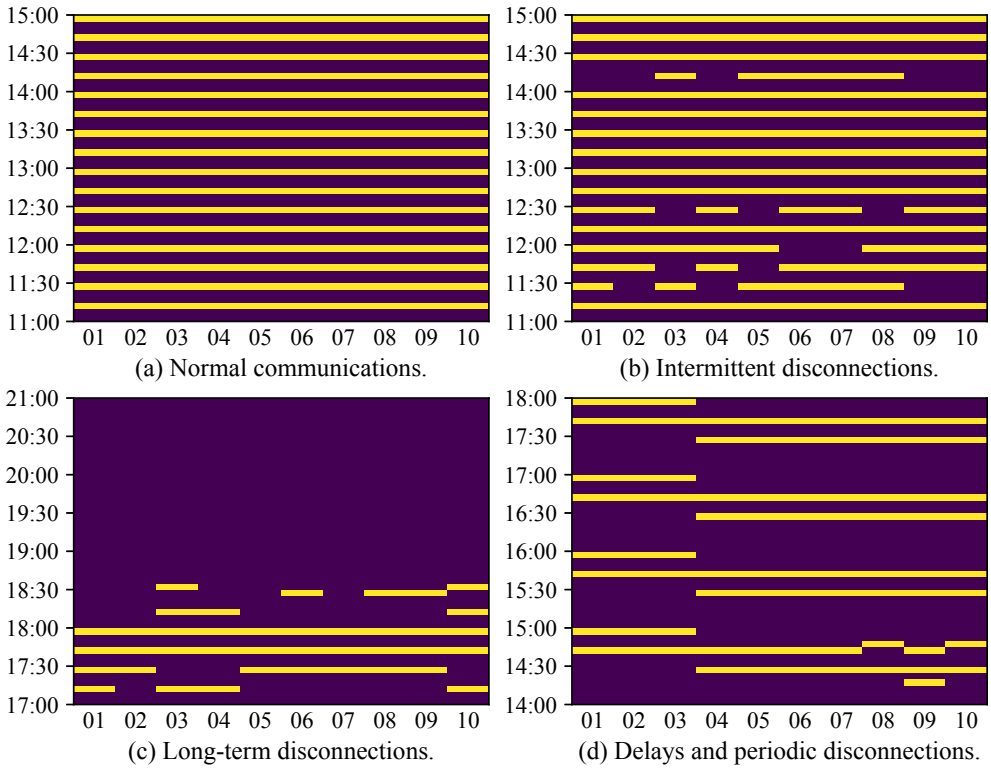

Figure 2.12: Monitoring data of a PV with multiple inverters under different communication failures. (a) Normal communication. (b) Intermittent disconnections. (c) Long-term disconnections. (d) Delays and periodic disconnections.

between inverters. Statistics for timing consistency were analyzed for 280 PVs with multiple inverters. The results are summarized in Table 2.9.

Consistency in data timing is an important issue for time-series analysis. The lack of consistency between the inverter and weather sensor data makes the correlation analysis between the solar irradiance and plant power generation impossible. A similar problem occurs when linking external service data to the monitoring system.

The monitoring system collects data from two external services, as shown in the database schema of Fig. 2.6. The electricity market service [74] operated by the Korea Power Exchange provides unit-balancing price data on an hourly basis. The weather

Table 2.9: Statistics for the Data Collection Timing Consistency Between Inverters

Consistency	Number of Inverters in Each PV (ea)					Total	
(%)	5	10	20	30	40	(ea)	(%)
50	2	1	-	-	-	3	1.07
60	-	-	-	-	-	-	0.00
70	-	-	-	1	-	1	0.36
80	2	-	-	-	-	2	0.71
90	4	12	2	-	-	18	6.43
100	194	50	10	1	1	256	91.43
Total	202	63	12	2	1	280	100.00

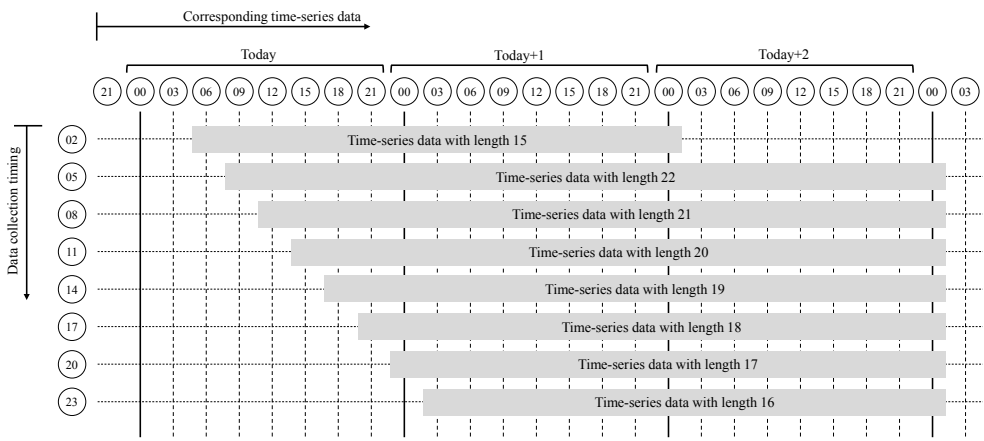

Figure 2.13: Discrete time-series data of the national weather forecasting service.

forecasting service [75] operated by the Korea Meteorological Administration provides weather forecast data on a three-hour basis. The weather forecast data also have complicated data timing and length, as presented in Fig. 2.13. Data preprocessing is mandatory for these external service data to match their timings and resolutions to those of the monitoring data, and therefore to enable further analyses such as cash balance calculation or PV power forecast.

2.6 Analyses with Error Data

Table 2.10: Summary of Errors Found in the PV Monitoring System Database

Specification of Data Error			Statistics in the Database		
Target	Description	Section	Total PVs (ea)	Error PVs (ea)	Ratio (%)
Static information	Missing	2.4.1	1,951	67	3.29
Static information	Redundancy	2.4.1	1,951	18	0.92
Static information	Incorrectness (location)	2.4.2	1,872	14	0.75
Static information	Incorrectness (address)	2.4.2	1,872	2	0.11
Static information	Incorrectness (facilities)	2.4.2	1,872	1	0.05
Monitoring data	Invalid (peak value)	2.5.1	1,843	3	0.16
Monitoring data	Invalid (unit)	2.5.2	1,866	8	0.43
Monitoring data	Invalid (confliction)	2.5.3	1,866	8	0.43
Monitoring data	Invalid (memory access)	2.5.4	1,866	8	0.43
Monitoring data	Disconnection (daily)	2.5.5	1,866	112	6.00
Monitoring data	Disconnection (long-term)	2.5.6	1,866	1,858	99.57
Monitoring data	Inconsistency (period)	2.5.7	1,866	643	34.46
Monitoring data	Inconsistency (timing)	2.5.8	280	6	2.14

The static and monitoring data errors found in the PV monitoring system database are summarized in Table 2.10. Each error would directly or indirectly affect the accuracy and availability of data-based PV analyses:

- Missing, redundant, and conflicting static information makes the corresponding data unusable for analyses.
- Incorrect static information may result in completely wrong conclusions.
- Invalid monitoring data values act as outliers and affect the result robustness.

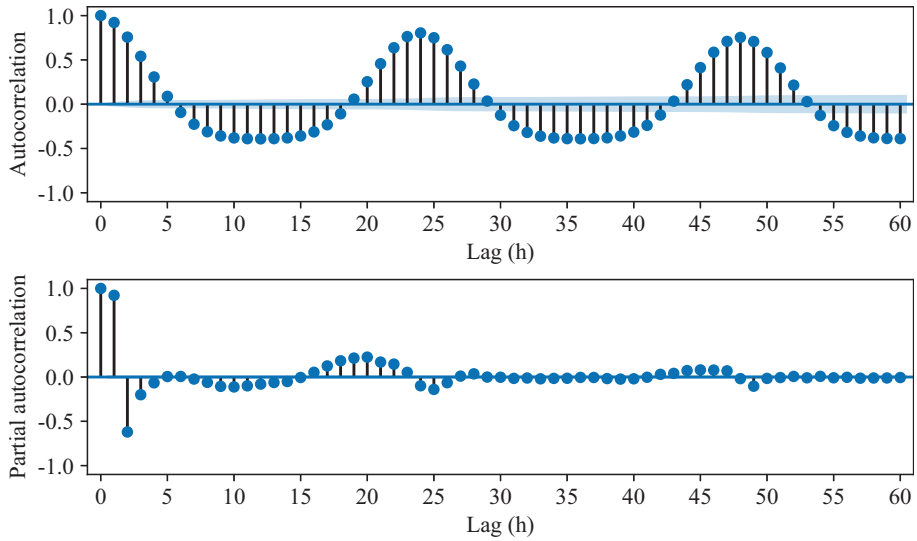

Figure 2.14: Autocorrelation and partial autocorrelation plots of hourly PV power generation data.

- Inconsistencies in data period and timing require additional data handling to match the time resolution.

The effects of errors on data-driven PV analyses were tested, particularly for the day-ahead hourly power generation forecast. PV power forecast helps a plant administrator decide a power purchase agreement, control local power supply, or even identify failures by the comparison with real power data. Autoregressive statistical models are suitable for forecasting studies because the hourly power generation of a PV has a strong correlation to its generation in the previous hour. The trend of power generation also has a short-term seasonality of 24 h. The autocorrelation and partial autocorrelation plots [53] of Fig. 2.14 reveal these intrinsic properties within the PV power generation data. Therefore, autoregressive integrated moving average (ARIMA) models, such as ARIMA$(1,0,0)\,(1,1,0)_{24}$ [76], ARIMA$(0,1,1)\,(1,0,1)_{24}$ [77], and others [78], have been widely used for PV power forecast studies.

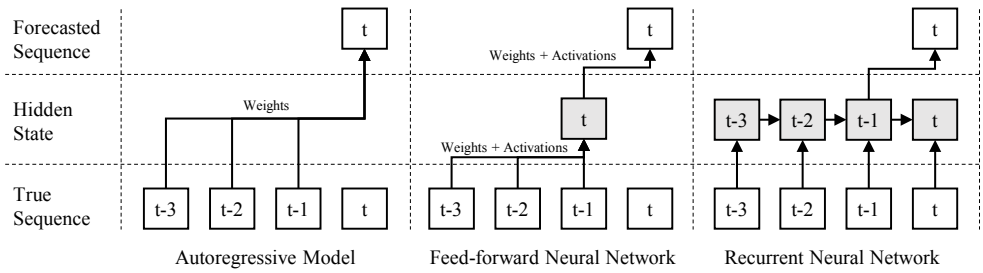

Figure 2.15: Autoregressive and neural network models for sequence modeling.

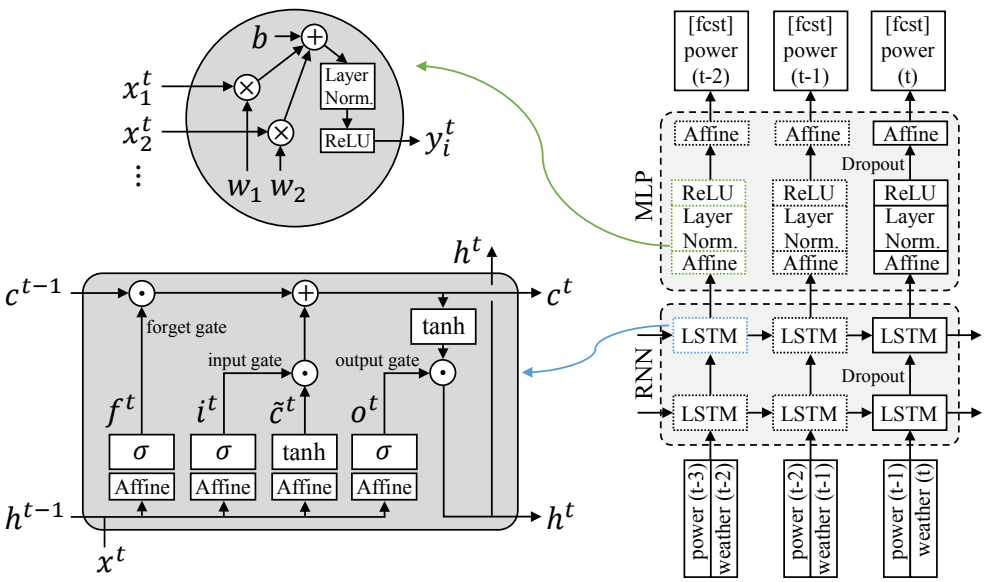

Figure 2.16: PV power forecast model using long short-term memory multilayers.

However, a more complicated data-driven model was applied for this analysis. Autoregressive models can be generalized as feed-forward neural networks, as presented in Fig. 2.15. Meanwhile, recurrent neural networks (RNNs) further apply a memory concept to store past information. These have shown better performance than traditional autoregressive models for PV power forecast studies [79, 80, 81]. The forecast model developed for this analysis comprises two long short-term memory [82] RNN layers and two feed-forward layers with rectified linear unit [83] ac-

tivations. The model also contains dropout [84] and layer normalization [85] layers for regularization. The structure of the model is presented in Fig. 2.16. The model is trained under a generative adversarial network framework [86] to further regularize its weight parameters. The robust regression error metric log-cosh loss [87] is applied during the training to reduce the effect of possible outliers.

The model is trained with historical power and weather data of a maximum two-year length and inferenced with one-day-length day-ahead forecasted weather data. Many PV studies, including power forecast research, use the atmospheric conditions of the PV location to produce accurate results [79, 88, 89]. Public weather data had been collected from the national weather forecasting service [75] to cooperate PVs with no weather sensor (e.g. small-scale PVs which suffer from economic feasibility problems). Three-hour-basis historical and forecasted weather data are interpolated into one-hour-basis ones to match with the power data.

Five weather parameters are selected as predictor variables for the PV power forecast model: cloudiness, precipitation type, relative humidity, temperature, and wind speed. Weather parameters that are not provided by the national weather service, such as solar irradiance, are excluded from the predictor variables. Cloudiness parameter with an ordinal value is selected as an alternative for solar irradiance. Categorical precipitation type and numerical relative humidity parameters are assumed to affect irradiance by absorption and scattering mechanisms of the water vapor in the air. Air temperature and wind speed parameters are expected to change PV cell temperature and corresponding performance by convection heat transfer.

Three types of data errors, as shown in Fig. 2.17, were simulated for a PV with 700 kW capacity to show their effects on the forecast accuracy: incorrect static in-

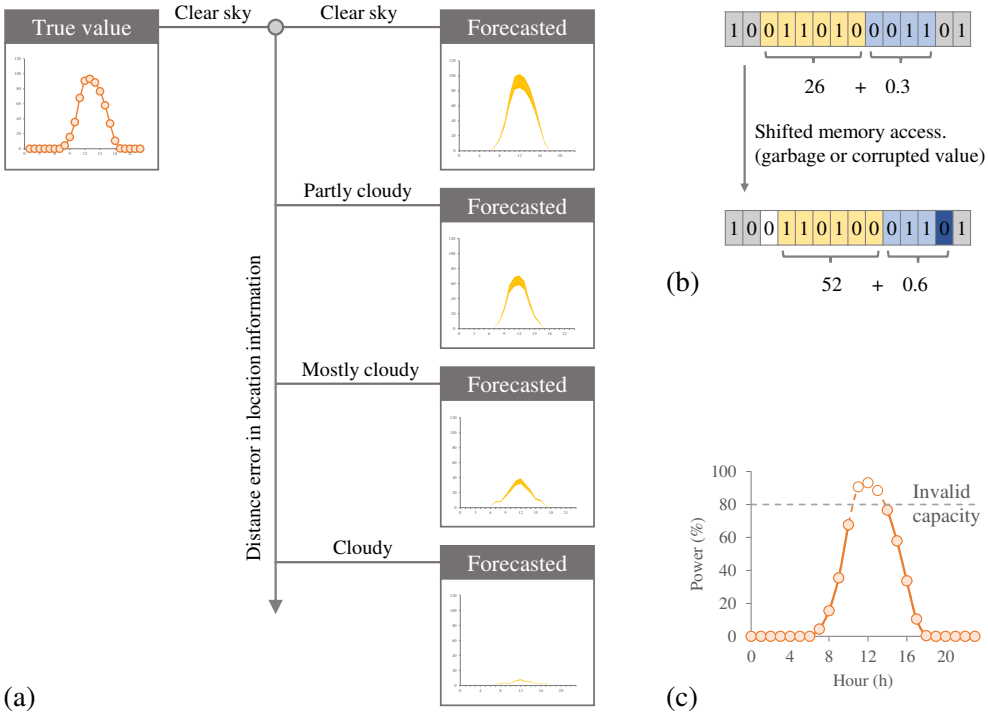

Figure 2.17: Simulated errors for the PV power forecast study. (a) Incorrect location information and corresponding weather data. (b) Intermittent peak power value errors as a result of invalid memory access. (c) Missing monitoring data as a result of data cleaning with invalid capacity information.

formation in location, invalid monitoring data values, and missing monitoring data. The performance of a model trained with error data is evaluated by the mean absolute error (MAE) and root mean square error (RMSE) of the day-ahead hourly forecast results during a month. These two metrics are normalized by the inverter capacity as normalized MAE (NMAE) and normalized RMSE (NRMSE). It is a common technique in PV studies to provide a value similar to the mean absolute percentage error while considering zero-power generation hours [90].

2.6.1 Effect of Incorrect Location Information

Incorrect static information in the location results in wrong weather data as the model input. The impact of each weather parameter on hourly PV power generation is first analyzed using a linear least squares model [91, 92]:

$$\begin{aligned}\log p_{imh} =& \beta_1 \text{clear}_{imh} + \beta_2 \text{cloudy}_{imh} + \beta_3 \text{rain}_{imh} + \beta_4 \text{snow}_{imh} \\ &+ \beta_5 \text{reh}_{imh} + \beta_6 \text{temp}_{imh} + \beta_7 \text{wsd}_{imh} + \alpha_i + \delta_m + \tau_h + \epsilon_{imh} \quad (2.1)\end{aligned}$$

where α_i, δ_m, and τ_h represent fixed effects by an individual inverter i, month-of-year m, and hour-of-day h, respectively. The three-level cloudiness variable is split into two dummy variables which represent clear (clear_{imh}) and cloudy (cloudy_{imh}) conditions. A partly cloudy condition is defined as the combination of zero values for the dummy variables. The eight-level precipitation-type variable is merged and then split into two dummy variables rain_{imh} and snow_{imh}. reh_{imh}, temp_{imh}, and wsd_{imh} represent relative humidity, temperature, and wind speed, respectively. β is the coefficient of interest and ϵ_{imh} is the error term. Hourly PV power generation p_{imh} is transformed into a logarithmic form to obtain approximations of percentage changes: a unit increase in a weather parameter multiplies p_{imh} by $\exp\beta$, which is approximately $\exp\beta = 1 + \beta + \beta^2/2! + \cdots \approx 1 + \beta$ for a small value of β. Data with zero power, which represent idle states of PVs, are excluded from the analysis because of the logarithmic transform.

The analysis result is presented in Table 2.11. Solar irradiance conditions, cloudiness and precipitation type, presented a significant impact on hourly power generation. Snow condition was identified as one with a positive impact because it increases

Table 2.11: Impact of Weather Conditions on Hourly Power Generation

Models	(1)	(2)	(3)	(4)	(5)	(6)
Clear	+0.206***	+0.207***	+0.207***	+0.267***	+0.198***	+0.235***
	(0.001)	(0.001)	(0.001)	(0.001)	(0.001)	(0.001)
Cloudy	−0.298***	−0.300***	−0.299***	−0.381***	−0.311***	−0.382***
	(0.001)	(0.001)	(0.001)	(0.001)	(0.001)	(0.001)
Rain	−0.387***	−0.393***	−0.395***	−0.491***	−0.356***	−0.435***
	(0.002)	(0.002)	(0.002)	(0.002)	(0.002)	(0.002)
Snow	+0.120***	+0.108***	+0.096***	+0.045***	+0.181***	−0.249***
	(0.008)	(0.008)	(0.008)	(0.008)	(0.008)	(0.008)
Relative humidity (%)	−0.010***	−0.010***	−0.010***		−0.009***	
	(0.00004)	(0.00004)	(0.00004)		(0.00003)	
Temperature (°C)	+0.002***	+0.003***			+0.025***	
	(0.0001)	(0.0001)			(0.0001)	
Wind speed (m/s)	−0.005***				−0.001***	
	(0.0003)				(0.0003)	
Fixed effects						
Inverter	Y	Y	Y	Y	Y	Y
Month-of-year	Y	Y	Y	Y		
Hour-of-day	Y	Y	Y	Y	Y	Y
Number of observations	2,614,136	2,614,136	2,614,136	2,614,136	2,614,136	2,614,136
F statistics	0.885	0.885	0.885	0.881	0.880	0.871
R^2	8430.7***	8432.9***	8435.3***	8182.6***	8110.0***	7487.8***

Notes: Standard errors are denoted in parentheses.
Statistical significance at the 10%, 5% and 1% levels is represented as *, ** and ***, respectively.

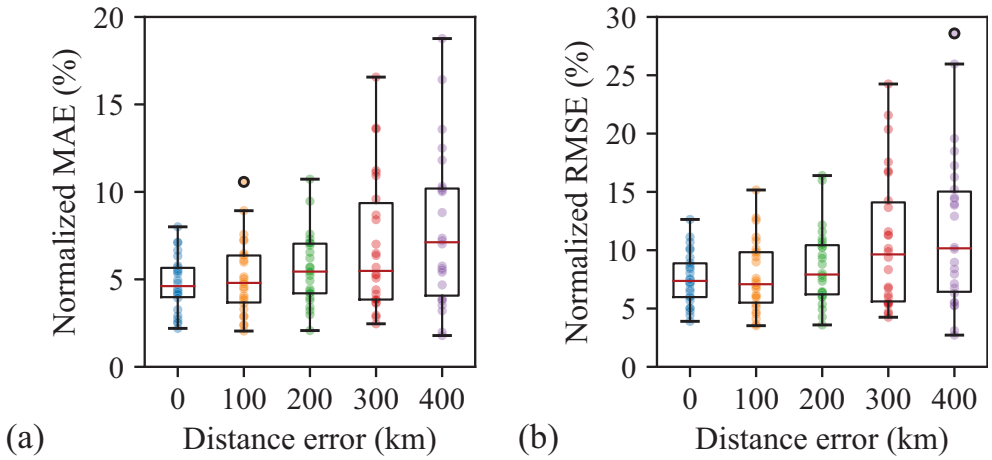

Figure 2.18: Effect of distance error in location information on the forecast accuracy. (a) Normalized mean absolute error (NMAE). (b) Normalized root mean square error (NRMSE).

the surface albedo and corresponding horizon brightening [93]. Removing the month-of-year fixed effect change this impact into a negative one; the decrease in solar irradiance during winter is merged into the impact of snow condition.

The distance error between the true PV location and incorrect information was simulated at several levels. The model was trained with the historical weather data of an incorrect location and inference with the day-ahead weather forecast data of that location. The increases in NMAE and NRMSE along with the distance error are presented in Fig. 2.18. Each dot represents NMAE or NRMSE of a day-ahead hourly forecast result for each day. The two metrics show exponential-like growth trends for both the median and interquartile range.

2.6.2 Effect of Invalid Monitoring Data Values

Three types of value errors can be found within the monitoring data: intermittent peaks, invalid units, and garbage values. Appropriate filters are required for data pre-

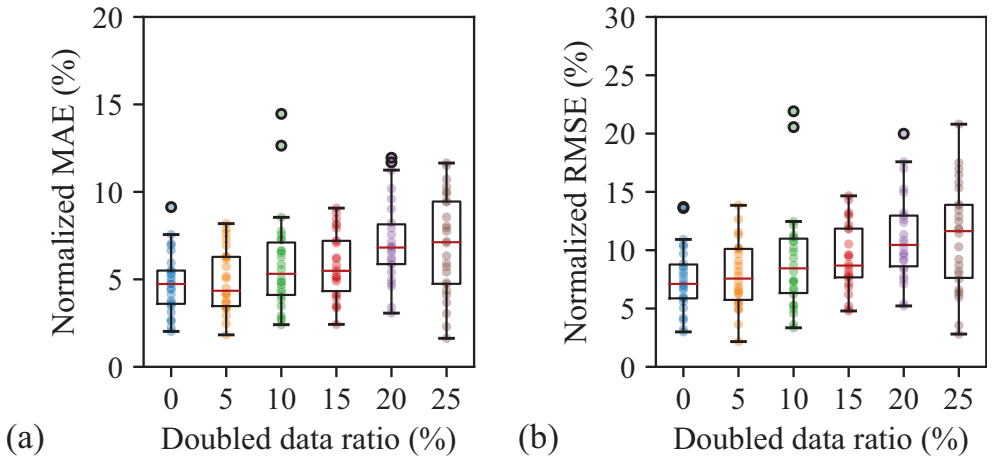

Figure 2.19: Effect of randomly doubled values in historical power data on the forecast accuracy. (a) NMAE. (b) NRMSE.

processing to detect errors prior to applying the data as forecast input. However, the development of a filtering algorithm recursively requires knowledge about errors. Errors that are not familiar to PV administrators, such as garbage or corrupted values due to memory problems, may not be detected because of the absence of a specialized filtering algorithm.

The invalid monitoring data value error was simulated as the random occurrence of doubled power values. It represents not only the intermittent peak values, but also the corrupted values as a result of accessing a bitwise shifted memory address of the binary data. This type of doubled-value error was reported by a metering company for their real-world metering system, without identifying the cause of an error [51].

The level of error occurrence probability was simulated from 5% to 25%, as shown in Fig. 2.19. Linear growth trends were observed for the NMAE and NRMSE metrics. The growth in the forecast error was lower than expected because of three reasons. First, the number of doubled values was half the simulation target because

the multiple of zero values at night hours is equal to zero. Second, the effect of the error in power data was limited because the multivariable forecast model uses weather parameters as additional predictor variables. Univariable models such as ARIMA may suffer more significant problems. Lastly, the introduction of the robust regression error metric during the model training further reduced the effect of outliers with doubled values.

2.6.3 Effect of Missing Monitoring Data

Missing monitoring data is closely related to data collection problems. Inconsistencies in data collection timing and period generate missing completely at random (MCAR) [55] patterns. The termination of daily monitoring results in missing values at night hours, which can be simply assumed to be zero. By contrast, continuous missing data from long-term disconnections are difficult to recover.

Missing monitoring data can also occur as a result of data cleaning. Correcting intermittent peak or corrupted values as missing ones again produces MCAR patterns. However, correcting for power values exceeding the capacity limit may remove every high-power data if the target PV suffers from invalid unit error or conflicting static information error. Missing not at random (MNAR) patterns occur in these cases. Introducing time and weather data, which have strong correlations with the power data, during data imputation may remedy the MNAR situation as the one similar to missing at random (MAR).

Three imputation methods were applied to both the MCAR and MNAR situations described here. Complete-case analysis, also known as list-wise deletion [55, 56, 57], was first tried as the simplest ad-hoc method with its capability of producing unbiased

estimation for MCAR. A list of daily data is completely removed if any error is found within its daily power generation data. Therefore, even a small error occurrence of 1% in hourly data may remove 21.4% of daily data and the corresponding statistical power of the models.

In contrast to the complete-case analysis, mean and regression imputations were employed to preserve the sample size and corresponding statistical power. Mean imputation replaces an error value with the average of the same hour data within the previous and next one-week intervals. Regression imputation for this analysis applies a cubic spline [94] to the same interval data in the time domain. Both imputation methods have their own advantages; the former can decrease the effect of noise in samples by averaging, and the latter can consider the time-series trend of the data.

More complicated regression methods such as ARIMA and neural network models were not tested because the development of a precise model for data imputation recursively requires large error-free data. Multiple imputation methods [95, 96, 97] were also ignored in this study because training and test for multiple datasets proportionally increase the training time.

The performance of the trained model with the MCAR error in historical power data is presented in Fig. 2.20. Error bars represent a standard error of the forecast accuracy for each day. Complete-case analysis, which presented a steep growth in model error metrics, was identified as an improper method for PV data imputation because a significant amount of training data was removed during the imputation. Mean and regression imputations effectively controlled the decrease in model performance by replacing the missing values as plausible ones.

Similar but different results were derived from the test with the MNAR error, i.e.,

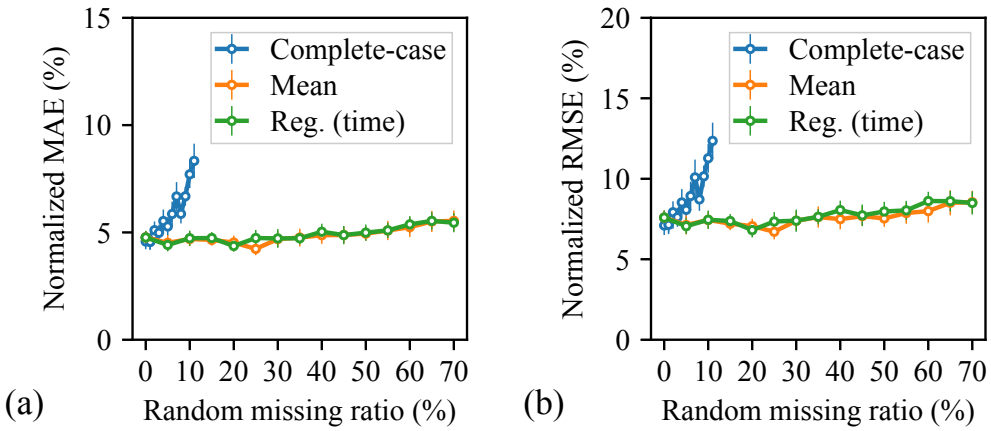

Figure 2.20: NMAE and NRMSE of the trained model with different imputation methods for the random missing error.

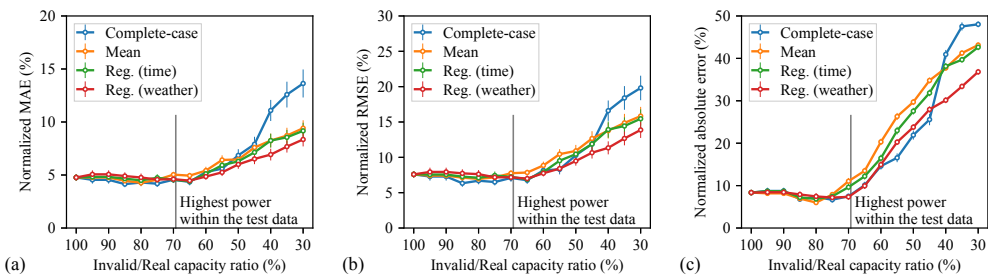

Figure 2.21: NMAE and NRMSE of the trained model with different imputation methods for the high-power data missing error. (a) NMAE. (b) NRMSE. (c) Normalized absolute error for the test data with only high-power values.

missing of high-power data. Each test simulated the training data cleaning process with a power value limit of 30—100% of the real PV capacity. Three imputation methods were again applied after the data cleaning. Regression imputation in the weather data domain was additionally tested to deal with the MNAR situation as the MAR one. A simple linear model of temperature and humidity was estimated using the complete-case data of each hour.

The performance of the trained model shown in Fig. 2.21(a) and (b) exhibits a

notable decrease in performance as the simulated power limit becomes lower than 70% of the original PV capacity. This value is the same as the maximum power value found within the test data. Data cleaning with a power limit lower than this value removes higher values within the training data. As a result, the statistical forecast model produces unbounded results for the high-power condition.

Fig. 2.21(c) focuses more on such high-power conditions by calculating the forecast performance only for power data with values higher than half of the PV capacity. A linear but steep decrease in performance was observed regardless of the imputation method. Complete-case analysis was the most effective among the initial three imputation methods, unless extreme error situations. Mean imputation presented the worst overall performance in contrast to the MCAR case. Meanwhile, regression imputation in the weather domain presented the best performance, despite the simplicity of a linear extrapolation model applied to the imputation. The correlation between the weather and power data helped to remedy the performance decrease resulted from the MNAR situation, as expected.

2.7 Conclusion

A PV monitoring system that covers nearly 2,000 plants nationwide in Korea is introduced in this study. Several types of errors in PV monitoring data are categorized and analyzed with the help of massive data collected by the monitoring system. This type of study is rare in engineering fields because of the lack of error cases for each plant and the reluctance to share data among plant owners. PV administrators such as O&M service companies are expected to benefit from this study as it identifies the issues that should be checked for their continuous and error-free services. Error iden-

tification processes that are suggested in this study can be applied to the database or data collecting API to inherently prevent the collection of erroneous data. The existence of error-free data also helps researchers conduct data-driven analyses by saving the data preprocessing time and enhancing the result accuracy.

The errors found in this study are mainly categorized as those within the static information data and those within the real-time monitoring data. A general focus on PV data, including data preprocessing targets, may only be limited to monitoring data. Intermittent errors within the monitoring data are easily notified by administrators because of their invalid or missing values. However, PV power forecast analyses with simulated error data proved that static information data errors such as invalid location or capacity significantly affect the accuracy of the results. Double-checking the PV specification document is the most effective and easiest method to increase the quality of PV data analyses. If there are remaining monitoring data errors, regression imputation in the time domain will provide good results in most cases.

The limitation of this study mainly comes from the sample size and privacy issue. One example of the sample size issue is related to the geographical distribution of PVs. It is expected that a PV in an uninhabited island may suffer from serious monitoring problems because of unstable network connections, corrosion on monitoring devices, and lack of supports for the maintenance. However, it was impossible to validate this hypothesis because only a few PVs match with this geographical condition. Although this study analyzes the data from approximately 0.5% of nationwide PVs, a large enough sample in its number, increasing the sample size would enable additional analyses on data errors.

The names of facility manufacturers or monitoring service companies related to

error situations are not mentioned in this study because of privacy issues. One thing that can be said is that each company tends to use the same monitoring devices for every PV site, thereby reproducing the same error. Therefore, plant owners should share their data and opinions to identify the existing issues and provide the service provider a chance to repair the devices before the issues become a significant problem.

2.8 Acknowledgments

© 2021 Elsevier. Reprinted, from Jongwoo Choi, Il-Woo Lee, and Suk-Won Cha, "Analysis of data errors in the solar photovoltaic monitoring system database: An overview of nationwide power plants in Korea," in *Renewable and Sustainable Energy Reviews,* vol. 156, 112007, Mar. 2022, doi: 10.1016/j.rser.2021.112007.

Chapter 3

Robust Scheduling of a Microgrid Energy Storage System with Ancillary Service Considerations

This chapter presents a robust optimal control strategy for an energy storage system (ESS) of a grid-connected microgrid. The robust optimal control guarantees the highest possible economic benefit of the control schedule even under the worst case net demand prediction error conditions. The global optimum of a concise control problem can be found within a short computation time using mixed-integer linear programming. The rolling horizon controller of the energy management system periodically updates the control schedule by solving the control problem. The state of charge of an ESS is precisely calculated by the piecewise linearization technique using nonlinear efficiency maps. Grid ancillary services, which are denoted as external working conditions in this chapter, can be dynamically applied during the optimization process. Two ancillary services are considered: peak control and demand response. The proposed strategy provides control robustness in terms of cost reduction, precise control, and external effect.

3.1 Background

A microgrid is a localized electrical grid that manages a variety of loads and distributed energy resources (DERs) within its electrical boundaries [98]. It operates in a grid-connected or island mode depending on its connection to the main grid. In a grid-connected operation, it acts as a single controllable resource that enables the main grid to establish a unified binding contract with regard to its aggregated power usage pattern [99]. Instead, the main grid takes responsibility for its power quality control. The entire power/energy capacities of DERs can be utilized for optimal energy management [100]. By contrast, in an island mode operation, a certain portion of the DER capacities must be allocated for power quality control such as voltage and frequency regulations [101].

DERs in a microgrid can be classified as either dispatchable (active) or non-dispatchable (passive) resources [102]. Controllable conventional generators and uncontrollable renewable generators are typical examples of each category, respectively. The microgrid energy management system (EMS) predicts the net demand power of the loads and uncontrollable passive DERs and controls the active DERs. The main objective of the microgrid energy management is to achieve the highest possible economic benefit by minimizing its operating costs [103, 104].

Several control strategies have been applied to microgrid optimal control problems. Evolutionary algorithms such as genetic algorithm [105, 106, 107] and particle swarm optimization [100, 108] are generally applied to find a local optimum of the nonlinear control problem. Levron *et al.* [109] proposed a dynamic programming approach to find the global optimum. These algorithms can solve complex optimization problems, however, they suffer from long computation time. Linear programming

approaches have been proposed in many studies to overcome this disadvantage.

Linear programming is a subfield of convex optimization. It consists of a linear objective and linear equality/inequality constraints that define a convex polytope feasible region [110]. The convex feature of the optimal problem guarantees that its local minimum must be the global one. Although much effort is required to linearize the control problem; or it is sometimes even impossible, linear programming is worth trying because of its nearly linear [111] fast computation time.

In addition to linear programming, mixed-integer linear programming (MILP) is also used for microgrid economic scheduling problems to represent microgrid state conditions as integer binary variables. Branch-and-cut algorithm [112] is applied to solve the optimization problem with integer variables. Morias *et al.* [113] studied an optimal scheduling of DERs under different unit power costs. Hoke *et al.* [114] applied preprocessing and postprocessing steps to work with nonlinear constraints. Jiang *et al.* [115] presented an MILP-based optimal scheduling algorithm for both grid-connected and island modes.

Although the EMS attempts to maximize the economic benefit of a microgrid, the prediction uncertainty of a net demand power decreases the reliability of the optimization. Xiang *et al.* [103] applied an orthogonal array testing method to control the worst case scenario. Handschin *et al.* [116] presented a stochastic optimization method for price and demand uncertainties. Malysz *et al.* [117] proposed a fast robust counterpart optimization that considered the prediction uncertainty threshold. Both Handschin *et al.* [116] and Malysz *et al.* [117] used MILP to achieve robust optimal results. MILP-based online optimization has been also proposed to deal with future uncertainty. Parisio *et al.* [118] proposed a model predictive control to peri-

odically update the control schedule. Prodan and Zio [119] applied a time-varying weight concept to improve system reliability. Palma-Behnke *et al.* [120] presented a rolling horizon control strategy and communication infrastructures of an EMS.

This chapter first introduces an MILP-based robust optimal control strategy for an energy storage system (ESS) of a grid-connected microgrid. The robust control strategy allows the microgrid to robustly maintain a low level of grid power usage cost even if the net demand prediction error increases within the predefined range. Several robust optimization approaches are proposed to maximize the worst case economic benefit of an ESS operation. The concise form of a control problem can handle an interval-type net demand prediction uncertainty within a short computation time, thereby enabling its application as a rolling-horizon controller.

Along with the robust optimization, this chapter presents a method to introduce 2D efficiency maps for the ESS state of charge (SOC) calculation. The efficiency of an ESS strongly depends on its power and SOC states [121, 122, 123] because of electrical, electrochemical, or mechanical properties. The application of nonlinear efficiency maps using a piecewise linearization technique can provide a more precise control result than that of a fixed efficiency.

Finally, the application of ancillary services is proposed to consider short-term external effects from the main grid. The robust optimal control strategy can dynamically apply these external working conditions to achieve both robust optimal control and operational limitations. Two external working conditions are considered in this study: peak control and demand response. Each condition requires insertion of additional terms into the optimization problem. The proposed control strategy provides control robustness in terms of cost reduction, precise control, and external effect.

The rest of this chapter is organized as follows. The full EMS architecture is described in Section 3.2. Robust optimal scheduling of the microgrid ESS is proposed in Section 3.3. Applications of nonlinear ESS efficiency maps and external working conditions are presented in Section 3.4 and 3.5. Section 3.6 presents the robust optimal control results under different working scenarios. The chapter summary is given in Section 3.7.

3.2 System Architecture

This study targets a grid-connected microgrid as presented in Fig. 3.1. Building and campus microgrids are typical examples of this grid-connected microgrid. Surplus/Insufficient power of the microgrid is traded to the main grid. The microgrid

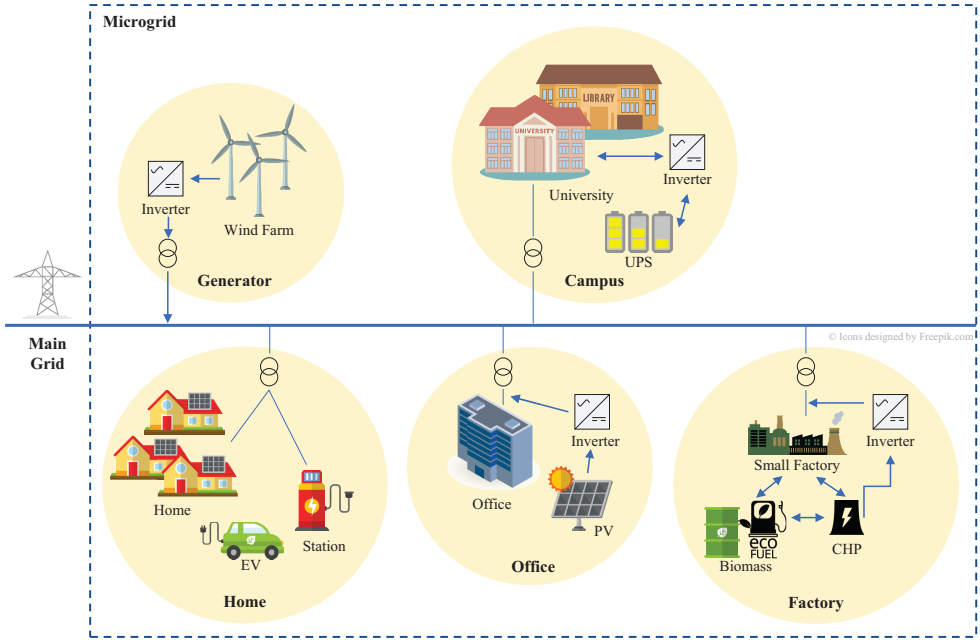

Figure 3.1: Typical grid-connected microgrids with their loads and DERs.

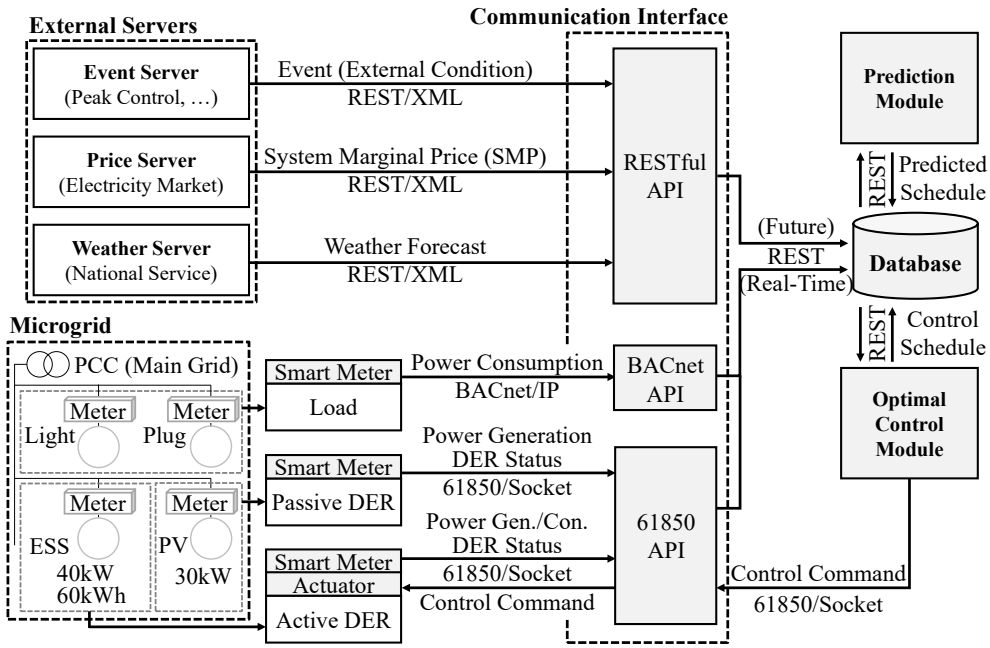

Figure 3.2: Communication flow of the target microgrid EMS. The EMS receives real-time/future data through its communication interface.

EMS controls its active DERs to achieve the highest economic benefit from the power transaction. A building microgrid with a controllable ESS is considered in this study.

Fig. 3.2 presents communication between the target microgrid EMS and internal/external systems. The communication interface receives real-time power usage data from the internal energy resources. A smart meter measures the real-time power usage and sends it through BACnet [124] or IEC 61850 [125] protocol. IEC 61850 protocol is also used to transfer DER state information and control commands between the active DER actuator and the microgrid EMS.

The RESTful [126] application programming interface (API) requests the XML structured data from three external servers. The price server provides a daily scheduled buying/selling system marginal price (SMP). The weather server provides local

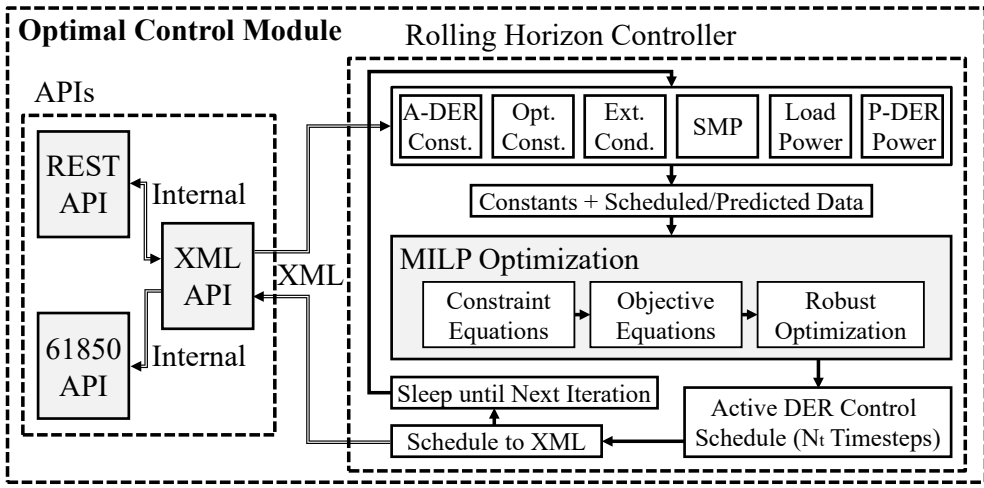

Figure 3.3: Iterative schedule generation process of the rolling horizon controller.

weather forecast. The event server provides additional operating limitations as external working conditions. The prediction module predicts future power usages of the loads and passive DERs. The optimal control module generates the active DER control schedule that maximizes the economic benefit under given conditions.

The optimal control module shown in Fig. 3.3 provides rolling horizon control of the active DER. It applies the latest information to the rolling horizon optimization to make the administrator manage the remaining time horizon. The MILP-based rolling horizon controller uses the input information of following XML files: active DER properties, optimization constants, scheduled external working conditions, unit power prices, and predicted power usages of the loads and passive DERs.

3.3 Robust MILP Optimization

3.3.1 ESS Constraints

A simple grid-connected microgrid system presented in Fig. 3.2 is considered in this study. It contains an ESS as its only active DER. Prior to introducing the grid-level optimization, the physical system limitations of an ESS have to be considered.

The maximum power of an ESS is limited by the system specification. The minimum power of an ESS can be also limited with respect to the operation of internal equipment, i.e., balance of plants. For example, some vanadium redox flow batteries have the minimum power limitation to guarantee the consistent operation of their circulating pumps. This study considers both the maximum and minimum power limitations to generalize the problem:

$$P_{chg}^{min,spec}\mathbf{1} \leq \boldsymbol{P}_{chg}^{min} \leq \boldsymbol{P}_{chg}^{max} \leq P_{chg}^{max,spec}\mathbf{1} \tag{3.1}$$

$$P_{dis}^{min,spec}\mathbf{1} \leq \boldsymbol{P}_{dis}^{min} \leq \boldsymbol{P}_{dis}^{max} \leq P_{dis}^{max,spec}\mathbf{1} \tag{3.2}$$

$$\boldsymbol{P}_{chg}^{min} \circ \boldsymbol{\delta}_{chg} \leq \boldsymbol{P}_{chg} \leq \boldsymbol{P}_{chg}^{max} \circ \boldsymbol{\delta}_{chg} \tag{3.3}$$

$$\boldsymbol{P}_{dis}^{min} \circ \boldsymbol{\delta}_{dis} \leq \boldsymbol{P}_{dis} \leq \boldsymbol{P}_{dis}^{max} \circ \boldsymbol{\delta}_{dis} \tag{3.4}$$

$$\mathbf{0} \leq \boldsymbol{\delta}_{chg} + \boldsymbol{\delta}_{dis} \leq \mathbf{1} \tag{3.5}$$

where operator $\circ$ represents the entry-wise production. Two binary vectors $\boldsymbol{\delta}_{chg}$ and $\boldsymbol{\delta}_{dis}$ indicate the ESS operating state. The ESS system-specified power limitations are defined as $P_{chg}^{min,spec}$, $P_{chg}^{max,spec}$, $P_{dis}^{min,spec}$, and $P_{dis}^{max,spec}$. The administrator can additionally define the user-defined limitations $\boldsymbol{P}_{chg}^{min}$, $\boldsymbol{P}_{chg}^{max}$, $\boldsymbol{P}_{dis}^{min}$, and $\boldsymbol{P}_{dis}^{max}$ to consider optional properties such as safety and lifetime. Vectors $\boldsymbol{P}_{chg}$ and $\boldsymbol{P}_{dis}$

represent the charge and discharge power in the entire schedule period, respectively.

The ESS SOC limitation is defined similar to the power limitation. A simple discrete-time ESS SOC model is defined as

$$\boldsymbol{S}^{i+1} = \boldsymbol{S}^{1} - \sum\nolimits_{k=1}^{i} \boldsymbol{dt}^{k} \left(\boldsymbol{P}_{dis}^{k} / \boldsymbol{\eta}_{dis}^{k} - \boldsymbol{\eta}_{chg}^{k} \boldsymbol{P}_{chg}^{k} \right) / ECap \tag{3.6}$$

where $\boldsymbol{S}$ is the SOC vector, i is the time-step index, $\boldsymbol{dt}$ is the time-step length vector, $ECap$ is the ESS energy capacity, and $\boldsymbol{\eta}_{chg}$ and $\boldsymbol{\eta}_{dis}$ are the charge and discharge efficiency vectors, respectively. The ESS SOC limitations are expressed as

$$S^{min,spec}\mathbf{1} \leq \boldsymbol{S}^{min} \leq \boldsymbol{S} \leq \boldsymbol{S}^{max} \leq S^{max,spec}\mathbf{1}. \tag{3.7}$$

3.3.2 Non-Robust Approach

The net demand power of the microgrid must be predicted prior to the formulation of the control problem. The prediction module of the microgrid EMS predicts demand power $\boldsymbol{P}_D$ for N_t discrete time steps using load power consumption pattern $\boldsymbol{P}_L$ and passive DER (PV) power generation pattern $\boldsymbol{P}_{PV}$. Main grid power usage $\boldsymbol{P}_g$ of the grid-connected microgrid under ESS operation $\boldsymbol{P}_{ESS}$ is expressed as

$$\boldsymbol{P}_g = (\boldsymbol{P}_L - \boldsymbol{P}_{PV}) - \boldsymbol{P}_{ESS} = \boldsymbol{P}_D - \boldsymbol{P}_{dis} + \boldsymbol{P}_{chg}. \tag{3.8}$$

If there is no ESS operation, the unbalanced microgrid net demand must be traded with the main grid. The grid power-usage cost in the absence of ESS operation is

$$\sum\nolimits_{\boldsymbol{P}_D^i > 0} \boldsymbol{c}_b^i \boldsymbol{P}_D^i \boldsymbol{dt}^i + \sum\nolimits_{\boldsymbol{P}_D^i < 0} \boldsymbol{c}_s^i \boldsymbol{P}_D^i \boldsymbol{dt}^i \equiv (\boldsymbol{c}_{bs} \circ \boldsymbol{P}_D)^{\intercal} \, \boldsymbol{dt} \tag{3.9}$$

where $\boldsymbol{c}_b$ and $\boldsymbol{c}_s$ are the unit power buying and selling cost vectors, respectively. $\boldsymbol{c}_b$ must be higher than $\boldsymbol{c}_s$ to prevent the microgrid from realizing a profit by directly selling the bought power. Vector $\boldsymbol{c}_{bs}$ represents the unit price applied to the no ESS condition. Each of its element $\boldsymbol{c}_{bs}^i$ has a value of $\boldsymbol{c}_b^i$ or $\boldsymbol{c}_s^i$.

The main objective of the non-robust optimal control is achieving the highest possible benefit by minimizing the grid power-usage cost during the entire period:

$$\underset{\boldsymbol{P}_{chg},\boldsymbol{P}_{dis}}{\text{minimize}} \left(\sum_{i\in\{i|\boldsymbol{P}_g^i>0\}} \boldsymbol{c}_b^i \boldsymbol{P}_g^i \boldsymbol{dt}^i + \sum_{i\in\{i|\boldsymbol{P}_g^i<0\}} \boldsymbol{c}_s^i \boldsymbol{P}_g^i \boldsymbol{dt}^i \right). \tag{3.10}$$

The MILP form of the control problem aims to maximize the economic benefit as a result of the optimal ESS control. It has $5N_t$ variables and $5N_t$ constraints except for the integer value limitations of binary variables:

$$\text{minimize } \{(\boldsymbol{c}_b \circ \boldsymbol{P}_{gb} + \boldsymbol{c}_s \circ \boldsymbol{P}_{gs}) - \boldsymbol{c}_{bs} \circ \boldsymbol{P}_D\}^\intercal \boldsymbol{dt} \tag{3.11}$$

$$\text{s.t. } \boldsymbol{P}_{gb} + \boldsymbol{P}_{gs} = \boldsymbol{P}_D - \boldsymbol{P}_{dis} + \boldsymbol{P}_{chg} \tag{3.12}$$

$$\boldsymbol{0} \le \boldsymbol{P}_{gb} \le P_{line}^{limit} \boldsymbol{\delta}_g \tag{3.13}$$

$$-P_{line}^{limit} (\boldsymbol{1} - \boldsymbol{\delta}_g) \le \boldsymbol{P}_{gs} \le \boldsymbol{0} \tag{3.14}$$

where vectors $\boldsymbol{P}_{gb}$ and $\boldsymbol{P}_{gs}$ represent the buying and selling portions of $\boldsymbol{P}_g$, respectively. Binary vector $\boldsymbol{\delta}_g$ represents the sign of $\boldsymbol{P}_g$. Constant P_{line}^{limit} indicates the maximum power limitation of the power line, which stands for a large-enough value. Constraints (3.12)–(3.14) can be converted into general linear form $\boldsymbol{Ax} \le \boldsymbol{b}$. Therefore, the control problem can be solved using MILP algorithms with optimization arguments $\boldsymbol{P}_{gb}$, $\boldsymbol{P}_{gs}$, $\boldsymbol{P}_{chg}$, $\boldsymbol{P}_{dis}$, and $\boldsymbol{\delta}_g$.

3.3.3 Intuitive Approach

Although the optimal control problem requires a future net demand schedule as its input parameter, predicted value $\boldsymbol{P}_D$ may include an error because of the perturbations in the load power consumption and renewable power generation. Robust optimization techniques can help in handling the uncertain constants of the control problem. However, duplicated usages of uncertain constant $\boldsymbol{P}_D$ in both (3.11) and (3.12) makes direct application of these techniques difficult [127].

Interval-type prediction error boundaries $\boldsymbol{P}_D^{min}$ and $\boldsymbol{P}_D^{max}$ of uncertain net demand $\boldsymbol{P}_D$ are introduced to optimize the worst case control result. The main objective of the robust optimal control is to maintain a high level of benefit regardless of the prediction uncertainty. Intuitively, it can be assumed that the worst case benefit would occur under extreme prediction error conditions. The robust optimization form of the control problem becomes

$$\text{minimize } \mathbf{1}^{\intercal}\boldsymbol{obj} \tag{3.15}$$

$$\text{s.t. } \boldsymbol{P}_{gb,1} + \boldsymbol{P}_{gs,1} = \boldsymbol{P}_D^{min} - \boldsymbol{P}_{dis} + \boldsymbol{P}_{chg} \tag{3.16}$$

$$\mathbf{0} \leq \boldsymbol{P}_{gb,1} \leq P_{line}^{limit}\boldsymbol{\delta}_{g,1} \tag{3.17}$$

$$-P_{line}^{limit}\left(\mathbf{1} - \boldsymbol{\delta}_{g,1}\right) \leq \boldsymbol{P}_{gs,1} \leq \mathbf{0} \tag{3.18}$$

$$\boldsymbol{P}_{gb,2} + \boldsymbol{P}_{gs,2} = \boldsymbol{P}_D^{max} - \boldsymbol{P}_{dis} + \boldsymbol{P}_{chg} \tag{3.19}$$

$$\mathbf{0} \leq \boldsymbol{P}_{gb,2} \leq P_{line}^{limit}\boldsymbol{\delta}_{g,2} \tag{3.20}$$

$$-P_{line}^{limit}\left(\mathbf{1} - \boldsymbol{\delta}_{g,2}\right) \leq \boldsymbol{P}_{gs,2} \leq \mathbf{0} \tag{3.21}$$

$$\left\{\left(\boldsymbol{c}_b^i\boldsymbol{P}_{gb,1}^i + \boldsymbol{c}_s^i\boldsymbol{P}_{gs,1}^i\right) - \boldsymbol{c}_{bs,1}^i\boldsymbol{P}_D^{min,i}\right\}\boldsymbol{dt}^i \leq \boldsymbol{obj}^i \tag{3.22}$$

$$\left\{\left(\boldsymbol{c}_b^i\boldsymbol{P}_{gb,2}^i + \boldsymbol{c}_s^i\boldsymbol{P}_{gs,2}^i\right) - \boldsymbol{c}_{bs,2}^i\boldsymbol{P}_D^{max,i}\right\}\boldsymbol{dt}^i \leq \boldsymbol{obj}^i \tag{3.23}$$

Table 3.1: Resulting Constraints of the Intuitive Robust Optimization Problem under Different Operational Conditions

Charge/Discharge Condition	$\boldsymbol{obj}^i/\boldsymbol{dt}^i \geq$
$0 \leq \boldsymbol{P}_D^{min,i} \leq \boldsymbol{P}_D^{max,i} \leq \boldsymbol{P}_{dis}^i$	$-\boldsymbol{c}_b^i \boldsymbol{P}_D^{min,i} - \boldsymbol{c}_s^i \left(\boldsymbol{P}_{dis}^i - \boldsymbol{P}_D^{min,i} \right)$
$0 \leq \boldsymbol{P}_D^{min,i} \leq \boldsymbol{P}_{dis}^i \leq \boldsymbol{P}_D^{max,i}$	$-\boldsymbol{c}_b^i \boldsymbol{P}_D^{min,i} - \boldsymbol{c}_s^i \left(\boldsymbol{P}_{dis}^i - \boldsymbol{P}_D^{min,i} \right)$
$0 \leq \boldsymbol{P}_{dis}^i \leq \boldsymbol{P}_D^{min,i} \leq \boldsymbol{P}_D^{max,i}$	$-\boldsymbol{c}_b^i \boldsymbol{P}_{dis}^i$
$-\boldsymbol{P}_{chg}^i \leq 0 \leq \boldsymbol{P}_D^{min,i} \leq \boldsymbol{P}_D^{max,i}$	$+\boldsymbol{c}_b^i \boldsymbol{P}_{chg}^i$
$-\boldsymbol{P}_{chg}^i \leq \boldsymbol{P}_D^{min,i} \leq \boldsymbol{P}_D^{max,i} \leq 0$	$-\boldsymbol{c}_s^i \boldsymbol{P}_D^{max,i} + \boldsymbol{c}_b^i \left(\boldsymbol{P}_{chg}^i + \boldsymbol{P}_D^{max,i} \right)$
$\boldsymbol{P}_D^{min,i} \leq -\boldsymbol{P}_{chg}^i \leq \boldsymbol{P}_D^{max,i} \leq 0$	$-\boldsymbol{c}_s^i \boldsymbol{P}_D^{max,i} + \boldsymbol{c}_b^i \left(\boldsymbol{P}_{chg}^i + \boldsymbol{P}_D^{max,i} \right)$
$\boldsymbol{P}_D^{min,i} \leq \boldsymbol{P}_D^{max,i} \leq -\boldsymbol{P}_{chg}^i \leq 0$	$+\boldsymbol{c}_s^i \boldsymbol{P}_{chg}^i$
$\boldsymbol{P}_D^{min,i} \leq \boldsymbol{P}_D^{max,i} \leq 0 \leq \boldsymbol{P}_{dis}^i$	$-\boldsymbol{c}_s^i \boldsymbol{P}_{dis}^i$
$-\boldsymbol{P}_{chg}^i \leq \boldsymbol{P}_D^{min,i} \leq 0 \leq \boldsymbol{P}_D^{max,i}$	$+\boldsymbol{c}_b^i \boldsymbol{P}_{chg}^i$
$\boldsymbol{P}_D^{min,i} \leq -\boldsymbol{P}_{chg}^i \leq 0 \leq \boldsymbol{P}_D^{max,i}$	$+\boldsymbol{c}_b^i \boldsymbol{P}_{chg}^i$
$\boldsymbol{P}_D^{min,i} \leq 0 \leq \boldsymbol{P}_{dis}^i \leq \boldsymbol{P}_D^{max,i}$	$-\boldsymbol{c}_s^i \boldsymbol{P}_{dis}^i$
$\boldsymbol{P}_D^{min,i} \leq 0 \leq \boldsymbol{P}_D^{max,i} \leq \boldsymbol{P}_{dis}^i$	$-\boldsymbol{c}_s^i \boldsymbol{P}_{dis}^i$

where $\boldsymbol{obj}$ represents the worst case benefit in each time step. Predicted net demand $\boldsymbol{P}_D$ in (3.11) and (3.12) is replaced with its extreme error thresholds $\boldsymbol{P}_D^{min}$ and $\boldsymbol{P}_D^{max}$. Constraints (3.22) and (3.23) limit the worst case benefit as a worse one between the benefits under extreme error conditions. Table 3.1 lists the conditional result of (3.16)–(3.23) under different conditions.

The intuitive robust control problem (3.15)–(3.23) has $9N_t$ variables and $12N_t$ constraints. Although the intuitive assumption about the worst case benefit has not yet been proven, the ESS power partitioning approach [117] could help its certification.

3.3.4 ESS Power Partitioning Approach

Despite its complex problem structure, the ESS power partitioning approach can provide a mathematical proof of the robust optimization. It attempts to remove the equality constraints and duplicated uncertain constants so that the robust counterpart optimization technique can be applied [127].

Fig. 3.4 presents the graphical explanation of this approach. In the case of positive demand conditions shown in Fig. 3.4(a) and Fig. 3.4(b), the microgrid has to buy the unbalanced demand from the main grid. Portion $\boldsymbol{P}_{db}$ of discharge power $\boldsymbol{P}_{dis}$ first replaces this buying demand. If the discharge power is higher than the demand, surplus portion $\boldsymbol{P}_{ds}$ is sold to the main grid. Uncertain portion $\boldsymbol{P}_{du}$ represents the uncertain combination of these portions depending on the uncertain $\boldsymbol{P}_D$ value. Portions of charge power $\boldsymbol{P}_{chg}$ are partitioned similarly. After the partitioning, the grid power

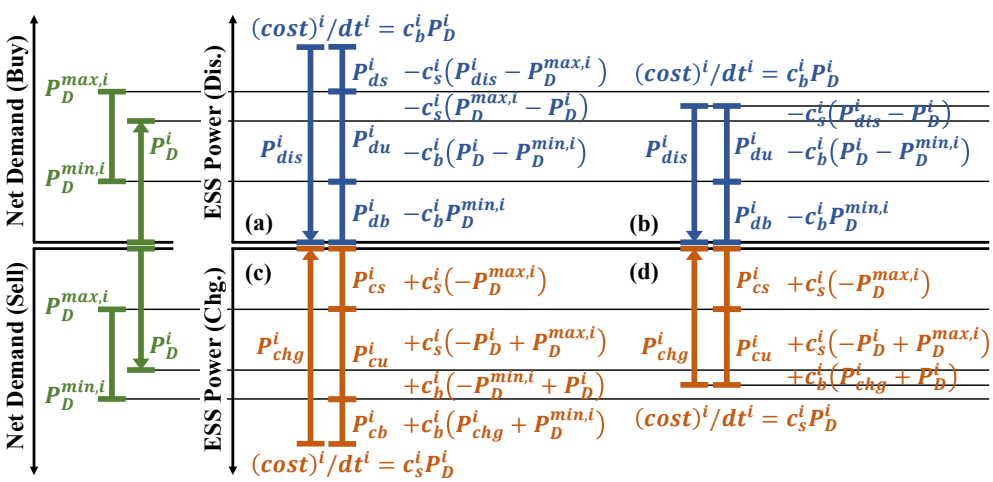

Figure 3.4: ESS power partitioning approach to disregard the uncertain net demand power. Four out of twelve possible conditions in Table 3.1 are presented. (a) High discharge, definitely positive demand (1st). (b) Medium discharge, definitely positive demand (2nd). (c) High charge, definitely negative demand (5th). (d) Medium charge, definitely negative demand (6th).

usage cost (3.10) is converted into

$$\begin{aligned}(\text{Cost}) = &(\boldsymbol{c}_{bs} \circ \boldsymbol{P}_D)^\intercal \, \boldsymbol{dt} \\ &- (\boldsymbol{c}_b \circ \boldsymbol{P}_{db} + \boldsymbol{c}_{u,dis} \circ \boldsymbol{P}_{du} + \boldsymbol{c}_s \circ \boldsymbol{P}_{ds})^\intercal \, \boldsymbol{dt} \\ &+ (\boldsymbol{c}_s \circ \boldsymbol{P}_{cs} + \boldsymbol{c}_{u,chg} \circ \boldsymbol{P}_{cu} + \boldsymbol{c}_b \circ \boldsymbol{P}_{cb})^\intercal \, \boldsymbol{dt}\end{aligned} \tag{3.24}$$

where unit-price vectors $\boldsymbol{c}_{u,chg}$ and $\boldsymbol{c}_{u,dis}$ represent the uncertain combinations of the buying and selling portions. Each of their elements $\boldsymbol{c}^i_{u,chg}$ or $\boldsymbol{c}^i_{u,dis}$ is an uncertain value between $\boldsymbol{c}^i_b$ and $\boldsymbol{c}^i_s$.

The first term of the objective cost in (3.24), which contains the uncertain value $\boldsymbol{P}_D$, can be removed by considering only the economic benefit and not the whole power transaction cost. It is the same approach as applied to (3.11). Demand prediction uncertainty $\boldsymbol{P}_D$ is now fully converted into two independent unit-price uncertainties $\boldsymbol{c}_{u,chg}$ and $\boldsymbol{c}_{u,dis}$. If the interval-type uncertainties are assumed again for the two, the robust counterpart form of the control problem that considers the worst case economic benefit is derived as

$$\underset{obj}{\text{minimize}} \; obj \tag{3.25}$$

$$\begin{aligned}\text{s.t.} \quad &- (\boldsymbol{c}_b \circ \boldsymbol{P}_{db} + \boldsymbol{c}_s \circ \boldsymbol{P}_{du} + \boldsymbol{c}_s \circ \boldsymbol{P}_{ds})^\intercal \, \boldsymbol{dt} \\ &+ (\boldsymbol{c}_s \circ \boldsymbol{P}_{cs} + \boldsymbol{c}_b \circ \boldsymbol{P}_{cu} + \boldsymbol{c}_b \circ \boldsymbol{P}_{cb})^\intercal \, \boldsymbol{dt} \leq obj\end{aligned} \tag{3.26}$$

where obj represents the worst case benefit of the entire period.

Fig. 3.4(a) can provide a simple explanation of (3.26). The worst case economic benefit occurs when uncertain $\boldsymbol{P}^i_D$ is equal to $\boldsymbol{P}^{min,i}_D$ so that $\boldsymbol{c}^i_{u,dis}$ of (3.24) has its lowest value $\boldsymbol{c}^i_s$.

Considering the power trading condition and robust counterpart optimization, the following constraints are applied:

$$\boldsymbol{P}_{chg}^{min,i}\boldsymbol{\delta}_{chg}^{i} \leq \boldsymbol{P}_{cs}^{i} + \boldsymbol{P}_{cb}^{i} + \boldsymbol{P}_{cu}^{i} \leq \boldsymbol{P}_{chg}^{max,i}\boldsymbol{\delta}_{chg}^{i} \tag{3.27}$$

$$\boldsymbol{P}_{dis}^{min,i}\boldsymbol{\delta}_{dis}^{i} \leq \boldsymbol{P}_{db}^{i} + \boldsymbol{P}_{ds}^{i} + \boldsymbol{P}_{du}^{i} \leq \boldsymbol{P}_{dis}^{max,i}\boldsymbol{\delta}_{dis}^{i} \tag{3.28}$$

$$\boldsymbol{P}_{cs}^{max,i}\boldsymbol{\delta}_{bs,1}^{i} \leq \boldsymbol{P}_{cs}^{i} \leq \boldsymbol{P}_{cs}^{max,i} \tag{3.29}$$

$$0 \leq \boldsymbol{P}_{cb}^{i} \leq \boldsymbol{P}_{chg}^{max,i}\boldsymbol{\delta}_{bs,1}^{i} \tag{3.30}$$

$$\boldsymbol{P}_{db}^{max,i}\left(1-\boldsymbol{\delta}_{bs,2}^{i}\right) \leq \boldsymbol{P}_{db}^{i} \leq \boldsymbol{P}_{db}^{max,i} \tag{3.31}$$

$$0 \leq \boldsymbol{P}_{ds}^{i} \leq \boldsymbol{P}_{dis}^{max,i}\left(1-\boldsymbol{\delta}_{bs,2}^{i}\right) \tag{3.32}$$

$$\boldsymbol{P}_{cs}^{max,i}\boldsymbol{\delta}_{bs,2}^{i} \leq \boldsymbol{P}_{cs}^{i} \tag{3.33}$$

$$\boldsymbol{P}_{cu}^{max,i}\boldsymbol{\delta}_{bs,1}^{i} \leq \boldsymbol{P}_{cu}^{i} \leq \boldsymbol{P}_{cu}^{max,i}\boldsymbol{\delta}_{bs,2}^{i} \tag{3.34}$$

$$\boldsymbol{P}_{db}^{max,i}\left(1-\boldsymbol{\delta}_{bs,1}^{i}\right) \leq \boldsymbol{P}_{db}^{i} \tag{3.35}$$

$$\boldsymbol{P}_{du}^{max,i}\left(1-\boldsymbol{\delta}_{bs,2}^{i}\right) \leq \boldsymbol{P}_{du}^{i} \leq \boldsymbol{P}_{du}^{max,i}\left(1-\boldsymbol{\delta}_{bs,1}^{i}\right) \tag{3.36}$$

where $\boldsymbol{\delta}_{bs,1}$ and $\boldsymbol{\delta}_{bs,2}$ are the binary vectors for the power trading condition, as presented in Table 3.2.

Table 3.2: Grid Trading Decision Table

$\boldsymbol{\delta}_{bs,1}^{i}$	$\boldsymbol{\delta}_{bs,2}^{i}$	Power Trading Condition
0	0	selling to the main grid
0	1	uncertain
1	0	infeasible
1	1	buying from the main grid

The upper limitation of each power portion is derived from its definition:

$$\boldsymbol{P}_{cs}^{max,i} = \min\left(\max\left(0, -\boldsymbol{P}_{D}^{max,i}\right), \boldsymbol{P}_{chg}^{max,i}\right) \tag{3.37}$$

$$\boldsymbol{P}_{db}^{max,i} = \min\left(\max\left(0, \boldsymbol{P}_{D}^{min,i}\right), \boldsymbol{P}_{dis}^{max,i}\right) \tag{3.38}$$

$$\boldsymbol{P}_{cu}^{max,i} = \min\left(\boldsymbol{P}_{chg}^{max,i}, \min\left(0, \boldsymbol{P}_{D}^{max,i}\right) - \min\left(0, \boldsymbol{P}_{D}^{min,i}\right)\right) \tag{3.39}$$

$$\boldsymbol{P}_{du}^{max,i} = \min\left(\boldsymbol{P}_{dis}^{max,i}, \max\left(0, \boldsymbol{P}_{D}^{max,i}\right) - \max\left(0, \boldsymbol{P}_{D}^{min,i}\right)\right). \tag{3.40}$$

The ESS power limitations in (3.3) and (3.4) are replaced by those in (3.27) and (3.28). The control problem (3.25), (3.26), and (3.29)–(3.36) generates the same results as in Table 3.1 with $8N_t + 1$ variables and $14N_t + 1$ constraints. It is proved that the intuitive approach is correct and provides an easier explanation.

3.3.5 Combined Constraint Approach

A more concise form of the robust control problem can be formulated by combining its similar constraints. Table 3.3 lists the compressed conditions for the result of the intuitive approach in Table 3.1. Two binary vector variables $\boldsymbol{\delta}_{D,+}$ and $\boldsymbol{\delta}_{D,-}$ are

Table 3.3: Compressed Conditions of the Intuitive Approach

Charge/Discharge Condition	$\boldsymbol{obj}^i/\boldsymbol{dt}^i \geq$
$\boldsymbol{P}_{D}^{min,i} \leq 0 \leq \boldsymbol{P}_{dis}^{i}$	$-\boldsymbol{c}_{s}^{i}\boldsymbol{P}_{dis}^{i}$
$0 \leq \boldsymbol{P}_{D}^{min,i} \leq \boldsymbol{P}_{dis}^{i}$	$-\left(\boldsymbol{c}_{b}^{i} - \boldsymbol{c}_{s}^{i}\right)\boldsymbol{P}_{D}^{min,i} - \boldsymbol{c}_{s}^{i}\boldsymbol{P}_{dis}^{i}$
$0 \leq \boldsymbol{P}_{dis}^{i} \leq \boldsymbol{P}_{D}^{min,i}$	$-\boldsymbol{c}_{b}^{i}\boldsymbol{P}_{dis}^{i}$
$\boldsymbol{P}_{D}^{max,i} \leq -\boldsymbol{P}_{chg}^{i} \leq 0$	$+\boldsymbol{c}_{s}^{i}\boldsymbol{P}_{chg}^{i}$
$-\boldsymbol{P}_{chg}^{i} \leq \boldsymbol{P}_{D}^{max,i} \leq 0$	$\left(\boldsymbol{c}_{b}^{i} - \boldsymbol{c}_{s}^{i}\right)\boldsymbol{P}_{D}^{max,i} + \boldsymbol{c}_{b}^{i}\boldsymbol{P}_{chg}^{i}$
$-\boldsymbol{P}_{chg}^{i} \leq 0 \leq \boldsymbol{P}_{D}^{max,i}$	$+\boldsymbol{c}_{b}^{i}\boldsymbol{P}_{chg}^{i}$

introduced to combine the remaining conditions:

$$-P_{line}^{limit}\left(\mathbf{1}-\boldsymbol{\delta}_{D,+}\right) \leq \boldsymbol{P}_{D}^{min} \circ \boldsymbol{\delta}_{D,+} \tag{3.41}$$

$$\boldsymbol{P}_{D}^{max} \circ \boldsymbol{\delta}_{D,-} \leq P_{line}^{limit}\left(\mathbf{1}-\boldsymbol{\delta}_{D,-}\right). \tag{3.42}$$

The concise form of the robust optimal control problem with combined constraints is derived as

$$\text{minimize } \mathbf{1}^{\intercal}\boldsymbol{obj} \tag{3.43}$$

$$\text{s.t. } \left\{-\left(\boldsymbol{c}_{b}^{i}-\boldsymbol{c}_{s}^{i}\right)\boldsymbol{P}_{D}^{min,i}\boldsymbol{\delta}_{D,+}^{i}-\boldsymbol{c}_{s}^{i}\boldsymbol{P}_{dis}^{i}+\boldsymbol{c}_{s}^{i}\boldsymbol{P}_{chg}^{i}\right\}\boldsymbol{dt}^{i} \leq \boldsymbol{obj}^{i} \tag{3.44}$$

$$\left\{+\left(\boldsymbol{c}_{b}^{i}-\boldsymbol{c}_{s}^{i}\right)\boldsymbol{P}_{D}^{max,i}\boldsymbol{\delta}_{D,-}^{i}-\boldsymbol{c}_{b}^{i}\boldsymbol{P}_{dis}^{i}+\boldsymbol{c}_{b}^{i}\boldsymbol{P}_{chg}^{i}\right\}\boldsymbol{dt}^{i} \leq \boldsymbol{obj}^{i}. \tag{3.45}$$

The combination of the binary elements $\boldsymbol{\delta}_{D,+}^{i}$ and $\boldsymbol{\delta}_{D,-}^{i}$ indicates the range of an uncertain net demand in each time step. Because the control problem tries to minimize the objective in (3.43), the feasible combination that produces the lowest $\boldsymbol{obj}^{i}$ limitation value in (3.44) and (3.45) is selected as the optimum set.

The concise form of the control problem (3.41)–(3.45) has only $4N_t$ variables and $4N_t$ constraints except for the binary variable limitations. It provides the same robust control results as those listed in Table 3.3 within a shorter computation time. Furthermore, it can replace the non-robust control problem (3.11)–(3.14) by applying uncertain net demand $\boldsymbol{P}_D$ itself, thereby providing a faster computation time.

3.4 ESS Efficiency Maps

The previously proposed simple ESS model (3.1)–(3.7) uses fixed efficiency value vectors $\boldsymbol{\eta}_{dis}$ and $\boldsymbol{\eta}_{chg}$ for its SOC calculation. To improve the accuracy of the ESS model, the extended model proposed in this study uses 2D efficiency maps. The 2D efficiency maps of the power and SOC are introduced to provide more precise optimization result than that from a constant efficiency value. It enables the EMS to safely control the ESS without violating its SOC limitations.

The efficiency maps of a massive vanadium redox flow battery system installed in the target microgrid are presented in Fig. 3.5. They are generated from the experimental results and known trend information [123]. To handle the nonlinearity of the efficiency maps, the ESS SOC model is piecewise linearized using the sampled power and SOC values:

$$\boldsymbol{P}_{dis}^{min,i} = \boldsymbol{P}_{dis,1}^{i} \leq \boldsymbol{P}_{dis,l}^{i} \leq \boldsymbol{P}_{dis,N_{dis}}^{i} = \boldsymbol{P}_{dis}^{max,i} \tag{3.46}$$

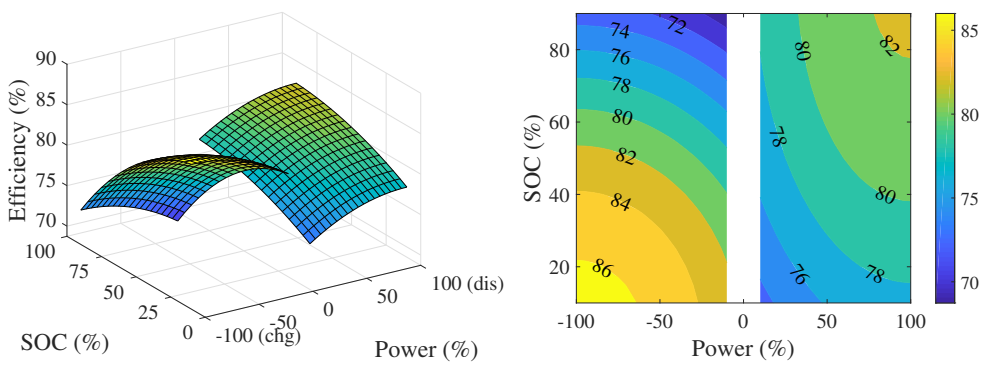

(a) Surface plot (b) Contour plot

Figure 3.5: Graphical presentations of the installed vanadium redox flow battery system charge/discharge efficiency maps. (a) Surface plot. (b) Contour plot.

$$\boldsymbol{P}_{chg}^{min,i} = \boldsymbol{P}_{chg,1}^{i} \leq \boldsymbol{P}_{chg,l}^{i} \leq \boldsymbol{P}_{chg,N_{chg}}^{i} = \boldsymbol{P}_{chg}^{max,i} \tag{3.47}$$

$$\boldsymbol{S}^{min,i} = \boldsymbol{S}_{1}^{i} \leq \boldsymbol{S}_{m}^{i} \leq \boldsymbol{S}_{N_S}^{i} = \boldsymbol{S}^{max,i} \tag{3.48}$$

where $\boldsymbol{P}_{chg,l}^{i}$, $\boldsymbol{P}_{dis,l}^{i}$, and $\boldsymbol{S}_{m}^{i}$ are the sampled power and SOC constants in each time step i. $\boldsymbol{P}_{chg}^{i}$, $\boldsymbol{P}_{dis}^{i}$, and $\boldsymbol{S}^{i}$ are sampled by N_{dis}, N_{chg}, and N_S times, respectively. The SOC limitation in (3.7) can be rewritten using the sampled values. Binary variable $\boldsymbol{\delta}_{S,m}^{i}$ represents the SOC location within the sampled value ranges:

$$\sum_{m=1}^{N_S-1} \boldsymbol{S}_{m}^{i} \boldsymbol{\delta}_{S,m}^{i} \leq \boldsymbol{S}^{i} \leq \sum_{m=1}^{N_S-1} \boldsymbol{S}_{m+1}^{i} \boldsymbol{\delta}_{S,m}^{i}, \quad \sum_{m=1}^{N_S-1} \boldsymbol{\delta}_{S,m}^{i} = 1. \tag{3.49}$$

The power limitations in (3.3) and (3.4) are also redefined:

$$\boldsymbol{P}_{dis}^{i} = \sum_{l=1}^{N_{dis}} \boldsymbol{P}_{dis,l}^{i} \boldsymbol{\theta}_{dis,l}^{i}, \quad \sum_{l=1}^{N_{dis}} \boldsymbol{\theta}_{dis,l}^{i} = \boldsymbol{\delta}_{dis}^{i} \tag{3.50}$$

$$\boldsymbol{P}_{chg}^{i} = \sum_{l=1}^{N_{chg}} \boldsymbol{P}_{chg,l}^{i} \boldsymbol{\theta}_{chg,l}^{i}, \quad \sum_{l=1}^{N_{chg}} \boldsymbol{\theta}_{chg,l}^{i} = \boldsymbol{\delta}_{chg}^{i} \tag{3.51}$$

where $\boldsymbol{\theta}_{dis}^{i}$ is a special ordered set of type 2 (SOS2) [128] representing the weights of the samples. At most two adjacent elements of $\boldsymbol{\theta}_{dis}^{i}$ may take positive values in each time step. $\boldsymbol{\theta}_{chg}^{i}$ is the same. If an MILP solver does not support a special ordered set, additional constraints are required [129]:

$$\sum_{l=1}^{N_{dis}-1} \boldsymbol{P}_{dis,l}^{i} \boldsymbol{\delta}_{dis,l}^{i} \leq \boldsymbol{P}_{dis}^{i} \leq \sum_{l=1}^{N_{dis}-1} \boldsymbol{P}_{dis,l+1}^{i} \boldsymbol{\delta}_{dis,l}^{i} \tag{3.52}$$

$$\sum_{l=1}^{N_{chg}-1} \boldsymbol{P}_{chg,l}^{i} \boldsymbol{\delta}_{chg,l}^{i} \leq \boldsymbol{P}_{chg}^{i} \leq \sum_{l=1}^{N_{chg}-1} \boldsymbol{P}_{chg,l+1}^{i} \boldsymbol{\delta}_{chg,l}^{i} \tag{3.53}$$

$$\sum_{l=1}^{N_{dis}-1} \boldsymbol{\delta}^i_{dis,l} = \boldsymbol{\delta}^i_{dis}, \qquad \sum_{l=1}^{N_{chg}-1} \boldsymbol{\delta}^i_{chg,l} = \boldsymbol{\delta}^i_{chg} \tag{3.54}$$

and the special ordered sets are now defined as

$$\boldsymbol{\theta}^i_{dis,1} \leq \boldsymbol{\delta}^i_{dis,1}, \qquad \boldsymbol{\theta}^i_{dis,N_{dis}} \leq \boldsymbol{\delta}^i_{dis,N_{dis}-1}, \tag{3.55}$$

$$\boldsymbol{\theta}^i_{dis,l} \leq \boldsymbol{\delta}^i_{dis,l-1} + \boldsymbol{\delta}^i_{dis,l} \qquad \forall l \in \{2, ..., N_{dis}-1\} \tag{3.56}$$

$$\boldsymbol{\theta}^i_{chg,1} \leq \boldsymbol{\delta}^i_{chg,1}, \qquad \boldsymbol{\theta}^i_{chg,N_{chg}} \leq \boldsymbol{\delta}^i_{chg,N_{chg}-1}, \tag{3.57}$$

$$\boldsymbol{\theta}^i_{chg,l} \leq \boldsymbol{\delta}^i_{chg,l-1} + \boldsymbol{\delta}^i_{chg,l} \quad \forall l \in \{2, ..., N_{chg}-1\}. \tag{3.58}$$

The step-wise increase or decrease of the ESS energy is also sampled with respect to the sampled power and SOC:

$$\boldsymbol{dE}^i_{dis,lm} = \boldsymbol{P}^i_{dis,l} \ / \ \eta_{dis}\left(\boldsymbol{P}^i_{dis,l}, 0.5\left(\boldsymbol{S}^i_m + \boldsymbol{S}^i_{m+1}\right)\right) \tag{3.59}$$

$$\boldsymbol{dE}^i_{chg,lm} = \boldsymbol{P}^i_{chg,l} \times \eta_{chg}\left(\boldsymbol{P}^i_{chg,l}, 0.5\left(\boldsymbol{S}^i_m + \boldsymbol{S}^i_{m+1}\right)\right) \tag{3.60}$$

where $\eta_{chg}\left(P, S\right)$ and $\eta_{dis}\left(P, S\right)$ are the 2D efficiency map functions and $\boldsymbol{dE}^i_{chg,lm}$ and $\boldsymbol{dE}^i_{dis,lm}$ are the sampled effects.

The ESS SOC model (3.6) is now simply linearized as

$$\boldsymbol{S}^{i+1} = \boldsymbol{S}^1 - \sum_{k=1}^{i} \boldsymbol{dt}^k \boldsymbol{dE}^k / ECap \tag{3.61}$$

where $\boldsymbol{dE}^i$ represents the step-wise change in the ESS energy at the time step i. It is

selected from sampled values $\boldsymbol{dE}^i_{chg,lm}$ and $\boldsymbol{dE}^i_{dis,lm}$ by the following condition:

$$\begin{aligned}
&\left(\boldsymbol{\delta}^i_{S,m} - 1\right)\left\{\max_l\left(\boldsymbol{dE}^i_{dis,lm}\right) + \max_l\left(\boldsymbol{dE}^i_{chg,lm}\right)\right\} \\
&\leq \boldsymbol{dE}^i - \sum_{l=1}^{N_{dis}} \boldsymbol{dE}^i_{dis,lm}\boldsymbol{\theta}^i_{dis,l} + \sum_{l=1}^{N_{chg}} \boldsymbol{dE}^i_{chg,lm}\boldsymbol{\theta}^i_{chg,l} \\
&\leq \left(1 - \boldsymbol{\delta}^i_{S,m}\right)\left\{\max_l\left(\boldsymbol{dE}^i_{dis,lm}\right) + \max_l\left(\boldsymbol{dE}^i_{chg,lm}\right)\right\}.
\end{aligned} \tag{3.62}$$

For each SOC-sample index m, $\boldsymbol{dE}^i$ is determined as the sum of the weighted sample values when $\boldsymbol{\delta}^i_{S,m}$ represents the current SOC location as its value one. The weights are determined by the current power value with corresponding special ordered sets $\boldsymbol{\theta}^i_{chg,l}$ and $\boldsymbol{\theta}^i_{dis,l}$.

3.5 External Working Conditions

Microgrid operating limitations that are not specified in the initial EMS specifications can be dynamically applied to the optimal control problem as external working conditions. It is possible to achieve both robust optimal control and additional power limitations by applying them to an online optimization process. For example, the main grid operator can handle a temporary power shortage by sending a peak control condition to the event server shown in Fig. 3.2.

Two types of grid ancillary services are introduced as external working conditions in this study. The peak control (PC) condition defines the peak power limitation. The demand response (DR) condition represents the energy conservation during a specific period. Each condition includes energy and time parameters.

3.5.1 Peak Control

The PC condition defines the peak power limitation of the active DER or the whole microgrid. Its most common application is the limitation of the grid-buying power. Under a power shortage situation, grid-level blackout can be prevented by applying the PC conditions to the grid-connected microgrids.

A grid-buying PC condition within the time-step range $i \in \left[i^{start}_{PC,g,buy}, i^{end}_{PC,g,buy} \right]$ is considered. The following limitation for the peak power has to be additionally applied to the robust optimal problem:

$$\boldsymbol{P}^{max,i}_{D} - \boldsymbol{P}^{i}_{dis} + \boldsymbol{P}^{i}_{chg} \leq \boldsymbol{P}^{i}_{PC,g,buy} + \boldsymbol{P}^{fail,i}_{PC,g,buy} \tag{3.63}$$

where $\boldsymbol{P}_{PC,g,buy}$ is the defined power limit value vector and $\boldsymbol{P}^{fail}_{PC,g,buy}$ is the non-negative failure amount vector. If the EMS fails to control the peak power under the limit value, the excess amount value is identified as $\boldsymbol{P}^{fail}_{PC,g,buy}$. The upper bound of the PC failure value is expressed as

$$\boldsymbol{P}^{fail,i}_{PC,g,buy} \leq \left(\boldsymbol{P}^{max,i}_{D} + \boldsymbol{P}^{max,i}_{chg} - \boldsymbol{P}^{i}_{PC,g,buy} \right) \times \left(1 - \boldsymbol{\delta}^{i}_{PC,g,buy} \right) \tag{3.64}$$

where $\boldsymbol{\delta}_{PC,g,buy}$ is the binary vector that represents the success/failure state of the PC condition. Even if the target external working condition is too harsh that the EMS cannot satisfy it during the entire condition applied time steps, the optimization process tries to find the best solution by assigning some time steps as failed ones. In this case, the condition is not applied to these failed time steps by assigning the value zero to the binary vector elements.

The objective cost of an external working condition have to be added to the main control problem objective in (3.11), (3.15), (3.25), or (3.43). The cost of the grid-buying PC condition is defined as

$$\sum_{i=i^{start}_{PC,g,buy}}^{i^{end}_{PC,g,buy}} \left\{ c^1_{PC,g,buy} \left(1 + \left(c^2_{PC,g,buy}\right)^i\right) \left(1 - \boldsymbol{\delta}^i_{PC,g,buy}\right) + c^3_{PC,g,buy} \boldsymbol{P}^{fail,i}_{PC,g,buy} \right\} \boldsymbol{dt}^i \tag{3.65}$$

where $c^1_{PC,g,buy}$, $c^2_{PC,g,buy}$, and $c^3_{PC,g,buy}$ are the grid-buying PC failure penalty constants. The aim of the objective cost is to find the maximum possible success states of $\boldsymbol{\delta}^i_{PC,g,buy}$ and to reduce the failure power amount of $\boldsymbol{P}^{fail}_{PC,g,buy}$.

Non-negative penalty constant $c^1_{PC,g,buy}$ represents the effect of the condition failure states. A high value of this penalty constant enables success/failure state vector $\boldsymbol{\delta}_{PC,g,buy}$ to obtain the greatest effect in the full objective cost.

$c^2_{PC,g,buy}$ represents the time dependence of the penalty. If the condition is unsatisfied in some time steps because of the lack of DER capacities, the faster time steps should be satisfied first to gain time. It must have a positive value of less than one to make the time-step index i act as an exponent to prioritize the success states of the faster time steps. It is similar to the time-varying weight concept [119].

$c^3_{PC,g,buy}$ functions as a penalty to reduce the excessive power amount as possible even when the PC condition is not satisfied.

The grid-selling PC condition can be expressed similar to the grid-buying one. A net-zero power usage condition can be also achieved by applying both the grid-buying and grid-selling PC conditions with zero-peak-power limitations. Above con-

cept (3.63)–(3.65) works as the basic formulation for external working conditions.

3.5.2 Demand Response

The DR condition aims to decrease the total grid energy usage during a specific period. The net demand without active DER operations is considered as the reference usage. The EMS tries to find a proper control schedule to achieve energy conservation E_{DR} during time-step range $\left[i_{DR}^{start}, i_{DR}^{end}\right]$:

$$\sum_{i=i_{DR}^{start}}^{i_{DR}^{end}} \left\{ \boldsymbol{P}_{D}^{min,i} - \left(\boldsymbol{P}_{D}^{max,i} - \boldsymbol{P}_{dis}^{i} + \boldsymbol{P}_{chg}^{i} \right) \right\} \boldsymbol{dt}^{i} \geq E_{DR} - E_{DR}^{fail} \tag{3.66}$$

where E_{DR}^{fail} represents the non-negative failure amount for the energy conservation. The minimum and maximum uncertain net demand power boundaries $\boldsymbol{P}_{D}^{min}$ and $\boldsymbol{P}_{D}^{max}$ are applied as the reference and real power usage, respectively, to consider the worst case prediction uncertainty.

The upper bound of the DR failure amount is expressed as

$$E_{DR}^{fail} \leq \left\{ - \sum_{i=i_{DR}^{start}}^{i_{DR}^{end}} \left(\boldsymbol{P}_{D}^{min,i} - \boldsymbol{P}_{D}^{max,i} - \boldsymbol{P}_{chg}^{max,i} \right) \boldsymbol{dt}^{i} + E_{DR} \right\} (1 - \delta_{DR}) \tag{3.67}$$

where δ_{DR} is the DR success state binary vector. The DR condition is robustly satisfied under the worst case prediction uncertainty consideration if δ_{DR} has a success state value of one so that non-negative failure amount E_{DR}^{fail} has a value of zero.

The objective cost of the DR condition is defined as

$$c_{DR}^{1}\left(1+\left(c_{DR}^{2}\right)^{\text{(DR ID Number)}}\right)\left(1-\delta_{DR}\right)+c_{DR}^{3}E_{DR}^{fail} \tag{3.68}$$

where c_{DR}^{1}, c_{DR}^{2}, and c_{DR}^{3} are the DR failure penalty constants. If several DR conditions are applied at once, c_{DR}^{2} prioritizes each objective cost using their ID numbers.

3.6 Simulation Results

3.6.1 Computation Time

Table 3.4: Objective and Constraint Equations of the Full Robust Optimal Control Problem (Part 1)

Model	Objective	Constraints (Power & Cost)	Constraints (SOC)
Non-Robust	(3.11)	(3.12)–(3.14)	
Intuitive	(3.15)	(3.16)–(3.23)	
ESS Power Partitioning	(3.25)	(3.26)–(3.36)	
Combined Constraint	(3.43)	(3.41), (3.42), (3.44), (3.45)	
Simple ESS		(3.3)–(3.5)	(3.6), (3.7)
Extended ESS (w SOS2)		(3.50), (3.51)	(3.49), (3.61), (3.62)
Extended ESS (wo SOS2)		(3.50)–(3.58)	(3.49), (3.61), (3.62)
PC Condition	(3.65)	(3.63), (3.64)	
DR Condition	(3.68)	(3.66), (3.67)	

The objective and constraint equations of the full robust optimal control problem are listed in Tables 3.4 and 3.5. Three robust optimization approaches are tested using IBM ILOG CPLEX MILP solver with 3.4-GHz computing power. The control time

Table 3.5: Objective and Constraint Equations of the Full Robust Optimal Control Problem (Part 2)

Model	Optimization Arguments
Non-Robust	$\boldsymbol{P}_{gb}$, $\boldsymbol{P}_{gs}$, $\boldsymbol{P}_{chg}$, $\boldsymbol{P}_{dis}$, $\boldsymbol{\delta}_{g}$
Intuitive	$\boldsymbol{P}_{gb,1}$, $\boldsymbol{P}_{gs,1}$, $\boldsymbol{P}_{gb,2}$, $\boldsymbol{P}_{gs,2}$, $\boldsymbol{P}_{chg}$, $\boldsymbol{P}_{dis}$, $\boldsymbol{\delta}_{g,1}$, $\boldsymbol{\delta}_{g,2}$, $\boldsymbol{obj}$
ESS Power Partitioning	$\boldsymbol{P}_{cs}$, $\boldsymbol{P}_{cu}$, $\boldsymbol{P}_{cb}$, $\boldsymbol{P}_{db}$, $\boldsymbol{P}_{du}$, $\boldsymbol{P}_{ds}$, $\boldsymbol{\delta}_{bs,1}$, $\boldsymbol{\delta}_{bs,2}$, obj
Combined Constraint	$\boldsymbol{P}_{chg}$, $\boldsymbol{P}_{dis}$, $\boldsymbol{\delta}_{D,+}$, $\boldsymbol{\delta}_{D,-}$
Simple ESS	$\boldsymbol{P}_{chg}$, $\boldsymbol{P}_{dis}$, $\boldsymbol{\delta}_{chg}$, $\boldsymbol{\delta}_{dis}$, $\boldsymbol{S}$
Extended ESS (w SOS2)	$\boldsymbol{P}_{chg}$, $\boldsymbol{P}_{dis}$, $\boldsymbol{\delta}_{chg}$, $\boldsymbol{\delta}_{dis}$, $\boldsymbol{\theta}_{chg,l}$, $\boldsymbol{\theta}_{dis,l}$, $\boldsymbol{S}$, $\boldsymbol{\delta}_{S,m}$, $\boldsymbol{dE}$
Extended ESS (wo SOS2)	$\boldsymbol{P}_{chg}$, $\boldsymbol{P}_{dis}$, $\boldsymbol{\delta}_{chg}$, $\boldsymbol{\delta}_{dis}$, $\boldsymbol{\delta}_{chg,l}$, $\boldsymbol{\delta}_{dis,l}$, $\boldsymbol{\theta}_{chg,l}$, $\boldsymbol{\theta}_{dis,l}$, $\boldsymbol{S}$, $\boldsymbol{\delta}_{S,m}$, $\boldsymbol{dE}$
PC Condition	$\boldsymbol{P}_{chg}$, $\boldsymbol{P}_{dis}$, $\boldsymbol{P}^{fail}_{PC,g,buy}$, $\boldsymbol{\delta}_{PC,g,buy}$
DR Condition	$\boldsymbol{P}_{chg}$, $\boldsymbol{P}_{dis}$, E^{fail}_{DR}, δ_{DR}

horizon consists of 1-h-duration time steps. The operating data and DER information of the real microgrid shown in Fig. 3.2 are applied to the simulation. Fig. 3.6 shows the power usage patterns and unit power trading prices that are applied. The net demand prediction error threshold in each time step is set as $\pm$0.5 kW. The efficiency map and external working condition are not applied in the initial simulation.

Fig. 3.7 shows the comparison between the computation times from different approaches. The ESS power partitioning approach takes the longest time. The combined constraint approach takes even a shorter time than the non-robust one. The result shows that the number of constraints in a control problem has the largest effect on the computation time.

Despite the identical worst case cost results of each approach, the real costs can vary depending on an uncertain net demand. Fig. 3.8 presents two 48-h robust control schedules that are generated using the ESS power partitioning approach and

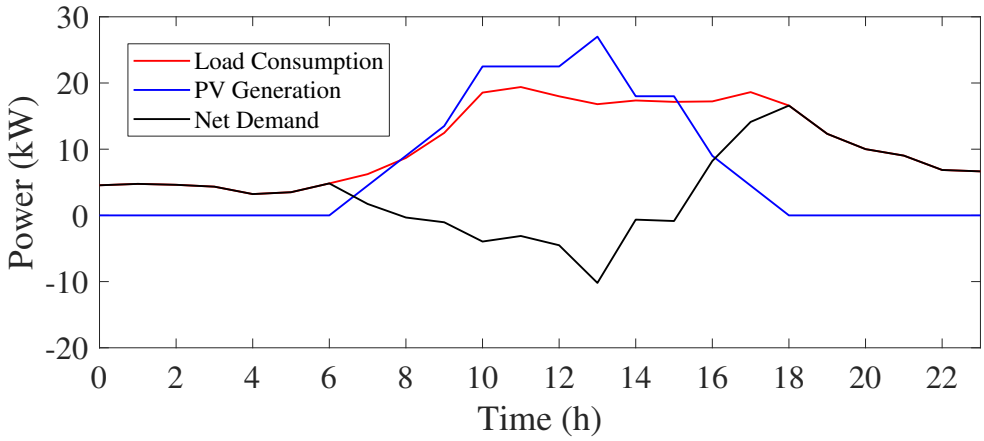

(a) Power usage patterns of the microgrid load, PV, and net demand

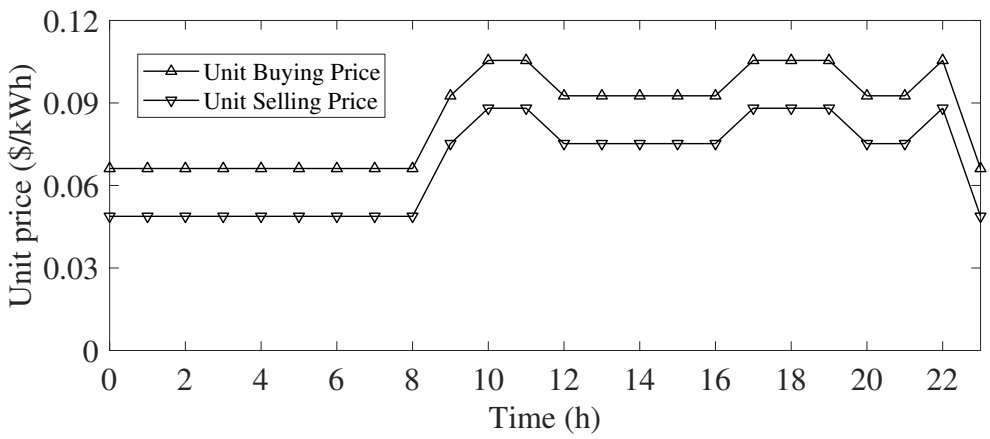

(b) Unit power buying/selling prices of the power trade

Figure 3.6: Operating conditions of a grid-connected microgrid for the control problem input data. (a) Power usage patterns of the microgrid load, PV, and net demand. (b) Unit power buying/selling prices of the power trade.

combined constraint approach. The first schedule tries to charge the ESS in 31 h. The charge power must be bought from the main grid as $+\boldsymbol{c}_b^{31}\boldsymbol{P}_{chg}^{31}\boldsymbol{dt}^{31}$ because an uncertain net demand is definitely positive. By contrast, the second schedule tries to charge the ESS in 32 h, when an uncertain demand can be either positive or negative. The unit buying cost is same as the one in 31 h. If the real demand is

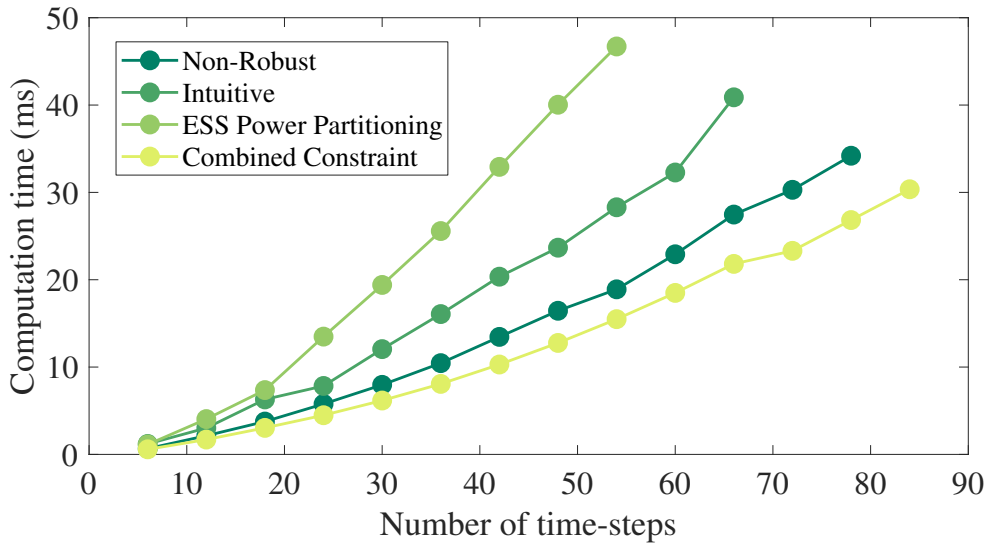

Figure 3.7: Robust optimization computation time for different approaches.

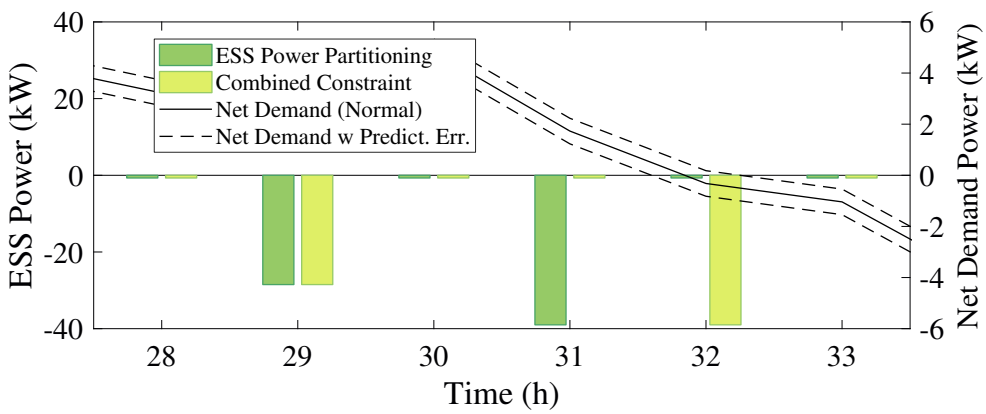

Figure 3.8: Robust optimal control schedules where the worst case cost results are the same but the real costs can differ depending on an uncertain net demand.

positive as the worst case, the charge power must be bought from the main grid, too. If not, the charge power first cancels the selling demand as $+\boldsymbol{c}_s^{32}\left(-\boldsymbol{P}_D^{32}\right)\boldsymbol{dt}^{32}$ $+\boldsymbol{c}_b^{32}\left(\boldsymbol{P}_{chg}^{32}+\boldsymbol{P}_D^{32}\right)\boldsymbol{dt}^{32}$. Two schedules are identical from the viewpoint of robust optimization, however, the latter is better because of its possible lower real cost.

3.6.2 Cost Robustness

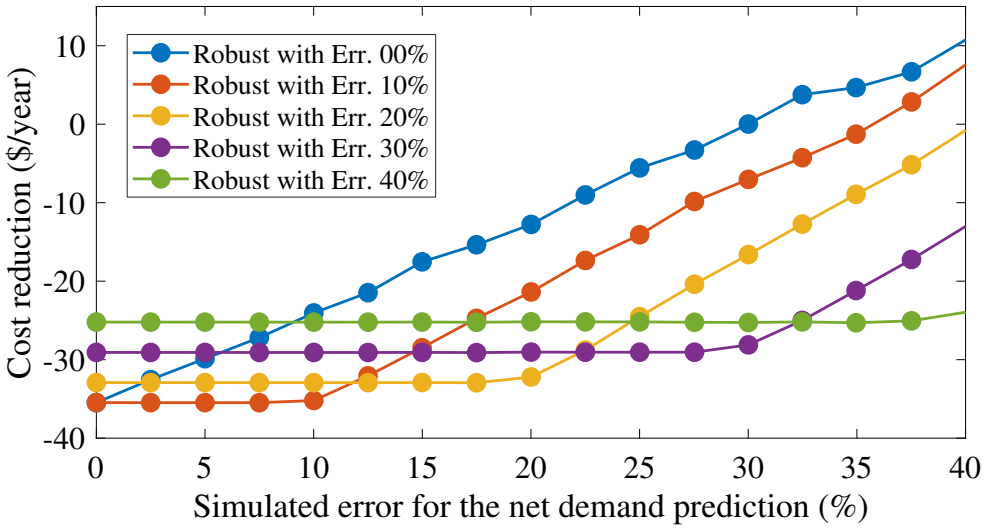

Figure 3.9: Yearly cost reduction for the main grid power usage as a result of the daily robust optimal control. Each strategy targets a different net demand prediction error threshold for the robust optimal control.

To demonstrate the control robustness in terms of cost reduction, robust optimal control schedules are applied to uncertain net demand conditions. The uncertain net demand in each time step contains a normally distributed proportional random noise as the prediction error. It can reduce the economic benefit of a non-robust control as a form of undesirable grid power buying/selling. Each robust control schedule is generated with the consideration for a different net demand error threshold.

Fig. 3.9 presents the yearly cost reduction in the main grid power usage after applying the daily robust control. The robust optimal control schedule can maintain a robustly high level of cost reduction even if the prediction error increases within the target threshold range. Therefore, it shows a better performance than the non-robust one if the error is close to or larger than the threshold.

3.6.3 Precise ESS Control

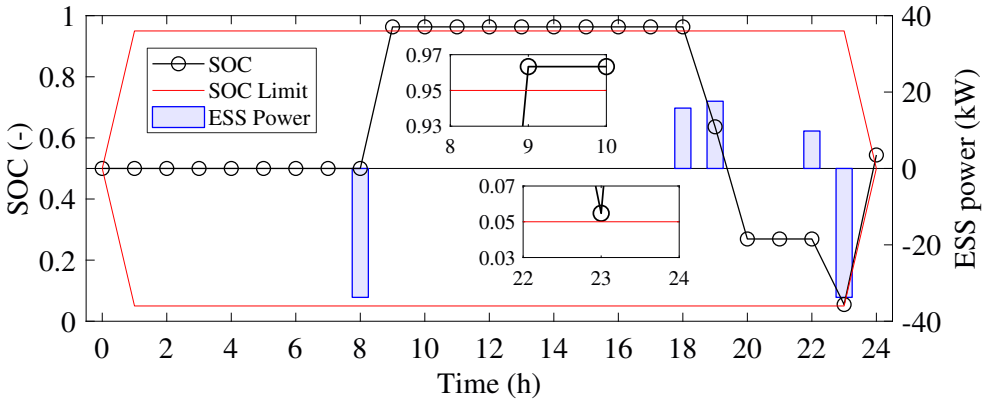

(a) Optimal control result (constant efficiency value)

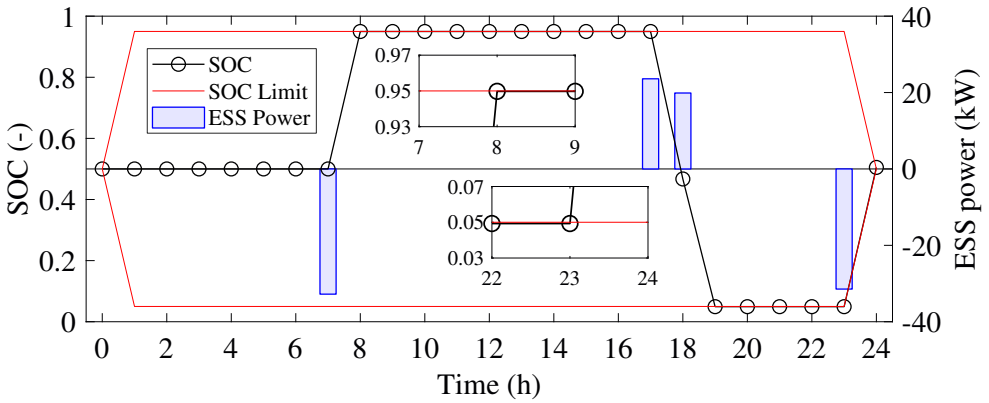

(b) Optimal control result (nonlinear efficiency maps)

Figure 3.10: ESS SOC values in each time step after applying the optimal control schedules. Each schedule is derived using the (a) constant efficiency value and (b) charge and discharge efficiency maps.

The extended ESS model proposed in this study applies nonlinear efficiency maps to its SOC calculation. Separable programming using the piecewise linearization method enables the control problem to remain a mixed-integer linear form. Improved accuracy of the model makes the controller precisely control the ESS without violating the SOC limitations.

Fig. 3.10(a) presents the optimal ESS control schedule derived using the constant efficiency value in the specification. The inaccuracy in the SOC calculation induced by a constant efficiency value can make the real SOC violate its limitations. As a result, the ESS hardware has to block the SOC violations in 9 h and 24 h, which means the optimality of the derived schedule is disrupted. The precise control schedule of Fig. 3.10(b) is free from this problem and can fully use the ESS capacity as shown in 23 h. The charge power, discharge power, and SOC in each time step are independently sampled four times for the piecewise linearized ESS model.

The application of the ESS efficiency maps to the optimization also has an advantage in terms of cost reduction. Fig. 3.11 shows the comparison of the optimal control schedule and the heuristic one. As presented in Fig. 3.5, the charge/discharge efficiency maps applied to the control problem show higher efficiency values under higher power conditions. The optimal control schedule attempts to operate the ESS under higher efficiency regions to minimize its energy loss and the corresponding cost. Compared with the optimal one, the heuristic schedule only considers the unit-price patterns and tries to evenly distribute the power without violating the SOC limitation. It may fall into undesirable efficiency regions because it does not consider the relationship between the efficiency and other conditions. The result presented in Table 3.6 shows that the optimized control schedule effectively decreases the cost by operating the ESS under higher efficiency regions only. By contrast, the heuristic schedule fails to decrease the grid power usage cost because of it makes the ESS operate under lower efficiency regions.

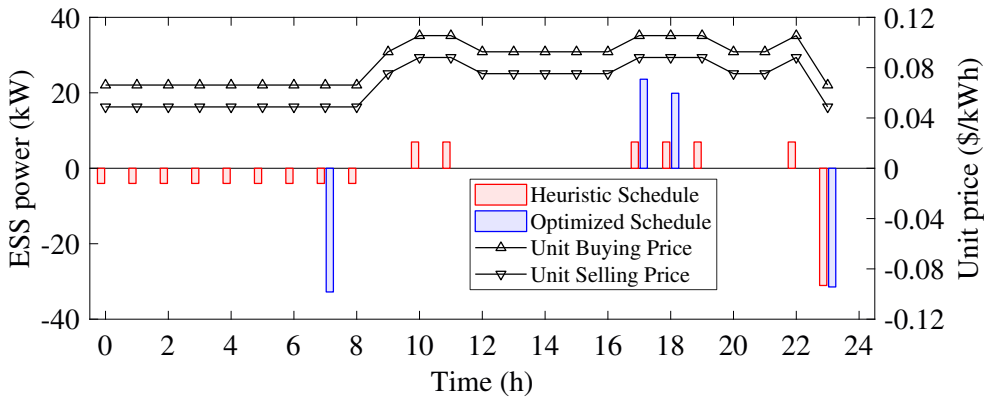

Figure 3.11: An optimal control schedule versus a heuristic one. The optimal control schedule tries to operate the ESS under higher efficiency conditions. By contrast, the heuristic schedule only considers even distribution of the ESS power.

Table 3.6: Optimal Control Considering the ESS Efficiency Map

Control Schedule	No ESS	Heuristic	Optimized
Averaged Efficiency (%)	-	76.458	82.513
Cost Reduction ($/day)	0.000	−0.042	+0.336

3.6.4 External Working Condition

Grid ancillary services such as PC and DR can be applied to the robust optimal control as external working conditions. Penalty constants with appropriate values can force the controller to satisfy these conditions along with considering the cost optimization.

A harsh PC condition of 10-kW grid power limit is applied to the 24-h duration robust optimal control from 16 h to 19 h time steps. Fig. 3.12 presents the resulting ESS control schedule and the corresponding grid power usage. The controller tries to robustly satisfy the PC condition by limiting the maximum possible grid power usage within the PC limit. The ESS is charged in the lowest unit-price time steps to additionally consider the cost optimization.

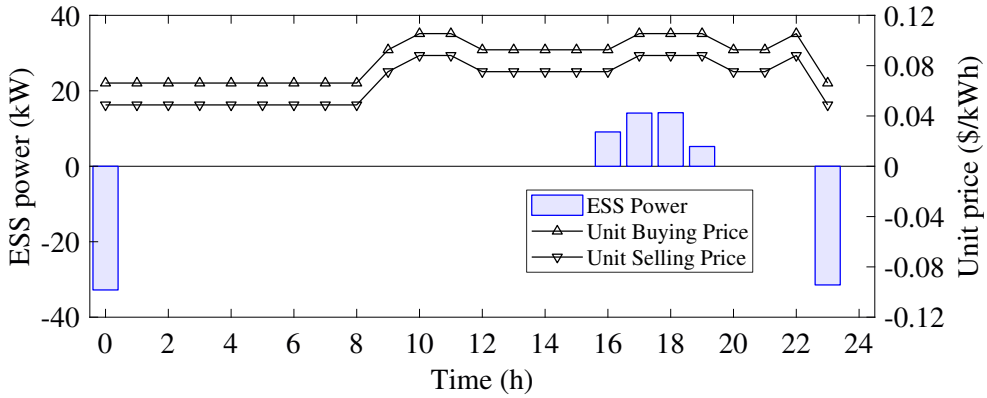

(a) ESS control schedule

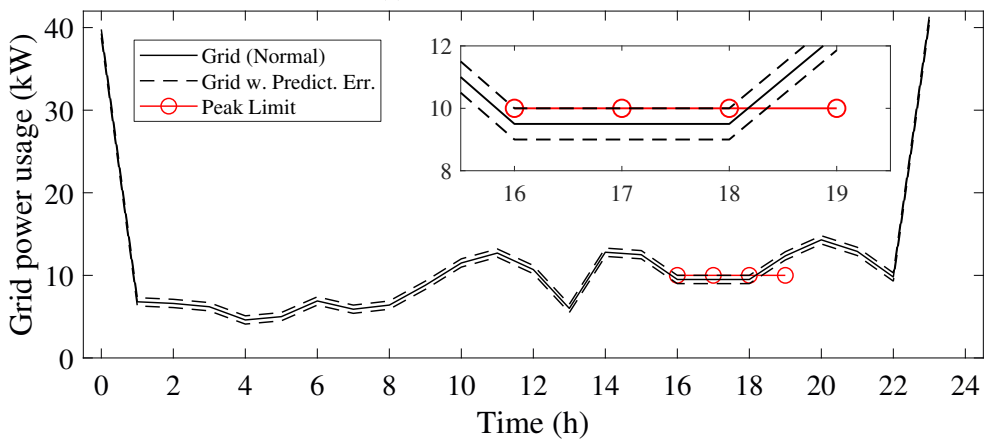

(b) Grid power usage schedule

Figure 3.12: PC result of the robust optimal control under a net demand prediction error threshold of 0.5 kW. (a) ESS control schedule. (b) Main grid power usage schedule with the prediction error threshold.

As shown in Fig. 3.12(b), the controller cannot fully satisfy the harsh PC condition because of the insufficient energy capacity of the ESS. The time dependency of the control penalty makes the controller satisfy the condition from earlier time steps (16–18 h). It helps the microgrid administrator to gain some time to manage the failure by delaying its occurrence.

3.7 Conclusion

This chapter has proposed a robust optimal control strategy for an ESS of a grid-connected microgrid. The prediction uncertainty of the microgrid net demand power can reduce the economic benefit of a non-robust control in the form of undesirable grid power buying/selling. The robust control approaches presented in this chapter aim to maintain a high level of economic benefit regardless of the prediction uncertainty. Three robust optimization approaches have been presented using MILP. The intuitive approach provides a logical background for robust optimization. The ESS power partitioning approach verifies its idea. The concise robust control problem from the combined constraint approach enables a short computation time, which is even shorter than the one of the non-robust control problem.

Along with cost robustness, this study has focused on the application of 2D ESS efficiency maps to the optimization. Despite its complex problem structure, an accurate ESS control schedule can be achieved by precisely calculating the SOC of the ESS. It also enables the controller to benefit from cost reduction by operating the ESS under higher efficiency regions only.

The proposed EMS structure can dynamically accommodate grid ancillary services as external working conditions. Two different types of additional power limitations have been proposed in this chapter: PC and DR. Proper penalty constants can change the main objective of the EMS from reducing the power trading cost to satisfying the external working conditions.

Comparison between robust optimal control schedules shows that the guarantee for the same worst case cost do not result in the same real cost. There can be multiple robust optimal control schedules that guarantee the same worst case cost under the

same net demand uncertainty. Applying each schedule to the real net demand condition may result in a different cost. Future study will focus on the development of an extended control approach that considers not only the worst case but also the best case of cost reduction.

3.8 Acknowledgments

© 2018 IEEE. Reprinted, with permission, from Jongwoo Choi, Youngmee Shin, Moonok Choi, Wan-Ki Park, and Il-Woo Lee, "Robust Control of a Microgrid Energy Storage System Using Various Approaches," in *IEEE Transactions on Smart Grid,* vol. 10, no. 3, pp. 2702-2712, May 2019, doi: 10.1109/TSG.2018.2808914.

In reference to IEEE copyrighted material which is used with permission in this thesis, the IEEE does not endorse any of Seoul National University's products or services. Internal or personal use of this material is permitted. If interested in reprinting/republishing IEEE copyrighted material for advertising or promotional purposes or for creating new collective works for resale or redistribution, please go to http://www.ieee.org/publications_standards/publications/rights/rights_link.html to learn how to obtain a License from RightsLink. If applicable, University Microfilms and/or ProQuest Library, or the Archives of Canada may supply single copies of the dissertation.

Chapter 4

Robust PV-BESS Scheduling for a Grid with Incentive for Forecast Accuracy

This chapter proposes a robust cost-optimal scheduling of a battery energy storage system (BESS) integrated with a solar photovoltaic power plant (PV). A power grid with an incentive policy is considered. Power transactions between the grid and its energy resources are normally charged according to the hourly time-of-use tariff. Additional hourly incentive is provided as a reversed version of an imbalance tariff; the owner of an energy resource can receive an incentive if the day-ahead grid-submitted schedule is maintained during the real-time operation. Accurate forecasting and robust scheduling are essential for PV-BESS owners to maximize both the transaction and incentive revenues. The PV power forecast model, which is based on a recurrent neural network, uses a convolutional neural network discriminator to decrease the gap between its open-loop one-step-ahead training and closed-loop multi-step-ahead test dynamics. The application of this generative adversarial network concept to the model training process ensures a stable day-ahead hourly forecast performance. The robust BESS scheduling model handles the remaining forecast error as a box uncertainty set to consider the cost-optimality and cost-robustness of the control schedule.

The scheduling model is formulated as a concise mixed-integer linear programming form to enable fast online optimization with the consideration for both transaction and incentive revenues. The introduction of adversarial learning to the forecast model increased the incentive revenue by 7.33%. Moreover, the online BESS scheduling with the incentive consideration enhanced the overall revenue by 3.73%.

4.1 Background

Solar photovoltaic power plants (PVs) passively convert solar irradiance into electrical power under the current weather condition. They are classified as uncontrollable variable renewable energy resources (VREs) if there are no control components such as inverters or battery energy storage systems (BESSs). Grid or electricity market operators should consider non-dispatchable and fluctuating characteristics of VREs to maintain power, voltage, and frequency balances of the electricity networks. Because this requires additional efforts of grid or market operators, some operators try to penalize [130, 131, 132, 133] or incentivize [134, 135] VREs by an imbalance tariff to indirectly control their deviations from predetermined or forecasted schedules.

This study presents economic scheduling of a VRE within a grid under an incentive policy. An integration of a PV and BESS is focused as a general form of a VRE as presented in Fig. 4.1. Power transactions between the grid and its VREs are normally charged according to the amounts of power supply and hourly unit prices. Additional incentives are provided to VREs if they maintain day-ahead submitted schedules. An energy management system (EMS) is required for a VRE to maximize both the transaction and incentive revenues. A PV power forecasting algorithm of the EMS helps to achieve a high incentive and provide a proper initial condition for op-

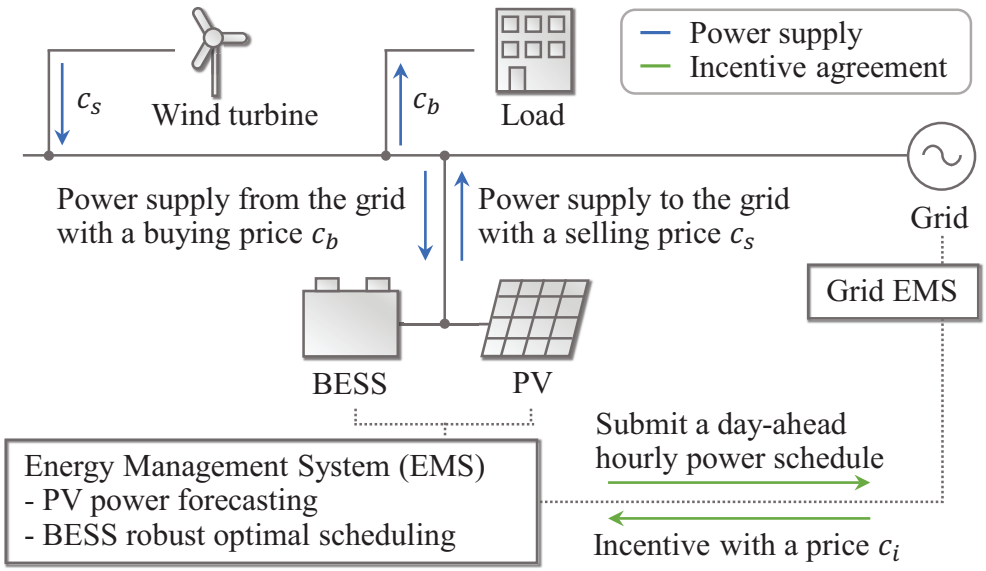

Figure 4.1: A schematic diagram of a grid under an incentive policy.

timal power scheduling. An optimal BESS scheduling algorithm helps to maximize the transaction revenue and adjust the power deviation from the forecasted schedule. The contribution of this study consists of advances in both algorithms.

PV power forecasting has been studied using physical or statistical data-driven models [136]. Autoregressive models including autoregressive integrated moving average (ARIMA) ones [76] have been generally used as a statistical data-driven model. Recent studies focus more on neural network models. Zhang *et al.* [88] compared the multilayer perceptron (MLP), convolutional neural network (CNN), and recurrent neural network (RNN) models for PV power forecasting. They concluded that the long short-term memory (LSTM) RNN model with the CNN-encoded sky image input outperforms the others. Lee *et al.* [79] and Gensler *et al.* [89] also proposed LSTM models with numerical weather prediction (NWP) data input. Both studies claimed that their models work better than conventional models such as persistent,

physical, autoregressive, and MLP models.

There have been various RNN-based models for PV power forecasting. Structural variations such as attention [80], CNN [137], and fuzzy-logic [138] have been applied to enhance the forecast accuracy. Some studies introduced prediction intervals [139] or probability outputs [140] to enhance the forecast reliability indirectly. In contrast to such approaches in modeling and test, this study presents a modification in the training process.

PV power forecast models generally focus on one-step-ahead forecasting on a given time domain [88, 80, 140]. A real-world application of a data-driven forecast model is operated in a rolling or moving horizon manner by updating the input data with the newest historical ones. Training a model is done in a same open-loop method; an RNN model with an autoregressive predictor is trained using the ground-truth input data to accurately forecast one-step-ahead values.

However, grid or market operators generally request multi-step-ahead forecasting such as day-ahead ones. The forecast model, which is trained using the ground-truth input data, has to use the step-wise generated data as its input because the ground-truth data of the future are unknown. The discrepancy between two data distributions produces inaccurate and unstable forecast results. This study introduces the generative adversarial network (GAN) to decrease this *exposure bias* [141] problem. The application of GAN as an RNN training framework robustly guarantees a similar level of accuracy for training and test results [86]. Several GAN variants are analyzed to further improve the robustness: deep convolutional GAN (DCGAN) [142], least squares GAN (LSGAN) [143], Wasserstein GAN (WGAN) [144], and WGAN with grid penalty (WGAN-GP) [145].

Despite the efforts to enhance the forecast accuracy, errors in forecast results are unavoidable. The cost optimal control of the BESS integrated with a PV suffers from uncertainties induced by forecast errors. Stochastic or worst-case control strategies can be considered to robustly solve an optimization problem with uncertainties [146]. The latter is applied in this study for a conservative estimation of the cash flow.

Optimal scheduling of a dispatchable energy resource is generally formulated using mixed-integer linear programming (MILP) for both robust and non-robust problems. Morais *et al.* [113] studied non-robust economic scheduling of a virtual power plant using MILP. Uncertainties in net demand have been additionally considered in robust microgrid studies. Zhang *et al.* [147] assumed a polyhedral uncertainty set for the worst-case cost optimal dispatch of a conventional generator within a microgrid, whereas Choi *et al.* [148] considered a box uncertainty set for the BESS scheduling problem. Malysz *et al.* [117] formulated a robust counterpart problem [127] using MILP to employ both box and polyhedral uncertainty sets.

This study introduces box uncertainty sets of different sizes to the BESS scheduling problem to deal with errors within a day-ahead PV power forecast schedule. The size of an uncertainty set represents the trade-off between the robustness and optimality. Weighted values of the forecasted PV power are tested as uncertainty bound candidates. Historic high and low power data are also tested as the simplest solution.

The robust scheduling model proposed in this study considers not only the power transaction revenue but also the incentive revenue as its cost-optimization objective. The deviation between the real and forecasted PV power is adjusted using the BESS operation to enhance the incentive revenue. Fast optimization speed of MILP enables this online, rolling-horizon update of a control schedule [117]. To further decrease

the computation time, a concise model form is developed by relaxing some integer constraints into affine ones.

In summary, this study presents the following contributions:

- Several GAN variants are applied to the PV power forecast model training. Training with a GAN discriminator ensures a stable day-ahead hourly forecast performance by decreasing the gap between open-loop training and closed-loop test dynamics of the RNN model.
- The robust BESS scheduling model focuses on the cost-optimization for both the power transaction and incentive revenues. Errors in the PV power forecast result are considered as a box uncertainty set during the robust optimization. The model is formulated as a concise MILP form to enable online optimization within a short computation time.

The rest of this chapter is organized as follows. The day-ahead hourly forecast model for a PV is proposed in Section 4.2. Robust cost-optimal scheduling of a BESS integrated with a PV is described in Section 4.3. The results and chapter summary are presented in Sections 4.4 and 4.5, respectively.

4.2 PV Power Forecast Model

4.2.1 Data Preprocessing

Historical power data of a 700-kW PV located in South Korea were collected from 2019 to 2020. Intermittent fluctuations within the real-time data were hourly averaged. An overview of the power and weather data are presented in Fig. 4.2.

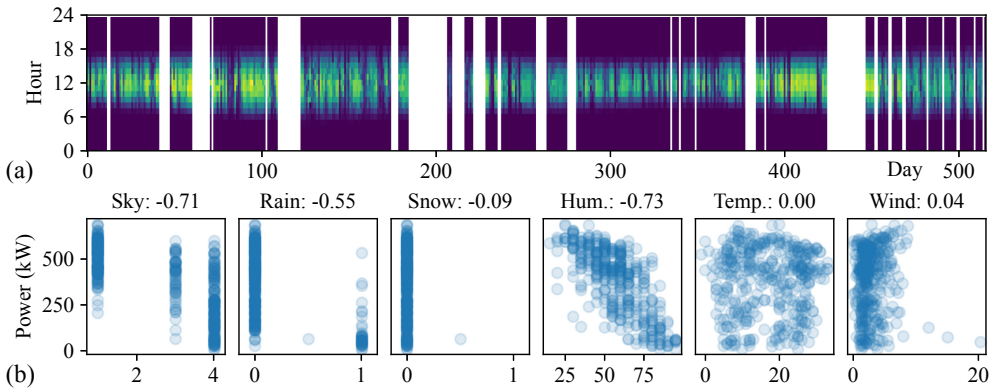

Figure 4.2: Overview of the training data. (a) Heatmap for the hourly power data. (b) Correlations between the power and weather data at daily noon.

Nowcasted and forecasted weather data were provided by the national NWP service of Korea. Five ordinal, categorical, and numerical parameters within the NWP data were selected as the predictor variables for the PV power forecast model: cloudiness, precipitation type (rain and snow), humidity, temperature, and wind speed. Solar irradiance is not used in this study because it is not provided by the NWP service. Instead, the cloudiness is used with its strong relationship with the power data as presented in Fig. 4.3. The difference between the real and NWP data may affect the accuracy of the PV power forecast model; this effect is tested in Section 4.4.5.

The fundamental operation of a PV cell is determined by the global horizontal (or tilted) irradiance and cell temperature with respect to its I-V curve. Hybrid physical-statistical models can be developed to further consider these parameters [93, 136]; however, they are beyond the scope of this study. This study focuses on the training process of a fully statistical forecast model and uses the given data themselves. It is inherently assumed that the historical power data reflect these parameters under the corresponding weather conditions.

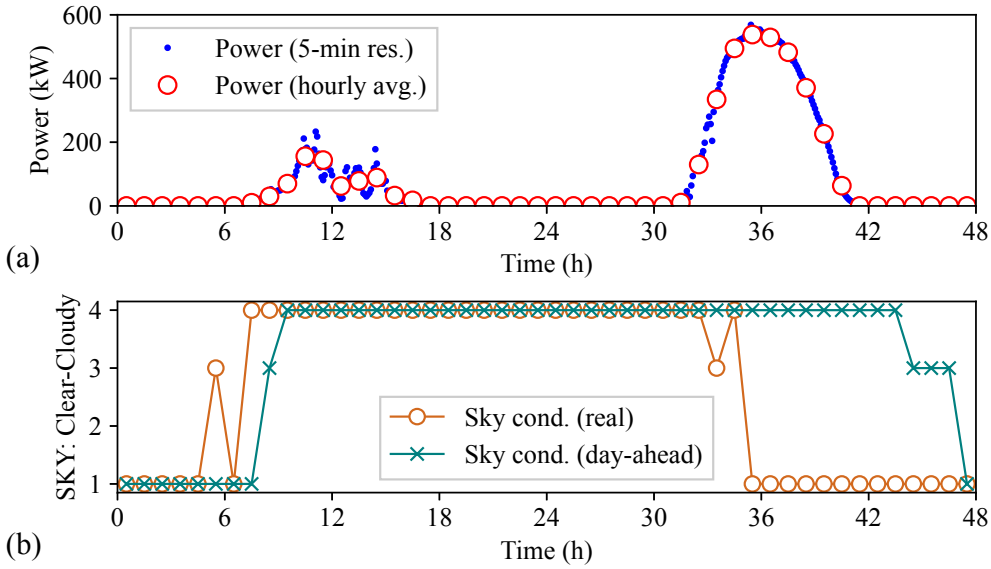

Figure 4.3: Two-day length sample data. (a) Power data and their hourly averages. (b) Comparison between the real (nowcasted) and day-ahead forecasted cloudiness.

Power and weather values that exceeded valid ranges were eliminated as anomalies. Constant values during a long time-interval were eliminated as well. Power x_p and weather x_w data of each time index t are normalized with mean μ and standard deviation σ at the end of the preprocessing stage:

$$x_p^t \leftarrow \left(x_p^t - \mu_p\right)/\sigma_p;\ x_w^t \leftarrow \left(x_w^t - \mu_w\right)/\sigma_w. \tag{4.1}$$

4.2.2 RNN-based Sequence Generator

This study proposes a PV power forecast model as an RNN-based sequence generator. An LSTM [82] cell in Fig. 4.4 stores autocorrelated information. The MLP layers connect the RNN and affine output layers. Layer normalization [85] and Dropout [149] are additionally applied for regularization.

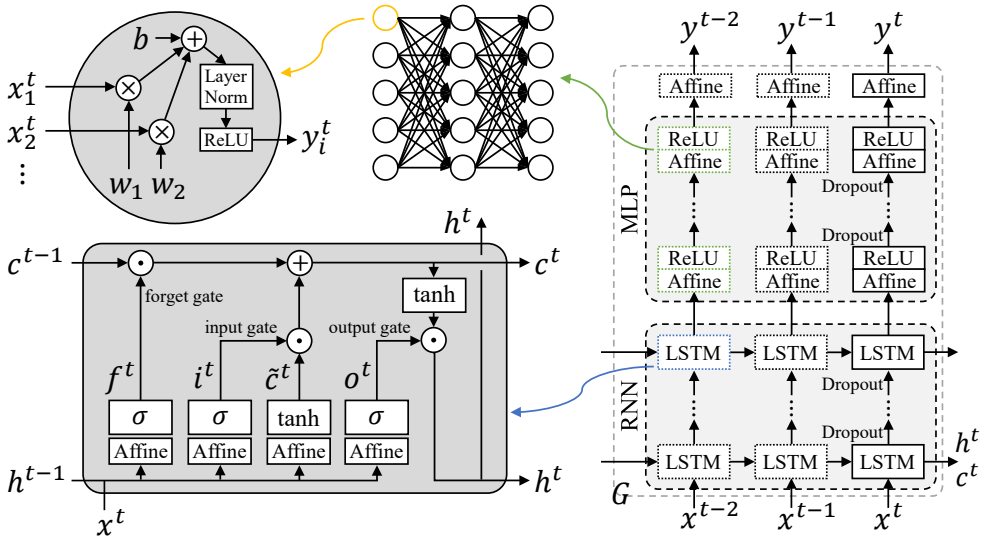

Figure 4.4: Network structure of the RNN-based sequence generator.

An autoregressive forecast model, including the proposed generator network G of Fig. 4.4 and 4.5, is generally trained in an open-loop teacher forcing mode; model parameters are optimized so that the inferred output y^{t-1} from the ground-truth input data x^{t-1} matches with the ground-truth value x^t as the forecasted value $\tilde{x}^t$. This method resembles the operation of an hour-ahead forecast model, and is therefore suitable for it.

Open-loop hour-ahead forecasting of a basic sequence generator model can be represented as

$$[\tilde{x}_p^t, \tilde{x}_w^t] = G\left([x_p^{t-1}, x_w^{t-1}], c^{t-1}, h^{t-1}\right) \tag{4.2}$$

$$= G\left([x_p^{t-1}, x_w^{t-1}], [x_p^{t-2}, x_w^{t-2}], c^{t-2}, h^{t-2}\right) \tag{4.3}$$

$$= G\left(x_p^{t-1}, x_p^{t-2}, ..., x_w^{t-1}, x_w^{t-2}, ...\right). \tag{4.4}$$

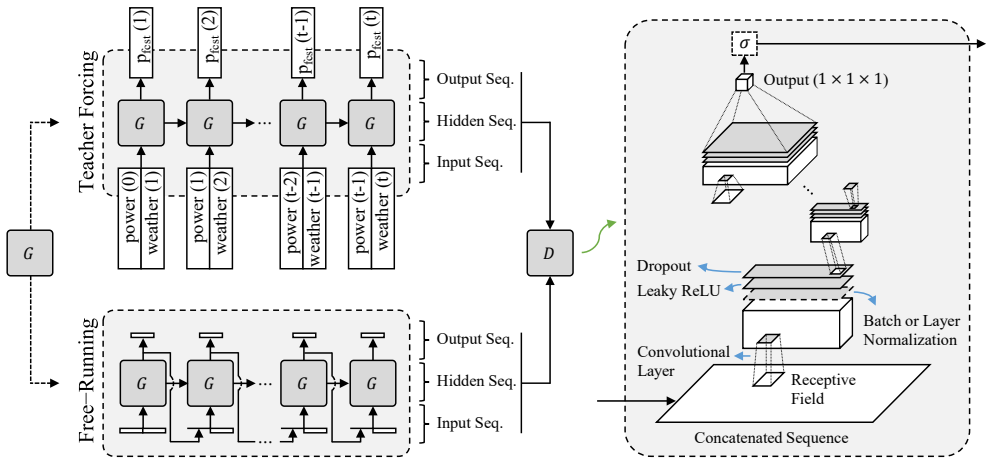

Figure 4.5: Adversarial training process of the RNN-based sequence generator network with the CNN-based sequence discriminator.

Starting from this basic model, $\tilde{x}_w^t$ in the left-hand side is removed because the forecast model does not target weather forecasting. Moreover, $\tilde{x}_w^t$ is used as a model input because it is provided by the national NWP service as a forecasted value. The symbol tilde is removed as x_w^t to represent that it is not an output of the forecast model. The effect of x_w^t accuracy on the forecast performance is tested in Section 4.4.5. The modified model is now represented as

$$\tilde{x}_p^t = G\left(x_p^{t-1}, x_p^{t-2}, ..., x_w^t, x_w^{t-1}, x_w^{t-2}, ...\right) \tag{4.5}$$

$$= G\left(x_w^t, [x_p^{t-1}, x_w^{t-1}], [x_p^{t-2}, x_w^{t-2}], ..., [x_p^0, x_w^0]\right) \tag{4.6}$$

$$= G\left([x_p^{t-1}, x_w^t], [x_p^{t-2}, x_w^{t-1}], ..., [x_p^1, x_w^0], x_p^0\right) \tag{4.7}$$

$$\approx G\left([x_p^{t-1}, x_w^t], [x_p^{t-2}, x_w^{t-1}], ..., [x_p^1, x_w^0]\right). \tag{4.8}$$

There are two approaches to handle x_w^t as a model input. The model (4.6) uses it as an additional input, e.g., the second input for an MLP layer. The model (4.8) just

delays the power data to prevent this doubled weather data input. The oldest power value is dropped with the assumption for its small correlation. The model proposed in Fig. 4.4 and 4.5 takes the latter approach without comparing their performances.

4.2.3 CNN-based Sequence Discriminator

General open-loop training method for an hour-ahead forecast model is introduced in Section 4.2.2. However, a day-ahead hourly forecast model has to be operated under a closed-loop free-running mode; the model recursively uses the forecasted value as its input. Discrepancy between the training and test dynamics may result in unexpected behaviors. For example, a persistent model $\tilde{x}^t = x_{t-1}$, which belongs to the first-order autoregressive model, can provide an acceptable open-loop forecast performance if the time difference between x^t and x^{t-1} is small. By contrast, the closed-loop operation of this model only results in a fixed initial value $\tilde{x}^t = x^0$. Complicated models can also present unexpected behaviors when the model encounters an unexposed erroneous power value during the inference. Moreover, open-loop-optimized model parameters can comprise a feedback loop that amplifies the forecast error or disturbs the forecasted value by saturation or oscillation. A closed-loop training method cannot be a solution because of the poor [150] or inconsistent [151] performance of the trained model.

A GAN-based training framework [86] is employed in this study to guarantee the stable performance of the trained model. The generator is trained in such a way that the discriminator fails to distinguish its training and testing dynamics.

The adversarial training process of the generator G and discriminator D is presented in Fig. 4.5. The forecast model G with the parameter θ_g outputs a power

forecast data sequence $\tilde{x}_p$ in both the teacher forcing and free-running modes:

$$\tilde{x}_{p,TF}^{t} = G\left([x_p^{t-1}, x_w^t]; \theta_g\right) \tag{4.9}$$

$$\tilde{x}_{p,FR}^{t} = G\left([\tilde{x}_{p,FR}^{t-1}, x_w^t]; \theta_g\right) \tag{4.10}$$

$$\tilde{x}_{p,either}^{1} = G\left([x_p^0, x_w^1]; \theta_g\right). \tag{4.11}$$

Selected input, hidden, or output sequences from the generator operation are concatenated as the behavior sequence B. A CNN-based discriminator D tries to identify whether the sequence comes from teacher forcing or free-running mode. It consists of convolutional, batch or layer normalization, and leaky ReLU layers, following the DCGAN guideline [142].

4.2.4 Training Objectives

The discriminator of a GAN is first trained n_d times with its objective L_d for each epoch. The generator is next trained with $L_g + \alpha L$, where L is its original objective as a forecast model, L_g is the GAN objective, and α is the weight. A robust regression error metric is applied for L to decrease the effect of possible outliers within the ground-truth data. Huber [152] and log-cosh losses are applicable for this purpose; the latter is applied to this study because it does not require additional parameters:

$$L = \sum_{t=T_{init}}^{T_{final}} \frac{\log\cosh\left(x_p^t - \tilde{x}_{p,TF}^{t}\left(\theta_g\right)\right)}{\left(T_{final} - T_{init} + 1\right)}. \tag{4.12}$$

The discriminator tries to classify behavior sequences from teacher forcing B_{TF} and free-running B_{FR} modes as 1 and 0, respectively. Therefore, the standard GAN

objective of the discriminator D with the parameter θ_d is

$$L_d(\theta_d) = -\log\left[D\left(B_{TF}\left(\theta_g\right);\theta_d\right)\right] - \log\left[1 - D\left(B_{FR}\left(\theta_g\right);\theta_d\right)\right]. \tag{4.13}$$

In contrast, the generator tries to fool the discriminator by maximizing (4.13). It is converted into minimizing

$$L_g(\theta_g) = -\log\left[1 - D\left(B_{TF}\left(\theta_g\right);\theta_d\right)\right] - \log\left[D\left(B_{FR}\left(\theta_g\right);\theta_d\right)\right]. \tag{4.14}$$

The second term of (4.14) makes the generator maintain its free-running behavior similar to the teacher forcing one. The first term, which ensures the opposite, can be neglected if needed.

Three variants of the GAN are additionally tested in this study to further improve the robustness. LSGAN [143], which aims to maintain a stable gradient during training, is applied by removing the sigmoid discriminator output and replacing the cross-entropy loss with the quadratic one:

$$L_d(\theta_d) = \left[D\left(B_{TF}\left(\theta_g\right);\theta_d\right) - 1\right]^2/2 + \left[D\left(B_{FR}\left(\theta_g\right);\theta_d\right) - 0\right]^2/2 \tag{4.15}$$

$$L_g(\theta_g) = \left[D\left(B_{TF}\left(\theta_g\right);\theta_d\right) - 0\right]^2/2 + \left[D\left(B_{FR}\left(\theta_g\right);\theta_d\right) - 1\right]^2/2. \tag{4.16}$$

WGAN [144] also removes the sigmoid output and cross-entropy loss. Weights of the discriminator are clamped with a box constraint $[-c,\, c]$, which is normally $[-0.01,\, 0.01]$, to ensure the K-Lipschitz duality condition:

$$L_d(\theta_d) = -D\left(B_{TF}\left(\theta_g\right);\theta_d\right) + D\left(B_{FR}\left(\theta_g\right);\theta_d\right) \tag{4.17}$$

$$L_g\left(\theta_g\right) = +D\left(B_{TF}\left(\theta_g\right);\theta_d\right) - D\left(B_{FR}\left(\theta_g\right);\theta_d\right) \tag{4.18}$$

$$\theta_g \leftarrow \text{clip}\left(\theta_g, -c, c\right). \tag{4.19}$$

Although WGAN remedies the vanishing gradient problem, its performance depends on a value of the clipping parameter c. WGAN-GP [145] alternatively enforces the 1-Lipschitz condition by introducing a penalty on the gradient norm that varies from 1:

$$\acute{B}\left(\theta_g\right) = \epsilon B_{TF}\left(\theta_g\right) + \left(1-\epsilon\right) B_{FR}\left(\theta_g\right) \tag{4.20}$$

$$\begin{aligned} L_d\left(\theta_d\right) = &- D\left(B_{TF}\left(\theta_g\right);\theta_d\right) + D\left(B_{FR}\left(\theta_g\right);\theta_d\right) \\ &+ \lambda\left[\left\|\nabla_{\hat{B}} D\left(\acute{B}\left(\theta_g\right);\theta_d\right)\right\|_2 - 1\right]^2 \end{aligned} \tag{4.21}$$

$$L_g\left(\theta_g\right) = +D\left(B_{TF}\left(\theta_g\right);\theta_d\right) - D\left(B_{FR}\left(\theta_g\right);\theta_d\right) \tag{4.22}$$

where λ is the penalty weight with its usual value 10 and ϵ is the random variable from the uniform distribution $U[0,1]$.

4.2.5 Training and Validation

Additive input noise, which has presented enhanced [153] or reduced [154] accuracy for RNN model training, is tested as a data augmentation method for the power data. It also works as an adversarial example [155] by providing unrealistic non-zero power values for night times. Gaussian noise $\xi \sim N(0, A\sigma_p)$ with the amplitude parameter $A \in \{0, 0.005, 0.01\}$ is added to the power value of each training time step:

$$\tilde{x}^t_{p,TF} = G\left(\left[x^{t-1}_p + \xi, x^t_w\right];\theta_g\right). \tag{4.23}$$

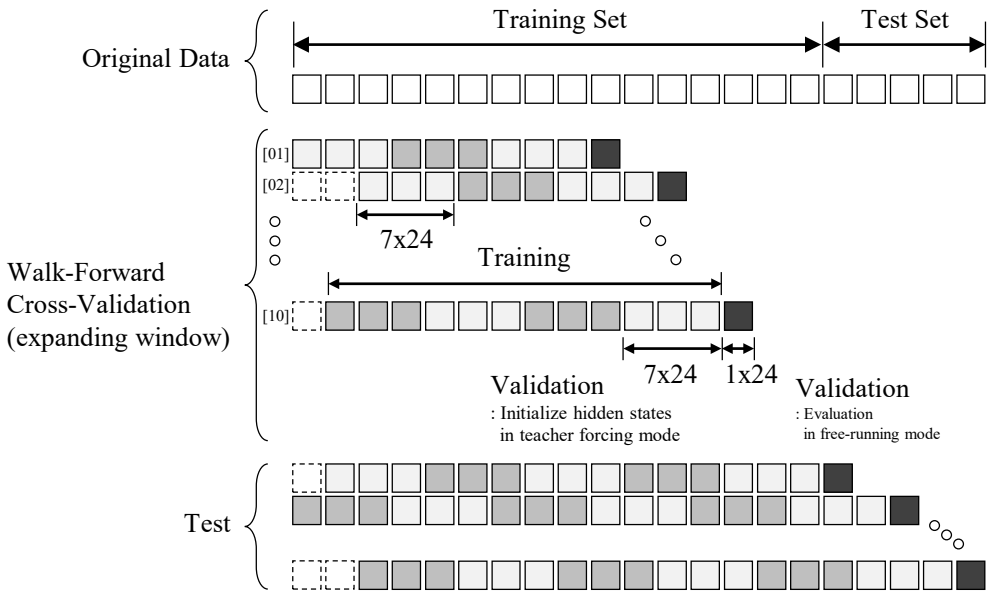

Figure 4.6: Walk-forward cross-validation with an expanding window.

Walk-forward cross-validation illustrated in Fig. 4.6 is applied for the hyperparameter optimization. Training data of 386×24-hour length are divided into 7×24-hour length ones to avoid the vanishing gradient problem. Temporal discontinuities less than three days are neglected. Splitting is done without an overlap to avoid overfitting due to duplicated data.

Each model is trained under candidate hyperparameter values for validation. Day-ahead forecast performance of the trained model is evaluated for ten different days. Optimized hyperparameter values for each model are listed in Table 4.1.

Table 4.1: Hyperparameter Optimization

GAN Parameter		RNN	DC	LS	W	W-GP
G	RNN	Hidden 49, Depth 2, Dropout 0.2				
	MLP	Hidden 52, Depth 1, Dropout 0.5				
D	CNN	Kernel 3x3, Depth 5, Dropout 0.2				
Training		Batch size 5, Epoch 300, Adam optimizer				
Learning Rate		1e-3	1e-3	1e-3	1e-3	2e-4
Momentum		0.9	0.5	0.5	0.5	0.5
GAN	L_g Terms	–	Both	2nd only	Both	Both
	(n_d, α)	–	(1, 10)	(1, 10)	(1, 1)	(1, 30)

4.3 Robust BESS Scheduling

4.3.1 Power Transaction Revenue

A grid that supplies power with the hourly buying price c_b^t and purchases with a lower selling price c_s^t is suggested. A standalone PV simply pays a negative hourly settlement $-c_s^t x_p^t$ to the grid. In case of a PV with a BESS, the net power supply x_{net} from the grid must be considered:

$$x_{net}^t = -x_p^t - x_{dis}^t + x_{chg}^t \tag{4.24}$$

where x_{chg} and x_{dis} are the BESS charge and discharge powers, respectively. The non-robust BESS scheduling problem to minimize the additional payment to the grid is formulated as an MILP expression using the forecasted PV power $\tilde{x}_p^t$:

$$\min \ \sum_{t=T_{init}}^{T_{final}} r^t \tag{4.25}$$

$$s.t. \ r^t = \left(c_b^t x_{net,+}^t + c_s^t x_{net,-}^t\right) - \left(-c_s^t \tilde{x}_p^t\right) \tag{4.26}$$

$$x^t_{net,+} + x^t_{net,-} = -\tilde{x}^t_p - x^t_{dis} + x^t_{chg} \tag{4.27}$$

$$0 \leq x^t_{net,+} \leq P_{BESS}\delta^t_{net} \tag{4.28}$$

$$-\left(P_{PV} + P_{BESS}\right)\left(1 - \delta^t_{net}\right) \leq x^t_{net,-} \leq 0 \tag{4.29}$$

where r^t is the additional payment during the scheduling time range T_{init} and T_{final}. The binary value δ^t_{net} indicates the sign of x^t_{net} with $x^t_{net,+}$ and $x^t_{net,-}$. P_{PV} and P_{BESS} are the power capacities of the PV and BESS, respectively. The degradation of an energy resource is neglected.

BESS constraints for x^t_{chg} and x^t_{dis} are also applied as

$$0 \leq x^t_{chg} \leq P_{BESS}\delta^t_{BESS} \tag{4.30}$$

$$0 \leq x^t_{dis} \leq P_{BESS}\left(1 - \delta^t_{BESS}\right) \tag{4.31}$$

$$E_{init} - \sum\nolimits_{k=T_{init}}^{t}\left(x^k_{dis}/\eta - x^k_{chg}\eta\right) \geq S_{min}E_{BESS} \tag{4.32}$$

$$E_{init} - \sum\nolimits_{k=T_{init}}^{t}\left(x^k_{dis}/\eta - x^k_{chg}\eta\right) \leq S_{max}E_{BESS} \tag{4.33}$$

$$E_{init} - \sum\nolimits_{k=T_{init}}^{T_{final}}\left(x^k_{dis}/\eta - x^k_{chg}\eta\right) = E_{final} \tag{4.34}$$

where δ^t_{BESS} is the charge/discharge flag, E_{BESS} is the BESS energy capacity, and η is the efficiency. E_{init} and E_{final} are the initial and final energy storage conditions, respectively. S_{min} and S_{max} represent the state of charge (SOC) limitation with their values between zero and one.

The deterministic problem of (4.25)–(4.29) is transformed into a nondeterministic one if the forecast error is considered. A box uncertainty set $\left[x^t_{p,min}, x^t_{p,max}\right]$ is applied as the error range for the real PV power $x^t_p = \tilde{x}^t_p + \zeta\Delta x^t_p$ with the maximum

deviation Δx_p^t and uncertainty $\zeta^t \sim U\left[-1,1\right]$:

$$\min \quad \sum_{t=T_{init}}^{T_{final}} r^t \tag{4.35}$$

$$s.t. \quad r^t = \left(c_b^t x_{net,+}^t + c_s^t x_{net,-}^t\right) - \left\{-c_s^t \left(\tilde{x}_p^t + \zeta \Delta x_p^t\right)\right\} \tag{4.36}$$

$$x_{net,+}^t + x_{net,-}^t = -\left(\tilde{x}_p^t + \zeta \Delta x_p^t\right) - x_{dis}^t + x_{chg}^t \tag{4.37}$$

$$0 \leq x_{net,+}^t \leq P_{BESS} \delta_{net}^t \tag{4.38}$$

$$-\left(P_{PV} + P_{BESS}\right)\left(1 - \delta_{net}^t\right) \leq x_{net,-}^t \leq 0. \tag{4.39}$$

The worst-case cost-optimization version of this nondeterministic problem can be intuitively derived as follows:

$$\min \quad \sum_{t=T_{init}}^{T_{final}} r^t \tag{4.40}$$

$$s.t. \quad r^t \geq \left(c_b^t x_{net1,+}^t + c_s^t x_{net1,-}^t\right) - \left(-c_s^t x_{p,max}^t\right) \tag{4.41}$$

$$r^t \geq \left(c_b^t x_{net2,+}^t + c_s^t x_{net2,-}^t\right) - \left(-c_s^t x_{p,min}^t\right) \tag{4.42}$$

$$x_{net1,+}^t + x_{net1,-}^t = -x_{p,max}^t - x_{dis}^t + x_{chg}^t \tag{4.43}$$

$$x_{net2,+}^t + x_{net2,-}^t = -x_{p,min}^t - x_{dis}^t + x_{chg}^t \tag{4.44}$$

$$0 \leq x_{net1,+}^t \leq P_{BESS} \delta_{net1}^t \tag{4.45}$$

$$0 \leq x_{net2,+}^t \leq P_{BESS} \delta_{net2}^t \tag{4.46}$$

$$-\left(P_{PV} + P_{BESS}\right)\left(1 - \delta_{net1}^t\right) \leq x_{net1,-}^t \leq 0 \tag{4.47}$$

$$-\left(P_{PV} + P_{BESS}\right)\left(1 - \delta_{net2}^t\right) \leq x_{net2,-}^t \leq 0 \tag{4.48}$$

The selection of a proper Δx_p^t value for this optimization problem affects the trade-off between the cost-optimality and cost-robustness of the resulting control schedule.

This robust optimization problem has been reformulated as various MILP forms to reduce the computation time [148, 117]. However, it is possible to derive a simple LP form from (4.35)–(4.39). It starts from splitting the cases with respect to the integer value of δ^t_{net}. If $\delta^t_{net} = 1$, $x^t_{net,-} = 0$ and

$$r^t = \left(c^t_b x^t_{net,+} + c^t_s x^t_{net,-}\right) - \left(-c^t_s x^t_p\right) \tag{4.49}$$

$$= \left(c^t_b x^t_{net,+} + 0\right) - \left(-c^t_s x^t_p\right) \tag{4.50}$$

$$= \left(c^t_b x^t_{net,+} + c^t_b x^t_{net,-}\right) - \left(-c^t_s x^t_p\right) \tag{4.51}$$

$$= c^t_b \left(-x^t_p - x^t_{dis} + x^t_{chg}\right) + c^t_s x^t_p. \tag{4.52}$$

Same steps can be applied to the remaining case for $\delta^t_{net} = 0$. The resulting nondeterministic problem becomes

$$\min \quad \sum\nolimits_{t=T_{init}}^{T_{final}} r^t \tag{4.53}$$

$$s.t. \quad r^t \geq c^t_b \left(-x^t_p - x^t_{dis} + x^t_{chg}\right) + c^t_s x^t_p - M\left(1 - \delta^t_{net}\right) \tag{4.54}$$

$$r^t \geq c^t_s \left(-x^t_p - x^t_{dis} + x^t_{chg}\right) + c^t_s x^t_p - M\delta^t_{net} \tag{4.55}$$

$$-x^t_p - x^t_{dis} + x^t_{chg} \leq P_{BESS}\delta^t_{net} \tag{4.56}$$

$$-x^t_p - x^t_{dis} + x^t_{chg} \geq -\left(P_{PV} + P_{BESS}\right)\left(1 - \delta^t_{net}\right) \tag{4.57}$$

where M is a large enough number. Considering the sign of x^t_{net} and following value of δ^t_{net}, it is possible to conclude that δ^t_{net} terms are redundant; the initial assumption $c^t_b \geq c^t_s$ activates only the correct condition between (4.54) and (4.55):

$$\min \quad \sum\nolimits_{t=T_{init}}^{T_{final}} r^t \tag{4.58}$$

$$s.t. \quad r^t \geq c_b^t \left(-x_p^t - x_{dis}^t + x_{chg}^t\right) - c_s^t \left(-x_p^t\right) \tag{4.59}$$

$$r^t \geq c_s^t \left(-x_p^t - x_{dis}^t + x_{chg}^t\right) - c_s^t \left(-x_p^t\right). \tag{4.60}$$

The worst-case optimal version of this LP form is derived by applying the uncertainty range for x_p^t:

$$\min \quad \sum\nolimits_{t=T_{init}}^{T_{final}} r^t \tag{4.61}$$

$$s.t. \quad r^t \geq -c_b^t x_{dis}^t + c_b^t x_{chg}^t - \left(c_b^t - c_s^t\right) x_{p,min}^t \tag{4.62}$$

$$r^t \geq -c_s^t x_{dis}^t + c_s^t x_{chg}^t. \tag{4.63}$$

The robust BESS scheduling problem of (4.30)–(4.34) and (4.61)–(4.63) reveals a simple intuition. A PV without the BESS operation initially sells its power to the grid. The BESS charge power that is definitely lower than the PV power maintains the negative sign of x_{net}^t and only decreases the selling revenue as (4.63). By contrast, the charge power that may be higher than the PV power possibly changes the selling behavior into the buying one as (4.62). Only the lower boundary value $x_{p,min}^t$ of the PV power forecast uncertainty is required for this worst-case optimization problem.

4.3.2 Forecast Accuracy Incentive

VREs can disturb the stability of an electricity network with their variable power generation. Incentives or penalties for the VRE operators have been proposed by some network operators to encourage them to submit forecasted generation schedules, thereby decreasing uncertainties in the network management.

The forecast accuracy incentive in Korea [135] is applied to this study as a re-

versed version of an energy imbalance tariff [130]. A VRE operator can get an hourly incentive with the price c_i depending on the absolute error (AE) of the day-ahead forecasted schedule submitted at yesterday 10 or 17 h. Following general conditions are required:

- The normalized absolute error (NAE), the AE normalized by the VRE power capacity, has to be less than 8%.
- The capacity utilization rate, the power normalized by the capacity, has to be higher than 10%.
- The normalized mean absolute error (NMAE) for the hours that meet both conditions should be less than 10% for each month.
- If a VRE consists of multiple energy resources (e.g., PVs and BESSs), the operator can submit a net power generation schedule. However, the normalization is done by an aggregate capacity of only the non-dispatchable resources to prevent the distortion on the incentive policy.

A BESS integrated with a PV is day-ahead scheduled to maximize the power transaction revenue. At the time of its operation, the BESS can decide to deviate from the original schedule if the PV power forecast error significantly decreases the incentive revenue. The BESS is first rescheduled for the current time step to adjust the net power generation to be closer to the submitted schedule. It is then rescheduled for the remaining hours. Fast optimization using the simple LP form of (4.61)–(4.63) is helpful for this online control.

During the online optimization, the real PV power x_p^t is known for the current

time. Therefore, robust optimization using the uncertainty set is not required for T_{init}:

$$\min \sum_{t=T_{init}}^{T_{final}} \left(r^t - i^t\right) \tag{4.64}$$

$$s.t.\ r^t \geq \begin{cases} -c_b^t x_{dis}^t + c_b^t x_{chg}^t - \left(c_b^t - c_s^t\right) x_p^t & \text{if } t = T_{init} \\ -c_b^t x_{dis}^t + c_b^t x_{chg}^t - \left(c_b^t - c_s^t\right) x_{p,min}^t & \text{otherwise} \end{cases} \tag{4.65}$$

$$r^t \geq -c_s^t x_{dis}^t + c_s^t x_{chg}^t \tag{4.66}$$

where i^t is the incentive revenue. Nondeterministic constraints for i^t are derived according to the incentive policy:

$$-\hat{x}_{net}^t = \hat{x}_p^t + \hat{x}_{dis}^t - \hat{x}_{chg}^t \tag{4.67}$$

$$\varepsilon_{max}^t = \left(0.92 P_{PV} + 2 P_{BESS}\right)\left(1 - \delta_\varepsilon^t\right) + 0.08 P_{PV} \tag{4.68}$$

$$\varepsilon_{max}^t \geq \left(x_p^t + x_{dis}^t - x_{chg}^t\right) - \left(-\hat{x}_{net}^t\right) \tag{4.69}$$

$$\varepsilon_{max}^t \geq -\left(x_p^t + x_{dis}^t - x_{chg}^t\right) + \left(-\hat{x}_{net}^t\right) \tag{4.70}$$

$$x_p^t \geq 0.1 P_{PV} \delta_p^t \tag{4.71}$$

$$i^t \leq c_i x_p^t \delta_\varepsilon^t \tag{4.72}$$

$$i^t \leq c_i x_p^t \delta_p^t \tag{4.73}$$

where $-\hat{x}_{net}^t$ is the net power generation schedule that was day-ahead submitted to the grid. Its fixed value consists of the day-ahead forecasted PV power $\hat{x}_p^t$ and the day-ahead scheduled BESS power $\hat{x}_{chg}^t$ and $\hat{x}_{dis}^t$.

The theoretical maximum error between the submitted and real generation schedule is $|(P_{PV} + P_{BESS}) - (-P_{BESS})|$ when $(x_p^t, x_{dis}^t, x_{chg}^t) = (P_{PV}, P_{BESS}, 0)$ and

$(\hat{x}_p^t, \hat{x}_{dis}^t, \hat{x}_{chg}^t) = (0, 0, P_{BESS})$, or vice versa. By contrast, the incentive policy defines $0.08P_{PV}$ as the error threshold. ε_{max}^t of (4.68)–(4.70) represents these error restrictions with respect to the binary value of δ_ε^t. The binary value of δ_p^t in (4.71) indicates the remaining power restriction $0.1P_{PV}$. Monthly NMAE restriction is neglected in this problem.

The robust counterpart of (4.69)–(4.73) for the deterministic optimization problem is derived as follows:

$$\varepsilon_{max}^t \geq \begin{cases} \left(x_p^t + x_{dis}^t - x_{chg}^t\right) - \left(-\hat{x}_{net}^t\right) & \text{if } t = T_{init} \\ \left(x_{p,max}^t + x_{dis}^t - x_{chg}^t\right) - \left(-\hat{x}_{net}^t\right) & \text{otherwise} \end{cases} \tag{4.74}$$

$$\varepsilon_{max}^t \geq \begin{cases} -\left(x_p^t + x_{dis}^t - x_{chg}^t\right) + \left(-\hat{x}_{net}^t\right) & \text{if } t = T_{init} \\ -\left(x_{p,min}^t + x_{dis}^t - x_{chg}^t\right) + \left(-\hat{x}_{net}^t\right) & \text{otherwise} \end{cases} \tag{4.75}$$

$$x_{p,min}^t \geq 0.1P_{PV}\delta_p^t \tag{4.76}$$

$$i^t \leq c_i x_{p,min}^t \delta_\varepsilon^t \tag{4.77}$$

$$i^t \leq c_i x_{p,min}^t \delta_p^t. \tag{4.78}$$

The robust optimal control problem of (4.30)–(4.34), (4.64)–(4.68), and (4.74)–(4.78) tries to maximize both the power transaction and incentive revenues. The online optimization flow for the proposed problem is presented in Algorithm 1. The control schedule is continuously updated for the receding time range $[T_{init}, T_{final}]$. T_{final} is fixed as midnight because the transaction price c_b and c_s in Korea are updated on a daily basis.

The online optimization flow of Algorithm 1 can also be applied to sub-hourly

Algorithm 1: Online Optimization

Preprocess historical PV data x_p^t and NWP data x_w^t
$T_{init} \leftarrow 1$ and $T_{final} \leftarrow 24$
Day-ahead forecast of x_p^t as $\tilde{x}_p^t$
Define $\left[x_{p,min}^t, x_{p,max}^t\right]$ with the consideration about $\tilde{x}_p^t$
Solve (4.30)–(4.34) and (4.61)–(4.63) for x_{chg}^t and x_{dis}^t
$\hat{x}_p^t \leftarrow \tilde{x}_p^t$, $\hat{x}_{chg}^t \leftarrow x_{chg}^t$, and $\hat{x}_{dis}^t \leftarrow x_{dis}^t$
for $T_{init} = 1, 2, \ldots, T_{final}$ **do**
    $x_p^{T_{init}}$ becomes a known value
    Update x_{chg}^t and x_{dis}^t
        by solving (4.30)–(4.34), (4.64)–(4.68), and (4.74)–(4.78)
    $E_{init} \leftarrow E_{init} - x_{dis}^{T_{init}}/\eta + x_{chg}^{T_{init}}\eta$
end

scheduling in a minute or second basis. Receding horizon control can be considered by defining T_{final} as a fixed offset from T_{init}. The concise problem structure enables to solve the problem for 3×60 time steps within 300 ms, thereby enabling an online adjustment for the net power generation. Detailed analysis for the computation time is presented in Section 4.4.7.

4.4 Results

4.4.1 Benchmark Models for PV Power Forecasting

The proposed RNN models are developed using PyTorch [156]. Several benchmark models are further introduced in this study to compare the day-ahead hourly forecast performance.

- Persistent model, $\tilde{x}_p^t = x_p^{t-24}$, is used as a naive baseline.
- Exponential moving average (EMA) is applied in an hourly manner, according

to $\tilde{x}_p^t = 0.9x_p^{t-24} + 0.1\tilde{x}_p^{t-24} = 0.9x_p^{t-24} + 0.1(0.9x_p^{t-48} + 0.1\tilde{x}_p^{t-48}) = \cdots$.

- Two seasonal ARIMA models are tested on behalf of statistical methods: ARIMA$(1,0,0)(1,1,0)_{24}$ from [76] and $(0,1,0)(0,1,1)_{24}$ from the autocorrelation analysis.

- Scheduled sampling (SS) [150], which selects the training input between the ground-truth and predicted values for each step, is tested for the RNN model with the ground-truth selection probability of $26/(25 + \exp(t/25))$.

4.4.2 Stability of the PV Power Forecast Results

The enhanced stability of an RNN model is analyzed by repeatedly evaluating the day-ahead hourly forecast accuracy. Each model is independently trained and validated five time for each of the ten validation dates. The basic RNN model is trained in a general open-loop mode with its optimal hyperparameters; others are trained with the consideration for the close-loop forecast performance.

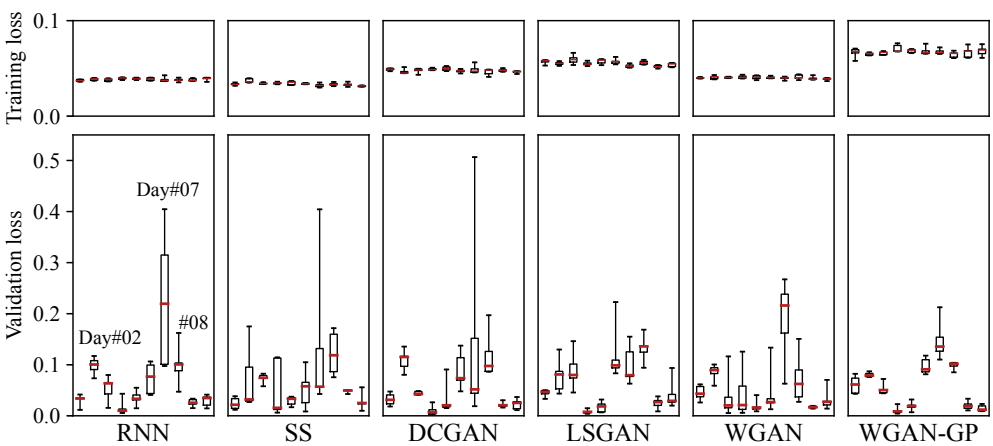

Figure 4.7: Repeated stability test of RNN models for each validation date.

Table 4.2: Stability Test for RNN Models

Stability ($\times 10^{-2}$)	RNN	SS	DC	LS	W	W-GP
Avg(Q4-Q0)	7.49	9.36	9.19	6.48	8.49	**3.16**
Avg(Q3-Q1)	3.64	3.94	2.62	1.86	2.48	**1.24**
Avg(Q2)	6.98	**4.85**	4.86	6.04	5.40	5.78
Avg(Q4-Q0) wo the 7th	4.91	6.38	4.79	6.18	7.16	**2.38**
Avg(Q3-Q1) wo the 7th	1.66	3.54	1.72	1.54	1.91	**1.07**
Avg(Q2) wo the 7th	5.32	4.75	4.82	5.83	**3.60**	4.91

Fig. 4.7 presents the result as a box plot with whiskers from the minimum to the maximum. In contrast to the stable and small training loss, the validation loss varied significantly for some models. An averaged value of the validation loss deviation is listed in Table 4.2 as a stability measure. Training the forecast model under the WGAN-GP framework reported the most stable result.

It should be noted that every model presented a stability problem for the seventh day, when the wind was uncommonly strong on a sunny day. Lack of similar data within the training set made the trained model produce an unstable result. And this instability might have diverged during the closed-loop inference for day-ahead forecasting. WGAN-GP helped to restrict this instability.

The effect of the additive input noise as an adversarial example is also analyzed as Fig. 4.8. DCGAN, LSGAN, and WGAN produced significantly improved results with the noise amplitude 0.005. SS showed enhanced stability but slightly increased median loss. WGAN-GP performed worse with the noise. Additive noise with amplitude 0.005 was applied to every model except WGAN-GP for the following analyses.

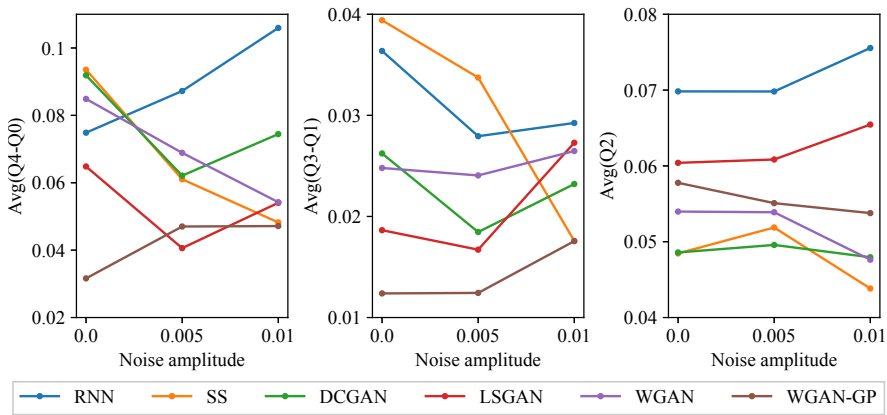

Figure 4.8: Effect of additive noise on validation loss.

4.4.3 Accuracy of the PV Power Forecast Results

The day-ahead forecast accuracy for the test dates with the nowcasted weather data is evaluated by the mean absolute error (MAE) and root mean square error (RMSE). Errors are normalized (N-) with the PV capacity [90] to produce a percentage-like value. The result is presented in Table 4.3. Every RNN-based model outperformed the benchmark models. DCGAN and WGAN-GP performed the best. Forecast results for selected days are presented in Fig. 4.9.

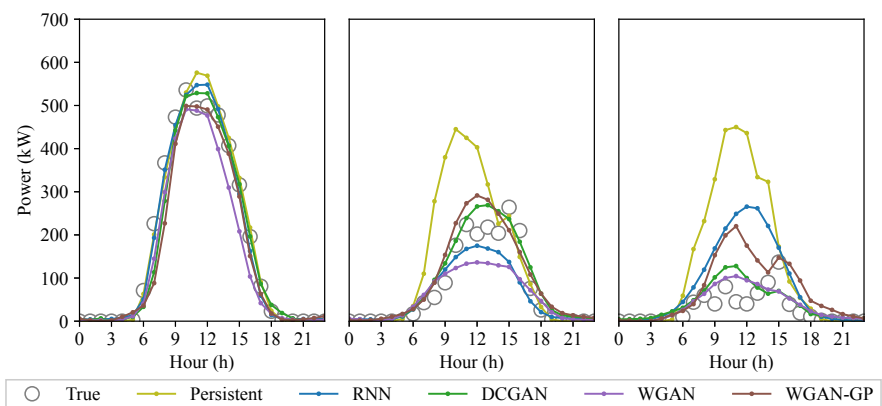

Figure 4.9: Forecast results for high, medium and low power generation dates.

Table 4.3: Accuracy of the Forecast Models

Model	MAE	RMSE	NMAE (%)	NRMSE (%)
Persistent	50.20	99.59	7.17	14.23
EMA	52.49	94.30	7.50	13.47
ARIMA-1	53.32	96.54	7.62	13.79
ARIMA-2	51.47	97.13	7.35	13.88
RNN	35.44	64.99	5.06	9.28
SS	34.77	60.88	4.97	8.70
DCGAN	**28.57**	**50.36**	**4.08**	**7.19**
LSGAN	38.41	70.22	5.49	10.03
WGAN	33.03	58.12	4.72	8.30
WGAN-GP	**31.59**	**54.58**	**4.51**	**7.80**

4.4.4 Incentive Analysis for the PV Power Forecast Results

Table 4.4: Incentives for Hours with more than 10% Usage Rate

Model	NMAE (%)	NRMSE (%)	Elec. Gen. (%) with NAE under 6%	8%	10%	15%
Real	0.00	0.00	90.95	90.95	90.95	90.95
Persistent	12.93	18.39	42.35	50.91	56.36	72.36
EMA	13.41	16.68	20.34	32.53	40.94	64.13
ARIMA-1	13.59	17.10	24.57	30.81	45.22	64.13
ARIMA-2	13.01	16.84	34.59	44.53	48.57	71.56
RNN	8.26	10.47	38.64	57.58	63.44	74.18
SS	9.63	12.05	27.90	44.14	53.77	69.27
DCGAN	**7.27**	**9.07**	41.34	55.09	71.75	**85.60**
LSGAN	9.53	13.35	41.25	48.38	66.03	71.36
WGAN	7.47	9.42	**44.23**	57.46	68.28	80.44
WGAN-GP	7.54	9.89	43.94	**61.80**	**73.06**	80.54

The forecast accuracy incentive conditions in Section 4.3.2, i.e., hourly NAE less than 8%, monthly NMAE less than 10%, and power higher than 10%, were applied to the forecast results of Section 4.4.3. The result is presented in Table 4.4. The theoretical maximum of the incentive revenue was identified as $0.9095 c_i \Sigma x_p^t$ because the incentive is not provided for the hours with a low power generation.

Every benchmark model failed to satisfy the NMAE restriction. SS and LSGAN models reported NMAE values close to it. Applying WGAN-GP to the RNN forecast model enhanced the incentive revenue from $0.5758 c_i \Sigma x_p^t$ to $0.6180 c_i \Sigma x_p^t$, which is equal to the enhancement of 7.33%. If the 8% NAE threshold is relaxed as 10%, the enhancement would be 15.2%.

4.4.5 Effect of Input Data Accuracy on Forecast Results

In addition to the model structure and training dynamics, the quality of input data can affect the forecast accuracy as presented in Fig. 4.3 and Fig. 4.10. A generalized analysis is performed for the incentive revenue with schedule submissions at yesterday 10 h and 17 h. Each submission requires 38-hour or 31-hour length forecasting. More-

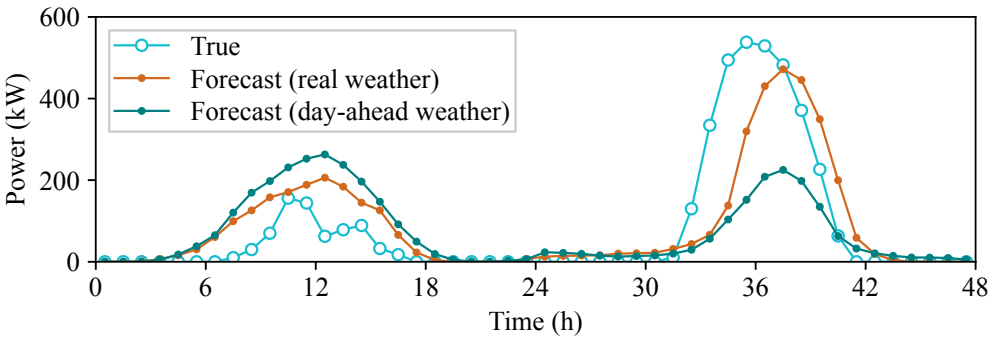

Figure 4.10: Day-ahead PV power forecast results using real (nowcasted) and day-ahead forecasted weather data inputs.

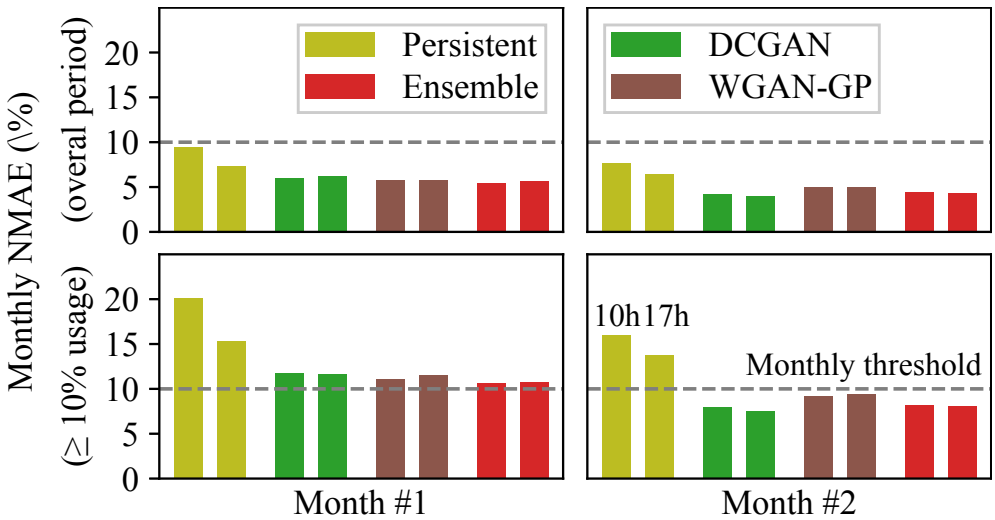

Figure 4.11: Sensitivity of PV power forecast to weather data accuracy.

over, the forecast model can only use the power and NWP data that are updated until the submission time. It is expected that the accuracy of the first submission would be lower than the accuracy of the second submission.

Two-month-length back test results are presented in Fig. 4.11. The persistent model showed notable enhancement with the newly observed power data. However, the monthly NMAE of an RNN-based model only improved by a maximum 0.42 percentage points with the updated power and weather data.

The concept of ensemble is further tested in this study. The ensemble model, comprising a simple average of the results from DCGAN and WGAN-GP models, effectively reduced the forecast error even lower than that of either model.

4.4.6 Robust BESS Scheduling for the Transaction Revenue

A BESS of 300-kW/300-kWh capacity and 95% efficiency is simulated with the energy storage constraint of 150 kWh at midnight and the full SOC range for others.

The 700-kW PV used in the forecast study is assumed to be integrated with the BESS. The hourly power transaction price is obtained from the Korean market for a particular date. The difference between hourly buying and selling prices, i.e., the grid commission, is defined as approximately 4.8% of the maximum buying price.

The robust scheduling problem of (4.30)–(4.34) and (4.61)–(4.63) is day-ahead hourly optimized at yesterday 10 h using CVXPY [157] along with CVXOPT [158] and GLPK [159]. The lower uncertainty bound for the forecasted PV power, $x_{p,min}$, in (4.62) is defined by applying the weight variation from 0% to 100% to the following forecast results:

- The real, perfectly forecasted PV power.
- The persistent-forecasted PV power.
- The ensemble-forecasted PV power of Section 4.4.5.
- The collection of the lowest PV power from the previous seven days of the target forecast date for each hour.

The enhancement in the power transaction revenue is presented in Fig. 4.12. Non-robust scheduling with the perfectly forecasted PV power provides the theoretical maximum revenue. However, non-robust scheduling with an imperfectly forecasted PV power resulted in a significantly low revenue because of the forecast error. Resulting revenues were close to or even lower than the revenue from extreme robust scheduling, which does not consider the forecast results and simply defines the lower uncertainty bound as zero. The result demonstrates the importance of selecting a proper uncertainty range for the robust optimization problem.

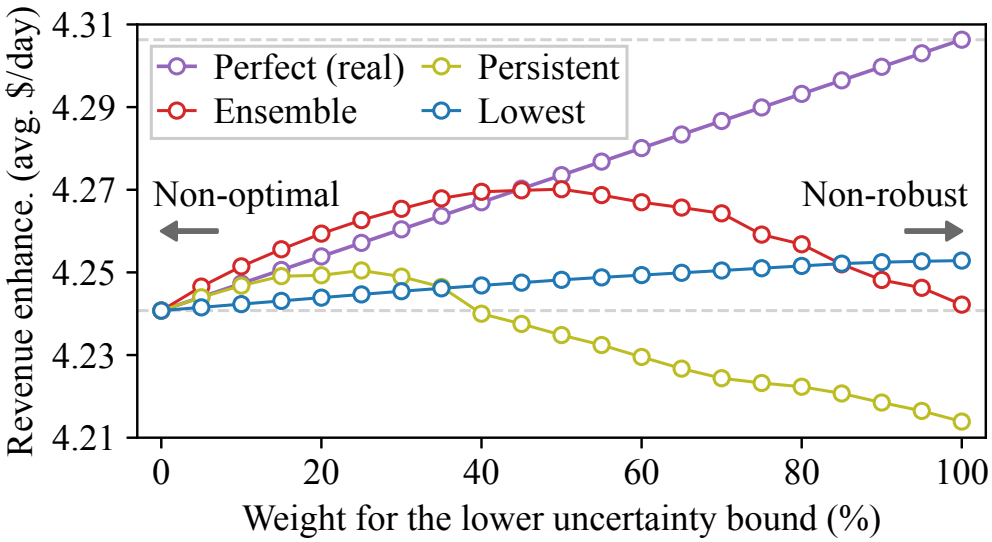

Figure 4.12: Changes in the revenue enhancement with respect to the lower uncertainty bound conditions for the robust optimization.

Collecting the historic low PV power values for each hour was identified as a simple but effective method to estimate the uncertainty bound for the robust BESS scheduling problem. Ensemble forecast result with 50% weight reported the best revenue enhancement. The optimal weight which is less than 100% represents the existence of overestimated values within the forecasted schedule; the lower uncertainty bound, which is defined as a value lower than the possibly overestimated schedule, helps to robustly consider a real PV power which may be lower than the forecasted one. By contrast, applying the weight variation to the perfectly forecasted schedule just decreases the corresponding revenue. A toy example to provide a detailed explanation for this result is presented in Appendix 4.6.1.

A case study for one day shown in Fig. 4.13 provides an idea of how the robust scheduling works. The price signal of Fig. 4.13(a) matches with a typical load trend: hourly electricity price is high during work hours and low at lunchtimes and night

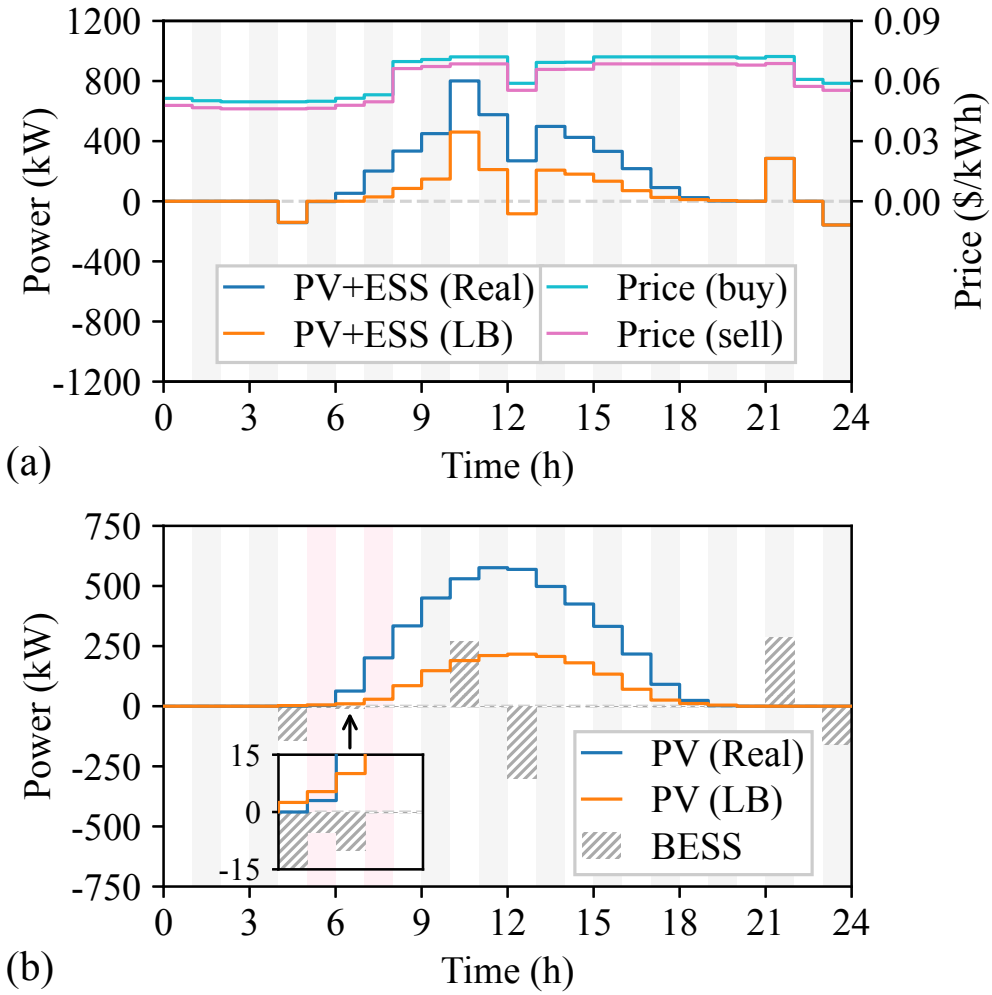

Figure 4.13: Robust BESS scheduling for cost optimization. (a) Hourly price conditions and corresponding net generation schedules. (b) BESS control schedule with respect to the PV power forecast uncertainty.

hours. Cost-optimal BESS control tries to schedule charge operations in low buying-price hours. It further tries to utilize the PV power for the BESS charge, thereby imitating the charge with a selling price. The BESS schedule at 5 h and 6 h in Fig. 4.13(b) shows this result. The BESS was robustly charged using the lowest uncertain amount of the PV power; thus, it offset the selling revenue of the PV operation. The

remaining charge was scheduled for 4 h with the lowest buying price. The underestimation about the PV power at 6 h resulted in the loss of opportunity to charge more power with a lower selling price; whereas the overestimation at 5 h resulted in the partial failure of the robust control.

4.4.7 Computation Speed of the Scheduling Problems

The optimal BESS scheduling problem has been formulated as a non-robust MILP form of (4.25)–(4.29), robust MILP form of (4.40)–(4.48), and robust LP form of (4.61)–(4.63) along with common integer BESS constraints of (4.30)–(4.34). The LP form for the power transaction revenue is further developed into an MILP form of (4.64)–(4.68) and (4.74)–(4.78) with the consideration of forecast accuracy incentive.

Computation time for an optimal scheduling problem must be as short as possible to enable online optimization. The computation time of each problem form was measured under a Linux environment using a single-thread of 2.90 GHz (boosted 4.30 GHz) CPU. Each measurement was independently executed 50 times and then averaged.

The result in Fig. 4.14 identifies exponential growth of the computation time with the number of optimization time steps. Four suggested forms of this study and two reference forms from [148] and [117] were tested. The LP form reported the lowest computation time with 12.3 ms for a 24-hour length time domain and 196 ms for a seven-day length time domain. Adapting the incentive constraints just increased the computation time by 5.40 ms for an one-day length domain and 20.7 ms for a seven-day length domain, thereby enabling its application for online optimization.

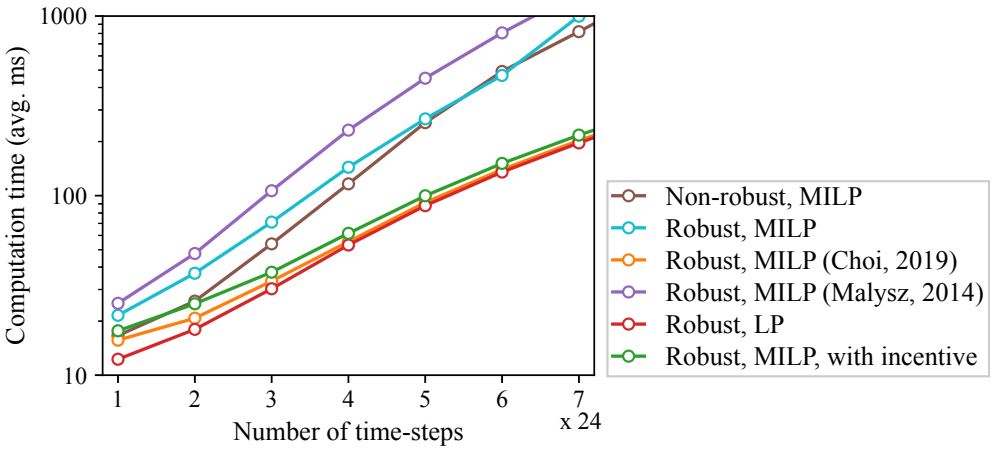

Figure 4.14: Computation time of a cost-optimal BESS scheduling problem with different forms.

4.4.8 Online Optimization for the Incentive Revenue

Online optimization for cost-optimal BESS scheduling continuously updates a control schedule into a more precise one by using the real PV power value of the current time step instead of a forecasted one. It can provide an enhanced revenue compared to the one-time, offline optimization.

Revenue enhancement by applying the online optimization is presented in Fig. 4.15. Ensemble-forecasted PV power of Section 4.4.5 with 50% and 150% weights are applied as the uncertainty bound for the robust optimization problem. Online update of a forecasted PV power schedule is not considered to focus only on the BESS control schedule. Incentive price is defined as approximately 3.8% of the maximum buying price, which is a 1% point lower value than the grid commission.

Compared to the robust one-time optimization using (4.30)–(4.34) and (4.61)–(4.63), the robust online optimization using the same model enhanced the power transaction revenue $-\sum r^t$ as presented in Fig. 4.15(a). However, the incentive rev-

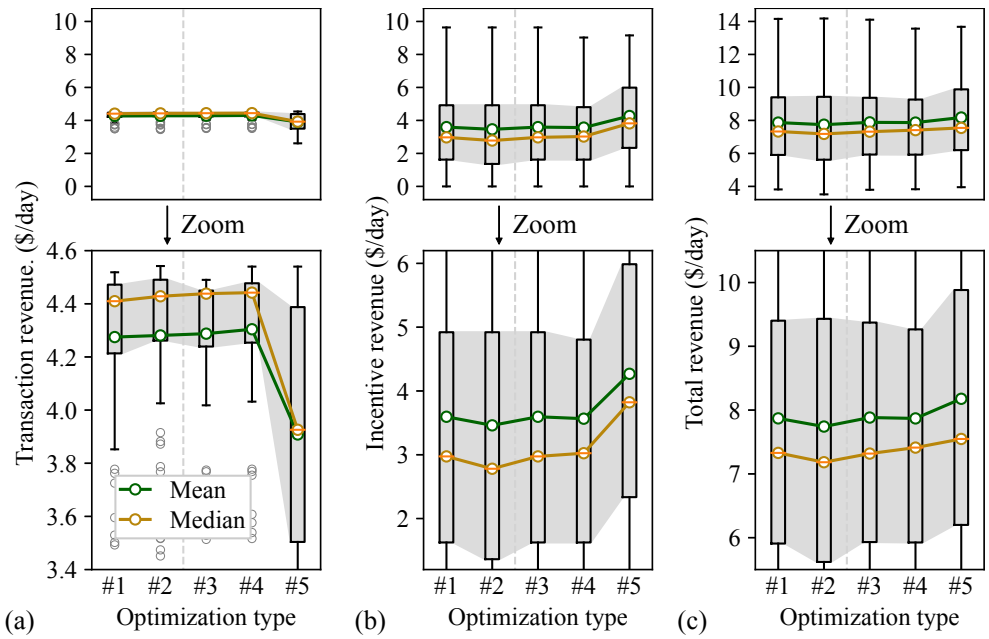

Figure 4.15: Change in revenues with respect to non-robust one-time optimization (#1), non-robust online optimization (#2), robust one-time optimization (#3), robust online optimization (#4), and robust online optimization with incentive consideration (#5). (a) Enhancement in power transaction revenue. (b) Forecast accuracy incentive. (c) Combined revenue enhancement.

enue $\sum i^t$ decreased as presented in Fig. 4.15(b) because of the change in a BESS schedule. The non-robust one-time and online optimization using (4.30)–(4.34) and (4.25)–(4.29) showed the same trend with a lower revenue.

The robust online optimization with the incentive consideration using (4.64)–(4.68) and (4.74)–(4.78) slightly decreased the power transaction revenue but significantly increased the incentive revenue. The total enhancement in both revenues $\sum \left(-r^t + i^t\right)$ reached 3.73% in average; the averaged revenue was increased from 7.88 $/day for the robust one-time optimization to 8.18 $/day for the robust online optimization with the incentive consideration, as presented in Fig 4.15(c).

4.5 Conclusion

This chapter proposed a method to enhance the revenue of a PV-BESS. A grid with a forecast accuracy incentive was considered. Accurate forecasting and robust scheduling algorithms are essential for the PV-BESS owners to maximize both the power transaction and incentive revenues. Introducing GAN-based training to the RNN-based PV power forecast model helped to decrease the gap between training and test dynamics, thereby enhancing stability and accuracy of forecast results. Among four types of GANs tested in this study, WGAN-GP reported superior performance. Additive noise as an adversarial example, or at least as a data augmentation method, also increased the performance of some models, particularly the DCGAN model.

The robust cost-optimal BESS scheduling model of this study was formulated as a concise one to achieve a short computation time. Online optimization with the incentive consideration enhanced the overall revenue of the PV-BESS. Future studies will focus on an approach to relax the remaining integer constraints into affine ones, thereby ensuring online optimization under hardware limitations. Model predictive control on the hardware level is one of the final goals of the future study.

4.6 Appendix

4.6.1 A Toy Example for the Robust Optimization Result

(1) Initial nondeterministic problem ($c_{real} = 4$ and $c_{fcst} \geq 0$):

$$\min_{x,y} \max\left(2x, y - c\right) \quad s.t. \quad x + y \geq -4.$$

(2) Deterministic non-robust equivalent problem:

$$\min_{x,y} r \quad s.t. \quad r \geq 2x,\ r \geq y - c_{fcst},\ x + y \geq -4.$$

(3) Deterministic robust equivalent problem (with 50% weight):

$$\min_{x,y} r \quad s.t. \quad r \geq 2x,\ r \geq y - 0.5c_{fcst},\ x + y \geq -4.$$

Case 1-1: perfectly forecasted $c_{fcst} = 4$, non-robust optimization.

$\Rightarrow$ $x_{opt} = -8/3$, $y_{opt} = -4/3$, $r_{opt} = -16/3$, $r_{real} = -16/3$.

Case 1-2: perfectly forecasted $c_{fcst} = 4$, robust optimization.

$\Rightarrow$ $x_{opt} = -2$, $y_{opt} = -2$, $r_{opt} = -4$, $r_{real} = -4$.

Case 2-1: overestimated $c_{fcst} = 8$, non-robust optimization.

$\Rightarrow$ $x_{opt} = -4$, $y_{opt} = -0$, $r_{opt} = -8$, $r_{real} = -4$.

Case 2-2: overestimated $c_{fcst} = 8$, robust optimization.

$\Rightarrow$ $x_{opt} = -8/3$, $y_{opt} = -4/3$, $r_{opt} = -16/3$, $r_{real} = -16/3$.

4.7 Acknowledgments

© 2021 IEEE. Reprinted, with permission, from Jongwoo Choi, Jeong-In Lee, Il-Woo Lee, and Suk-Won Cha, "Robust PV-BESS Scheduling for a Grid with Incentive for Forecast Accuracy," in *IEEE Transactions on Sustainable Energy,* vol. 13, no. 1, pp. 567-578, Jan. 2022, doi: 10.1109/TSTE.2021.3120451.

In reference to IEEE copyrighted material which is used with permission in this thesis, the IEEE does not endorse any of Seoul National University's products or services. Internal or personal use of this material is permitted. If interested in reprinting/republishing IEEE copyrighted material for advertising or promotional purposes or for creating new collective works for resale or redistribution, please go to http://www.ieee.org/publications_standards/publications/rights/rights_link.html to learn how to obtain a License from RightsLink. If applicable, University Microfilms and/or ProQuest Library, or the Archives of Canada may supply single copies of the dissertation.

Chapter 5

Conclusion

This study presented statistical and control analyses for grid resources to enhance the stability and efficiency on their operations.

Statistical analysis focused on the identification of errors within the grid resource monitoring data. A massive monitoring system was developed to collect real-time monitoring data for PVs distributed throughout Korea. Several types of errors were found during the raw data analysis. Errors within the PV specification data were categorized as missing, redundant, or conflicting ones. Human errors were the main cause of these specification data errors, whereas errors within the monitoring data were also caused by systematic problems. Corrupted values in monitoring data were found as a result of software problems. Inconsistencies in data collection period were originated from connection problems in communication hardware and software. This type of error identification analysis is rare in engineering fields because of the lack of data and the reluctance to share data among different grid resource owners.

The existence of errors within the raw data affects the accuracy of data-driven analyses. The effect of typical errors on the data-driven analysis was particularly evaluated for the statistical PV power forecast model. Value errors in the specification

data exponentially decreased the forecast accuracy, thereby addressing the impact of human errors. Randomly occurred value errors in the monitoring data also linearly decreased the forecast accuracy. However, monitoring data with missing completely at random situation did not affect much to the model accuracy if a proper imputation method was applied during data preprocessing. It is recommended for a monitoring system or EMS to drop every possibly corrupted value before applying monitoring data to data-driven analyses.

The statistical PV power forecast model of this study was formulated as an RNN sequence generator using LSTM. An RNN model is generally trained to optimize its parameters for one-step-ahead forecasting. However, grid or electricity market operators request multi-step-ahead forecasting such as day-ahead hourly ones. It was identified that the discrepancy between the training and test dynamics resulted in unexpected behaviors when the trained model encountered unexposed input values. A GAN-based training framework was applied to the RNN model training process to decrease the gap between training and test dynamics, thereby enhancing stability and accuracy of forecast results. Among several types of GANs tested in this study, WGAN-GP reported superior performance. Additive noise as an adversarial example, or at least as a data augmentation, additionally increased the performance of some training methods, particularly the DCGAN one.

Despite the efforts to enhance the forecast accuracy, errors in forecast results are unavoidable. Control analysis of this study focused on robust and cost-optimal scheduling for an ESS with the consideration for future uncertainty. A virtual power plant or a microgrid with a commercial building load, PV, and ESS was targeted as a behind-the-meter consumer-generator. Economic dispatch control problem under

the electricity market condition was formulated as a mixed-integer linear program. The ESS dispatch schedule was optimized with respect to the predefined time-of-use tariff schedule and the forecasted load power consumption and PV power generation schedules. The robust form of the control problem guaranteed the highest possible market revenue even under the worst-case future uncertainties. Uncertainties in non-dispatchable grid resource operations, which represent forecast errors, were applied as box uncertainty sets of different sizes. Collecting the historic extreme power values for each hour of the day from the previous seven days worked as a simple but effective method to determine the size of the uncertainty set.

The robust cost-optimal control problem was reformulated as a concise equivalent form to enable fast online optimization. The concise problem structure enabled to solve a week-ahead hourly optimization problem within one fifth of a second, which is approximately ten times shorter than the computation time of a benchmark model. Grid ancillary services such as peak control and imbalance tariff were successfully applied to the online optimization with the help of short computation time.

In summary, this study proposed the advances in power forecasting and dispatch scheduling algorithm for grid resources. The result of this study would help enhance the operation of an EMS, thereby contributing toward the realization of smart grid and transactive energy.

Bibliography

[1] U.S. Department of Energy. Electricity 101. URL https://www.energy.gov/oe/information-center/educational-resources/electricity-101.

[2] A Muir and J Lopatto. Final report on the august 14, 2003 blackout in the United States and Canada : causes and recommendations. Technical Report 20461178, U.S.-Canada Power System Outage Task Force, 2004. URL https://www.osti.gov/etdeweb/biblio/20461178.

[3] Joe A. Short, David G. Infield, and Leon L. Freris. Stabilization of grid frequency through dynamic demand control. *IEEE Transactions on Power Systems*, 22(3):1284–1293, 2007. doi: 10.1109/TPWRS.2007.901489.

[4] John Undrill. Primary frequency response and control of power system frequency. NREL 2001105, National Renewable Energy Laboratory (NREL), U.S. Department of Energy, February 2018. URL https://eta.lbl.gov/publications/primary-frequency-response-control.

[5] Juan Pablo Holguin, David Celeita Rodriguez, and Gustavo Ramos. Reverse power flow (rpf) detection and impact on protection coordination of distribution systems. *IEEE Transactions on Industry Applications*, 56(3):2393–2401, 2020. doi: 10.1109/TIA.2020.2969640.

[6] C.L. Masters. Voltage rise: the big issue when connecting embedded generation to long 11 kv overhead lines. *Power Engineering Journal*, 16(1):5–12, 2002. doi: 10.1049/pe:20020101.

[7] Ali Safayet, Poria Fajri, and Iqbal Husain. Reactive power management for overvoltage prevention at high pv penetration in a low-voltage distribution system. *IEEE Transactions on Industry Applications*, 53(6):5786–5794, 2017. doi: 10.1109/TIA.2017.2741925.

[8] Jibran Khan and Mudassar H. Arsalan. Solar power technologies for sustainable electricity generation – a review. *Renewable and Sustainable Energy Reviews*, 55:414–425, 2016. ISSN 1364-0321. doi: https://doi.org/10.1016/j.rser.2015.10.135. URL https://www.sciencedirect.com/science/article/pii/S1364032115012149.

[9] Federal Energy Management Program (FEMP). Using distributed energy resources: A how-to guide for federal facility managers. DOE/GO 102002-1520, Office of Energy Efficiency and Renewable Energy (EERE), U.S. Department of Energy, May 2002. URL https://www.nrel.gov/docs/fy02osti/31570.pdf.

[10] George Zhou, David Wang, Adham Atallah, Frank McElvain, Ram Nath, John Jontry, Christopher Bolton, Huang Lin, and Andreas Haselbauer. Synchronous condenser applications: Under significant resource portfolio changes. *IEEE Power and Energy Magazine*, 17(4):35–46, 2019. doi: 10.1109/MPE.2019.2909005.

[11] California Independent System Operator. What the duck curve tells us about managing a green grid, 2013. URL https://www.caiso.com/documents/flexibleresourceshelprenewables_fastfacts.pdf.

[12] Santosh Veda, Yingchen Zhang, Jin Tan, Erol Kevin Chartan, Jonathan Duckworth, Nicholas Gilroy, Dylan J. Hettinger, Sean J. Ericson, Jason Ausmus, Slaven Kincic, Xiaping Zhang, and Guohui Yuan. Evaluating the impact of the 2017 solar eclipse on U.S. western interconnection operations. NREL/TP 5D00-71147, National Renewable Energy Laboratory (NREL), U.S. Department of Energy, April 2018. URL https://www.osti.gov/biblio/1435500.

[13] Emma Marris. Energy: Upgrading the grid. *Nature News*, 454(7204):570–573, 2008. doi: 10.1038/454570a.

[14] Smart Grid Mandate. Standardization mandate to european standardisation organisations (esos) to support european smart grid deployment. Mandate 490, Directorate-General for Energy, European Commission, March

2011. URL https://ec.europa.eu/energy/sites/ener/files/documents/2011_03_01_mandate_m490_en.pdf.

[15] United States Congress. Energy independence and security act, 2007. URL https://www.govinfo.gov/content/pkg/STATUTE-121/pdf/STATUTE-121-Pg1492.pdf.

[16] National Institute of Standards and U.S. Department of Commerce Technology (NIST). Transactive energy: An overview. URL https://www.nist.gov/engineering-laboratory/smart-grid/hot-topics/transactive-energy-overview.

[17] The GridWise Architecture Council. Gridwise transactive energy framework version 1.0. PNNL 22946, The GridWise Architecture Council (GWAC), U.S. Department of Energy, January 2015. URL https://www.gridwiseac.org/pdfs/te_framework_report_pnnl-22946.pdf.

[18] PJM. Market for electricity, . URL https://learn.pjm.com/electricity-basics/market-for-electricity.aspx.

[19] Ausgrid. Time of use pricing. URL https://www.ausgrid.com.au/Your-energy-use/Meters/Time-of-use-pricing.

[20] International Renewable Energy Agency (IRENA). Time-of-use tariffs: Innovation landscape brief. Technical report, June 2019. URL https://www.irena.org/publications/2019/Jun/Market-Design-Innovation-Landscape-briefs.

[21] Energy UK. Ancillary services report 2017. Technical report, April 2017. URL https://www.energy-uk.org.uk/publication.html?task=file.download&id=6138.

[22] International Renewable Energy Agency (IRENA). Innovative ancillary services: innovation landscape brief. Technical report, June 2019. URL https://www.irena.org/publications/2019/Jun/Market-Design-Innovation-Landscape-briefs.

[23] PJM. Ancillary services market, . URL https://learn.pjm.com/three-priorities/buying-and-selling-energy/ancillary-services-market.aspx.

[24] Furkan Dinçer. The analysis on photovoltaic electricity generation status, potential and policies of the leading countries in solar energy. *Renewable and Sustainable Energy Reviews*, 15(1):713–720, 2011. ISSN 1364-0321. doi: https://doi.org/10.1016/j.rser.2010.09.026. URL https://www.sciencedirect.com/science/article/pii/S1364032110003138.

[25] S.M. Moosavian, N.A. Rahim, J. Selvaraj, and K.H. Solangi. Energy policy to promote photovoltaic generation. *Renewable and Sustainable Energy Reviews*, 25:44–58, 2013. ISSN 1364-0321. doi: https://doi.org/10.1016/j.rser.2013.03.030. URL https://www.sciencedirect.com/science/article/pii/S1364032113001895.

[26] M. Hosenuzzaman, N.A. Rahim, J. Selvaraj, M. Hasanuzzaman, A.B.M.A. Malek, and A. Nahar. Global prospects, progress, policies, and environmental impact of solar photovoltaic power generation. *Renewable and Sustainable Energy Reviews*, 41:284–297, 2015. ISSN 1364-0321. doi: https://doi.org/10.1016/j.rser.2014.08.046. URL https://www.sciencedirect.com/science/article/pii/S1364032114007229.

[27] Hamed Hafeznia, Alireza Aslani, Sohail Anwar, and Mahdis Yousefjamali. Analysis of the effectiveness of national renewable energy policies: A case of photovoltaic policies. *Renewable and Sustainable Energy Reviews*, 79:669–680, 2017. ISSN 1364-0321. doi: https://doi.org/10.1016/j.rser.2017.05.033. URL https://www.sciencedirect.com/science/article/pii/S1364032117306718.

[28] Aishwarya S. Mundada, Emily W. Prehoda, and Joshua M. Pearce. U.s. market for solar photovoltaic plug-and-play systems. *Renewable Energy*, 103:255–264, 2017. ISSN 0960-1481. doi: https://doi.org/10.1016/j.renene.2016.11.034. URL https://www.sciencedirect.com/science/article/pii/S0960148116310035.

[29] Jinqing Peng, Lin Lu, and Hongxing Yang. Review on life cycle assessment of energy payback and greenhouse gas emission of solar photovoltaic systems. *Renewable and Sustainable Energy Reviews*, 19:255–274, 2013.

ISSN 1364-0321. doi: https://doi.org/10.1016/j.rser.2012.11.035. URL https://www.sciencedirect.com/science/article/pii/S1364032112006478.

[30] Hassan Radhi. Trade-off between environmental and economic implications of pv systems integrated into the uae residential sector. *Renewable and Sustainable Energy Reviews*, 16(5):2468–2474, 2012. ISSN 1364-0321. doi: https://doi.org/10.1016/j.rser.2012.01.048. URL https://www.sciencedirect.com/science/article/pii/S1364032112000494.

[31] Toshihiro Mukai, Maurizio Tomasella, Ajith Kumar Parlikad, Naoya Abe, and Yuzuru Ueda. The competitiveness of continuous monitoring of residential pv systems: A model and insights from the japanese market. *IEEE Transactions on Sustainable Energy*, 5(4):1176–1183, 2014. doi: 10.1109/TSTE.2014.2338933.

[32] Nadav Enbar, Dean Weng, and Geoffrey Taylor Klise. Budgeting for solar pv plant operations & maintenance: Practices and pricing. Technical Report SAND-2016-0649R, Sandia National Laboratories, 2016. URL https://www.osti.gov/biblio/1237001-budgeting-solar-pv-plant-operations-maintenance-practices-pricing.

[33] Soham Adhya, Dipak Saha, Abhijit Das, Joydip Jana, and Hiranmay Saha. An iot based smart solar photovoltaic remote monitoring and control unit. In *Proceedings of the 2nd International Conference on Control, Instrumentation, Energy & Communication (CIEC)*, pages 432–436, Kolkata, India, 2016. doi: 10.1109/CIEC.2016.7513793.

[34] K. Branker, M.J.M. Pathak, and J.M. Pearce. A review of solar photovoltaic levelized cost of electricity. *Renewable and Sustainable Energy Reviews*, 15(9):4470–4482, 2011. ISSN 1364-0321. doi: https://doi.org/10.1016/j.rser.2011.07.104. URL https://www.sciencedirect.com/science/article/pii/S1364032111003492.

[35] Lennart Peters and Reinhard Madlener. Economic evaluation of maintenance strategies for ground-mounted solar photovoltaic plants. *Applied En-*

ergy, 199:264–280, 2017. ISSN 0306-2619. doi: https://doi.org/10.1016/j.apenergy.2017.04.060. URL https://www.sciencedirect.com/science/article/pii/S0306261917304579.

[36] Mark D. Hopkins, Anil Pahwa, and Todd Easton. Intelligent dispatch for distributed renewable resources. *IEEE Transactions on Smart Grid*, 3(2):1047–1054, 2012. doi: 10.1109/TSG.2012.2190946.

[37] Khashayar Mahani, Zhenglin Liang, Ajith Kumar Parlikad, and Mohsen A. Jafari. Joint optimization of operation and maintenance policies for solar-powered microgrids. *IEEE Transactions on Sustainable Energy*, 10(2):833–842, 2019. doi: 10.1109/TSTE.2018.2849318.

[38] Sobrina Sobri, Sam Koohi-Kamali, and Nasrudin Abd. Rahim. Solar photovoltaic generation forecasting methods: A review. *Energy Conversion and Management*, 156:459–497, 2018. ISSN 0196-8904. doi: https://doi.org/10.1016/j.enconman.2017.11.019. URL https://www.sciencedirect.com/science/article/pii/S0196890417310622.

[39] Gabriel de Freitas Viscondi and Solange N. Alves-Souza. A systematic literature review on big data for solar photovoltaic electricity generation forecasting. *Sustainable Energy Technologies and Assessments*, 31:54–63, 2019. ISSN 2213-1388. doi: https://doi.org/10.1016/j.seta.2018.11.008. URL https://www.sciencedirect.com/science/article/pii/S2213138818301036.

[40] Fernando A. Olivencia Polo, Jesús Ferrero Bermejo, Juan F. Gómez Fernández, and Adolfo Crespo Márquez. Failure mode prediction and energy forecasting of pv plants to assist dynamic maintenance tasks by ann based models. *Renewable Energy*, 81:227–238, 2015. ISSN 0960-1481. doi: https://doi.org/10.1016/j.renene.2015.03.023. URL https://www.sciencedirect.com/science/article/pii/S0960148115002050.

[41] Tao Hu, Minghui Zheng, Jianjun Tan, Li Zhu, and Wang Miao. Intelligent photovoltaic monitoring based on solar irradiance big data and wireless sensor networks. *Ad Hoc Networks*, 35:127–136, 2015. ISSN 1570-8705. doi: https:

//doi.org/10.1016/j.adhoc.2015.07.004. URL https://www.sciencedirect.com/science/article/pii/S1570870515001390. Special Issue on Big Data Inspired Data Sensing, Processing and Networking Technologies.

[42] Silvano Vergura, Giuseppe Acciani, Vitantonio Amoruso, Giuseppe E. Patrono, and Francesco Vacca. Descriptive and inferential statistics for supervising and monitoring the operation of pv plants. *IEEE Transactions on Industrial Electronics*, 56(11):4456–4464, 2009. doi: 10.1109/TIE.2008.927404.

[43] Muhammad Ismail, Mostafa F. Shaaban, Mahesh Naidu, and Erchin Serpedin. Deep learning detection of electricity theft cyber-attacks in renewable distributed generation. *IEEE Transactions on Smart Grid*, 11(4):3428–3437, 2020. doi: 10.1109/TSG.2020.2973681.

[44] Saveli I Goldberg, Andrzej Niemierko, and Alexander Turchin. Analysis of data errors in clinical research databases. In *AMIA Annual Symposium Proceedings*, pages 242–246, Washington, DC, 2008.

[45] Danielle G. T. Arts, Nicolette F. de Keizer, and Gert-Jan Scheffer. Defining and Improving Data Quality in Medical Registries: A Literature Review, Case Study, and Generic Framework. *Journal of the American Medical Informatics Association*, 9(6):600–611, 11 2002. ISSN 1067-5027. doi: 10.1197/jamia.M1087. URL https://doi.org/10.1197/jamia.M1087.

[46] Jiang Zhu, Yingning Qiu, Thomas R. Betts, and Ralph Gottschalg. Outlier identification in outdoor measurement data - effects of different strategies on the performance descriptors of photovoltaic modules. In *Proceedings of the 34th IEEE Photovoltaic Specialists Conference (PVSC)*, pages 000828–000833, Philadelphia, PA, 2009. doi: 10.1109/PVSC.2009.5411160.

[47] Chongqing Kang, Yi Wang, Yusheng Xue, Gang Mu, and Ruijin Liao. Big data analytics in china's electric power industry: Modern information, communication technologies, and millions of smart meters. *IEEE Power and Energy Magazine*, 16(3):54–65, 2018. doi: 10.1109/MPE.2018.2790819.

[48] Wen Chen, Kaile Zhou, Shanlin Yang, and Cheng Wu. Data quality of electricity consumption data in a smart grid environment. *Renewable and Sustainable Energy Reviews*, 75:98–105, 2017. ISSN 1364-0321. doi: https://doi.org/10.1016/j.rser.2016.10.054. URL https://www.sciencedirect.com/science/article/pii/S1364032116307109.

[49] Dazhi Yang. A correct validation of the national solar radiation data base (nsrdb). *Renewable and Sustainable Energy Reviews*, 97:152–155, 2018. ISSN 1364-0321. doi: https://doi.org/10.1016/j.rser.2018.08.023. URL https://www.sciencedirect.com/science/article/pii/S1364032118306087.

[50] Andreas Livera, Marios Theristis, Elena Koumpli, Spyros Theocharides, George Makrides, Juergen Sutterlueti, Joshua S. Stein, and George E. Georghiou. Data processing and quality verification for improved photovoltaic performance and reliability analytics. *Progress in Photovoltaics: Research and Applications*, 29(2):143–158, 2021. doi: https://doi.org/10.1002/pip.3349. URL https://onlinelibrary.wiley.com/doi/abs/10.1002/pip.3349.

[51] Juan Shishido. Smart meter data quality insights. In *Proceedings of the ACEEE Summer Study on Energy Efficiency in Buildings*, volume 12, pages 277–288, Pacific Grove, CA, 2012. URL https://www.aceee.org/files/proceedings/2012/data/papers/0193-000375.pdf.

[52] Mouzhi Ge, Stanislav Chren, Bruno Rossi, and Tomas Pitner. Data quality management framework for smart grid systems. In Witold Abramowicz and Rafael Corchuelo, editors, *Business Information Systems*, pages 299–310, Seville, Spain, 2019. Springer International Publishing. ISBN 978-3-030-20482-2.

[53] Rob J Hyndman and George Athanasopoulos. *Forecasting: principles and practice*. OTexts, Melbourne, Australia, 2018.

[54] Kadir Amasyali and Nora M. El-Gohary. A review of data-driven building energy consumption prediction studies. *Renewable and Sustainable Energy Reviews*, 81:1192–1205, 2018. ISSN 1364-0321. doi: https://doi.org/10.

1016/j.rser.2017.04.095. URL https://www.sciencedirect.com/science/article/pii/S1364032117306093.

[55] Yulei He. Missing data analysis using multiple imputation. *Circulation: Cardiovascular Quality and Outcomes*, 3(1):98–105, 2010. doi: 10.1161/CIRCOUTCOMES.109.875658. URL https://www.ahajournals.org/doi/abs/10.1161/CIRCOUTCOMES.109.875658.

[56] Marianne Riksheim Stavseth, Thomas Clausen, and Jo Røislien. How handling missing data may impact conclusions: A comparison of six different imputation methods for categorical questionnaire data. *SAGE Open Medicine*, 7:2050312118822912, 2019. doi: 10.1177/2050312118822912. URL https://doi.org/10.1177/2050312118822912.

[57] Jie Lin, NianHua Li, Md Ashraful Alam, and Yuqing Ma. Data-driven missing data imputation in cluster monitoring system based on deep neural network. *Applied Intelligence*, 50(3):860–877, 2020. ISSN 1573-7497. doi: 10.1007/s10489-019-01560-y. URL https://doi.org/10.1007/s10489-019-01560-y.

[58] *Alternative Energy Development Promotion Act*. Korea Ministry of Trade, Industry and Energy, 1987. URL https://www.law.go.kr/%EB%B2%95%EB%A0%B9/%EB%8C%80%EC%B2%B4%EC%97%90%EB%84%88%EC%A7%80%EA%B0%9C%EB%B0%9C%EC%B4%89%EC%A7%84%EB%B2%95/(03990,19871204).

[59] *The Third National Energy Master Plan (2019-2040)*. Korea Ministry of Trade, Industry and Energy, 2019. URL http://www.korea.kr/briefing/pressReleaseView.do?newsId=156334773.

[60] *Survey on deployment of New & Renewable energy: Energy Generation (1995-2017)*. Korea Energy Agency, 2018. URL http://kosis.kr/statHtml/statHtml.do?orgId=337&tblId=DT_337N_A002.

[61] *Survey on Deployment of New & Renewable Energy: Energy Deployment Capacity (Generation-Accumulated) (2005-2017)*. Korea Energy

Agency, 2018. URL http://kosis.kr/statHtml/statHtml.do?orgId=337&tblId=DT_337N_A005A.

[62] Industry Korea Ministry of Trade and Energy. [press release] strength the safety inspection for solar power plants to prepare for the 19th typhoon soulik, 2018. URL https://www.gov.kr/portal/ntnadmNews/1571739.

[63] Industry Korea Ministry of Trade and Energy. [press release] starting safety inspections for solar power plants, 2018. URL http://www.motie.go.kr/motie/ne/presse/press2/bbs/bbsView.do?bbs_cd_n=81&bbs_seq_n=160726.

[64] *Electric Utility Act*. Korea Ministry of Trade, Industry and Energy, 2019. URL https://www.law.go.kr/%EB%B2%95%EB%A0%B9/%EC%A0%84%EA%B8%B0%EC%82%AC%EC%97%85%EB%B2%95.

[65] *Statistical Report on The Electric Safety of Electric Installations for General Use 2018*. Korea Electrical Safety Corporation, 2019. URL http://www.kesco.or.kr/cop/bbs/selectBoardList.do?bbsId=BBSMSTR_000000003363&menuId=MNU_0000000000001077.

[66] *Electric Utility Act Amendment Bill*. Korea Ministry of Trade, Industry and Energy, 2018. URL http://likms.assembly.go.kr/bill/billDetail.do?billId=PRC_V1Z8Z1Z1S1R4P1X6P3Y2O3A4S5B3Z6.

[67] *Survey on Deployment of New & Renewable Energy: Solar Energy–Solar Photovoltaic (2016-2017)*. Korea Energy Agency, 2018. URL http://kosis.kr/statHtml/statHtml.do?orgId=337&tblId=DT_337001N_A002.

[68] Il-Yeol Song, Mary Evans, and Eun K Park. A comparative analysis of entity-relationship diagrams. *Journal of Computer and Software Engineering*, 3(4): 427–459, 1995.

[69] Howard E. Watson. Watt-hour meter maintenance and testing. In *Facilities instructions, standards, and techniques (FIST) Manuals*, volume 3-10. U.S. Bureau of Reclamation, 1992. URL https://www.usbr.gov/power/data/fist_pub.html.

[70] Du Stefanus Toit. Working draft, standard for programming language c++. Technical Report N3337, International Organization for Standardization (ISO) and International Electrotechnical Commission (IEC), 2012.

[71] *CWE-466: Return of Pointer Value Outside of Expected Range*. MITRE, 2006. URL https://cwe.mitre.org/data/definitions/466.html.

[72] *CWE-120: Buffer Copy without Checking Size of Input*. MITRE, 2006. URL https://cwe.mitre.org/data/definitions/120.html.

[73] *CWE-190: Integer Overflow or Wraparound*. MITRE, 2006. URL https://cwe.mitre.org/data/definitions/190.html.

[74] Korea Power Exchange. Open api for the electric market information by the korea power exchange, 2015. URL https://www.data.go.kr/dataset/3043737/openapi.do.

[75] Korea Meteorological Administration. Open api for the weather forecasting service by the korea meteorological administration, 2012. URL https://www.data.go.kr/dataset/15000099/openapi.do.

[76] Gordon Reikard. Predicting solar radiation at high resolutions: A comparison of time series forecasts. *Solar Energy*, 83(3):342–349, 2009. ISSN 0038-092X. doi: https://doi.org/10.1016/j.solener.2008.08.007. URL https://www.sciencedirect.com/science/article/pii/S0038092X08002107.

[77] Yue Zhang, Marc Beaudin, Hamidreza Zareipour, and David Wood. Forecasting solar photovoltaic power production at the aggregated system level. In *Proceedings of the North American Power Symposium (NAPS)*, pages 1–6, Pullman, WA, 2014. doi: 10.1109/NAPS.2014.6965389.

[78] R. Ahmed, V. Sreeram, Y. Mishra, and M.D. Arif. A review and evaluation of the state-of-the-art in pv solar power forecasting: Techniques and optimization. *Renewable and Sustainable Energy Reviews*, 124:109792, 2020. ISSN 1364-0321. doi: https://doi.org/10.1016/j.rser.2020.109792. URL https://www.sciencedirect.com/science/article/pii/S1364032120300885.

[79] Woonghee Lee, Keonwoo Kim, Junsep Park, Jinhee Kim, and Younghoon Kim. Forecasting solar power using long-short term memory and convolutional neural networks. *IEEE Access*, 6:73068–73080, 2018. doi: 10.1109/ACCESS.2018.2883330.

[80] Hangxia Zhou, Yujin Zhang, Lingfan Yang, Qian Liu, Ke Yan, and Yang Du. Short-term photovoltaic power forecasting based on long short term memory neural network and attention mechanism. *IEEE Access*, 7:78063–78074, 2019. doi: 10.1109/ACCESS.2019.2923006.

[81] Jianqin Zheng, Haoran Zhang, Yuanhao Dai, Bohong Wang, Taicheng Zheng, Qi Liao, Yongtu Liang, Fengwei Zhang, and Xuan Song. Time series prediction for output of multi-region solar power plants. *Applied Energy*, 257:114001, 2020. ISSN 0306-2619. doi: https://doi.org/10.1016/j.apenergy.2019.114001. URL https://www.sciencedirect.com/science/article/pii/S0306261919316885.

[82] Sepp Hochreiter and Jürgen Schmidhuber. Long short-term memory. *Neural Computation*, 9(8):1735–1780, 1997. ISSN 0899-7667. doi: 10.1162/neco.1997.9.8.1735.

[83] Vinod Nair and Geoffrey E. Hinton. Rectified linear units improve restricted boltzmann machines. In *Proceedings of the 27th International Conference on International Conference on Machine Learning (ICML)*, page 807–814, Haifa, Israel, 2010.

[84] Nitish Srivastava, Geoffrey Hinton, Alex Krizhevsky, Ilya Sutskever, and Ruslan Salakhutdinov. Dropout: A simple way to prevent neural networks from overfitting. *Journal of Machine Learning Research*, 15(56):1929–1958, 2014.

[85] Jimmy Lei Ba, Jamie Ryan Kiros, and Geoffrey E. Hinton. Layer normalization. In *Proceedings of the 32nd International Conference on Neural Information Processing Systems (NIPS)*, pages 1–14, Barcelona, Spain, 2016.

[86] Alex M Lamb, Anirudh Goyal ALIAS PARTH GOYAL, Ying Zhang, Saizheng Zhang, Aaron C Courville, and Yoshua Bengio. Professor forcing: A new algorithm for training recurrent networks. In *Proceedings of the 32nd International Conference on Neural Information Processing Systems (NIPS)*, pages 4601–4609, Barcelona, Spain, 2016.

[87] Pengfei Chen, Guangyong Chen, and Shengyu Zhang. Log hyperbolic cosine loss improves variational auto-encoder, 2019. URL https://openreview.net/forum?id=rkglvsC9Ym.

[88] Jinsong Zhang, Rodrigo Verschae, Shohei Nobuhara, and Jean-François Lalonde. Deep photovoltaic nowcasting. *Solar Energy*, 176:267–276, 2018. ISSN 0038-092X. doi: https://doi.org/10.1016/j.solener.2018.10.024.

[89] A. Gensler, J. Henze, B. Sick, and N. Raabe. Deep learning for solar power forecasting — an approach using AutoEncoder and LSTM neural networks. In *Proceedings of the IEEE International Conference on Systems, Man, and Cybernetics (SMC)*, pages 2858–2865, Budapest, Hungary, 2016.

[90] Jie Zhang, Bri-Mathias Hodge, Anthony Florita, Siyuan Lu, Hendrik F Hamann, and Venkat Banunarayanan. Metrics for evaluating the accuracy of solar power forecasting. NREL/CP 5500-60142, National Renewable Energy Laboratory (NREL), U.S. Department of Energy, October 2013.

[91] Jiyong Eom, Minwoo Hyun, Jaewoong Lee, and Hyoseop Lee. Increase in household energy consumption due to ambient air pollution. *Nature Energy*, 2020. ISSN 2058-7546. doi: 10.1038/s41560-020-00698-1. URL https://doi.org/10.1038/s41560-020-00698-1.

[92] Pan He, Jing Liang, Yueming (Lucy) Qiu, Qingran Li, and Bo Xing. Increase in domestic electricity consumption from particulate air pollution. *Nature Energy*, 2020. ISSN 2058-7546. doi: 10.1038/s41560-020-00699-0. URL https://doi.org/10.1038/s41560-020-00699-0.

[93] John A Duffie and William A Beckman. *Solar Engineering of Thermal Processes*. John Wiley & Sons, Hoboken, NJ, 2013.

[94] Garrett Birkhoff and Henry L Garabedian. Smooth surface interpolation. *Journal of Mathematics and Physics*, 39(1-4):258–268, 4 1960. ISSN 0097-1421. doi: 10.1002/sapm1960391258. doi: 10.1002/sapm1960391258.

[95] Stef van Buuren and Karin Groothuis-Oudshoorn. mice: Multivariate imputation by chained equations in r. *Journal of Statistical Software, Articles*, 45(3):1–67, 2011. ISSN 1548-7660. doi: 10.18637/jss.v045.i03. URL https://www.jstatsoft.org/v045/i03.

[96] Melissa J Azur, Elizabeth A Stuart, Constantine Frangakis, and Philip J Leaf. Multiple imputation by chained equations: what is it and how does it work? *International Journal of Methods in Psychiatric Research*, 20(1):40–49, 3 2011. ISSN 1049-8931. doi: 10.1002/mpr.329.

[97] Concepción Turrado, María López, Fernando Lasheras, Benigno Gómez, José Rollé, and Francisco Juez. Missing data imputation of solar radiation data under different atmospheric conditions. *Sensors*, 14(11):20382–20399, 10 2014. ISSN 1424-8220. doi: 10.3390/s141120382.

[98] U.S. Department of Energy. 2012 DOE microgrid workshop summary report, September 2012. URL http://energy.gov/oe/downloads/2012-doe-microgrid-workshop-summary-report-september-2012.

[99] Robert Lasseter, Abbas Akhil, Chris Marnay, John Stephens, Jeff Dagle, Ross Guttromson, A Meliopoulous, Robert Yinger, and Joe Eto. The CERTS microgrid concept. *White Paper for Transmission Reliability Program, Office of Power Technologies, U.S. Department of Energy*, April 2002.

[100] Amjad Anvari Moghaddam, Alireza Seifi, Taher Niknam, and Mohammad Reza Alizadeh Pahlavani. Multi-objective operation management of a renewable MG (micro-grid) with back-up micro-turbine/fuel cell/battery hybrid power source. *Energy*, 36(11):6490–6507, 2011.

[101] Jong-Yul Kim, Jin-Hong Jeon, Seul-Ki Kim, Changhee Cho, June Ho Park, Hak-Man Kim, and Kee-Young Nam. Cooperative control strategy of energy storage system and microsources for stabilizing the microgrid during islanded operation. *IEEE Transactions on Power Electronics*, 25(12):3037–3048, 2010.

[102] Wenbo Shi, Xiaorong Xie, Chi-Cheng Chu, and Rajit Gadh. Distributed optimal energy management in microgrids. *IEEE Transactions on Smart Grid*, 6 (3):1137–1146, 2015.

[103] Yingmeng Xiang, Jiangchuan Liu, and Yanbing Liu. Robust energy management of microgrid with uncertain renewable generation and load. *IEEE Transactions on Smart Grid*, 7(2):1034–1043, 2016.

[104] Xianjun Zhang, Ratnesh Sharma, and Yanyi He. Optimal energy management of a rural microgrid system using multi-objective optimization. In *Proceedings of the IEEE PES Innovative Smart Grid Technologies Conference (ISGT)*, pages 1–8, Washington, DC, 2012.

[105] Xiong Wu, Xiuli Wang, and Chong Qu. A hierarchical framework for generation scheduling of microgrids. *IEEE Transactions on Power Delivery*, 29(6): 2448–2457, 2014.

[106] Waleed KA Najy, Hatem H Zeineldin, and Wei Lee Woon. Optimal protection coordination for microgrids with grid-connected and islanded capability. *IEEE Transactions on Industrial Electronics*, 60(4):1668–1677, 2013.

[107] Faisal A Mohamed and Heikki N Koivo. Online management genetic algorithms of microgrid for residential application. *Energy Conversion and Management*, 64:562–568, 2012.

[108] Jong-Bae Park, Ki-Song Lee, Joong-Rin Shin, and Ki-Song Lee. A particle swarm optimization for economic dispatch with nonsmooth cost functions. *IEEE Transactions on Power Systems*, 20(1):34–42, 2005.

[109] Yoash Levron, Josep M Guerrero, and Yuval Beck. Optimal power flow in

microgrids with energy storage. *IEEE Transactions on Power Systems*, 28(3): 3226–3234, 2013.

[110] David G. Luenberger and Yinyu Ye. Basic properties of linear programs. In Frederick S. Hillier, editor, *Linear and Nonlinear Programming*, International Series in Operations Research & Management Science, pages 29–48, New York, NY, 2015. Springer.

[111] Zeyuan Allen-Zhu and Lorenzo Orecchia. Nearly-linear time packing and covering lp solvers. *arXiv:1411.1124v2 [cs.DS]*, August 2016.

[112] Manfred Padberg and Giovanni Rinaldi. A branch-and-cut algorithm for the resolution of large-scale symmetric traveling salesman problems. *SIAM Review*, 33(1):60–100, 1991.

[113] Hugo Morais, Peter Kadar, Pedro Faria, Zita A Vale, and HM Khodr. Optimal scheduling of a renewable micro-grid in an isolated load area using mixed-integer linear programming. *Renewable Energy*, 35(1):151–156, 2010.

[114] Anderson Hoke, Alexander Brissette, Shawn Chandler, Annabelle Pratt, and Dragan Maksimovizc. Look-ahead economic dispatch of microgrids with energy storage, using linear programming. In *Proceedings of the IEEE Conference on Technologies for Sustainability (SusTech)*, pages 154–161, Portland, OR, 2013.

[115] Quanyuan Jiang, Meidong Xue, and Guangchao Geng. Energy management of microgrid in grid-connected and stand-alone modes. *IEEE Transactions on Power Systems*, 28(3):3380–3389, 2013.

[116] Edmund Handschin, F Neise, H Neumann, and R Schultz. Optimal operation of dispersed generation under uncertainty using mathematical programming. *International Journal of Electrical Power & Energy Systems*, 28(9):618–626, 2006.

[117] Pawel Malysz, Shahin Sirouspour, and Ali Emadi. An optimal energy storage

control strategy for grid-connected microgrids. *IEEE Transactions on Smart Grid*, 5(4):1785–1796, 2014.

[118] Alessandra Parisio, Evangelos Rikos, and Luigi Glielmo. A model predictive control approach to microgrid operation optimization. *IEEE Transactions on Control Systems Technology*, 22(5):1813–1827, 2014.

[119] Ionela Prodan and Enrico Zio. A model predictive control framework for reliable microgrid energy management. *International Journal of Electrical Power & Energy Systems*, 61:399–409, 2014.

[120] Rodrigo Palma-Behnke, Carlos Benavides, Fernando Lanas, Bernardo Severino, Lorenzo Reyes, Jacqueline Llanos, and Doris Sáez. A microgrid energy management system based on the rolling horizon strategy. *IEEE Transactions on Smart Grid*, 4(2):996–1006, 2013.

[121] Kwi-Seong Jeong, Won-Yong Lee, and Chang-Soo Kim. Energy management strategies of a fuel cell/battery hybrid system using fuzzy logics. *Journal of Power Sources*, 145(2):319–326, 2005.

[122] Volkan Sezer, Metin Gokasan, and Seta Bogosyan. A novel ecms and combined cost map approach for high-efficiency series hybrid electric vehicles. *IEEE Transactions on Vehicular Technology*, 60(8):3557–3570, 2011.

[123] Burak Turker, Sebastian Arroyo Klein, Eva-Maria Hammer, Bettina Lenz, and Lidiya Komsiyska. Modeling a vanadium redox flow battery system for large scale applications. *Energy Conversion and Management*, 66:26–32, 2013.

[124] Steven T Bushby. BACnet™: a standard communication infrastructure for intelligent buildings. *Automation in Construction*, 6(5):529–540, 1997.

[125] *Communication networks and systems for power utility automation - Part 7-420: Basic communication structure - Distributed energy resources logical nodes*. IEC, Geneva, Switzerland, 2009.

[126] Roy T Fielding and Richard N Taylor. Principled design of the modern web architecture. *ACM Transactions on Internet Technology (TOIT)*, 2(2):115–150, 2002.

[127] Zukui Li, Ran Ding, and Christodoulos A Floudas. A comparative theoretical and computational study on robust counterpart optimization: I. Robust linear optimization and robust mixed integer linear optimization. *Industrial & engineering chemistry research*, 50(18):10567–10603, 2011.

[128] Evelyn Martin Lansdowne Beale and John A Tomlin. Special facilities in a general mathematical programming system for non-convex problems using ordered sets of variables. In *Proceedings of the Fifth International Conference on Operational Research*, pages 447–454, London, UK, 1970.

[129] Ahmet B Keha, Ismael R de Farias, and George L Nemhauser. Models for representing piecewise linear cost functions. *Operations Research Letters*, 32 (1):44–48, 2004.

[130] Y Wan, M Milligan, and B Kirby. Impact of energy imbalance tariff on wind energy. NREL/CP 500-40663, National Renewable Energy Laboratory (NREL), U.S. Dept. of Energy, July 2007.

[131] Lori Bird, Jaquelin Cochran, and Xi Wang. Wind and solar energy curtailment: Experience and practices in the united states. NREL/TP 6A20-60983, National Renewable Energy Laboratory (NREL), U.S. Dept. of Energy, March 2014.

[132] Juan Rivier Abbad. Electricity market participation of wind farms: the success story of the spanish pragmatism. *Energy Policy*, 38(7):3174 – 3179, 2010.

[133] Michael Joos and Iain Staffell. Short-term integration costs of variable renewable energy: Wind curtailment and balancing in britain and germany. *Renewable and Sustainable Energy Reviews*, 86:45 – 65, 2018. ISSN 1364-0321.

[134] Leonardo Costa. Final proposals for electricity system operator incentives from April 2017. Technical report, Office of Gas and Electricity Markets (Ofgem), U.K., March 2017.

[135] Electricity Market Operation Council. *Electricity Market Operation Rules of Korea*. Korea Power Exchange, November 2020.

[136] Muhammad Qamar Raza, Mithulananthan Nadarajah, and Chandima Ekanayake. On recent advances in pv output power forecast. *Solar Energy*, 136:125–144, 2016. ISSN 0038-092X.

[137] S. Chai, Z. Xu, Y. Jia, and W. K. Wong. A robust spatiotemporal forecasting framework for photovoltaic generation. *IEEE Transactions on Smart Grid*, pages 1–1, 2020.

[138] A. Yona, T. Senjyu, T. Funabashi, and C. Kim. Determination method of insolation prediction with fuzzy and applying neural network for long-term ahead pv power output correction. *IEEE Transactions on Sustainable Energy*, 4(2): 527–533, 2013. ISSN 1949-3037. doi: 10.1109/TSTE.2013.2246591.

[139] F. Wang, Z. Zhang, H. Chai, Y. Yu, X. Lu, T. Wang, and Y. Lin. Deep learning based irradiance mapping model for solar pv power forecasting using sky image. In *Proceedings of the IEEE Industry Applications Society Annual Meeting*, pages 1–9, Baltimore, MD, 2019.

[140] M. Sun, T. Zhang, Y. Wang, G. Strbac, and C. Kang. Using bayesian deep learning to capture uncertainty for residential net load forecasting. *IEEE Transactions on Power Systems*, 35(1):188–201, 2020. ISSN 1558-0679. doi: 10.1109/TPWRS.2019.2924294.

[141] Marc'Aurelio Ranzato, Sumit Chopra, Michael Auli, and Wojciech Zaremba. Sequence level training with recurrent neural networks. In *Proceedings of the International Conference on Learning Representations (ICLR)*, pages 1–16, San Juan, Puerto Rico, 2016.

[142] Alec Radford, Luke Metz, and Soumith Chintala. Unsupervised representation learning with deep convolutional generative adversarial networks. In *Proceedings of the International Conference on Learning Representations (ICLR)*, pages 1–16, San Juan, Puerto Rico, 2016.

[143] X. Mao, Q. Li, H. Xie, R. Y. K. Lau, Z. Wang, and S. P. Smolley. Least squares generative adversarial networks. In *Proceedings of the IEEE International Conference on Computer Vision (ICCV)*, pages 2813–2821, Venice, Italy, 2017.

[144] Martin Arjovsky, Soumith Chintala, and Léon Bottou. Wasserstein generative adversarial networks. In *Proceedings of the 34th International Conference on Machine Learning*, pages 214–223, Sydney, Australia, 2017.

[145] Ishaan Gulrajani, Faruk Ahmed, Martin Arjovsky, Vincent Dumoulin, and Aaron Courville. Improved training of wasserstein gans. In *Proceedings of the 31st International Conference on Neural Information Processing Systems (NIPS)*, page 5769–5779, Long Beach, CA, 2017.

[146] Z. Chen, L. Wu, and Y. Fu. Real-time price-based demand response management for residential appliances via stochastic optimization and robust optimization. *IEEE Transactions on Smart Grid*, 3(4):1822–1831, 2012. ISSN 1949-3061. doi: 10.1109/TSG.2012.2212729.

[147] Y. Zhang, N. Gatsis, and G. B. Giannakis. Robust distributed energy management for microgrids with renewables. In *Proceedings of the International Conference on Smart Grid Communications (SmartGridComm)*, pages 510–515, Tainan, Taiwan, 2012. doi: 10.1109/SmartGridComm.2012.6486036.

[148] J. Choi, Y. Shin, M. Choi, W. Park, and I. Lee. Robust control of a microgrid energy storage system using various approaches. *IEEE Transactions on Smart Grid*, 10(3):2702–2712, 2019. ISSN 1949-3061. doi: 10.1109/TSG.2018.2808914.

[149] Wojciech Zaremba, Ilya Sutskever, and Oriol Vinyals. Recurrent neural network regularization. arXiv:1409.2329, 2014.

[150] Samy Bengio, Oriol Vinyals, Navdeep Jaitly, and Noam Shazeer. Scheduled sampling for sequence prediction with recurrent neural networks. In *Proceed-*

ings of the 28th International Conference on Neural Information Processing Systems (NIPS), pages 1171–1179, Montreal, Canada, 2015.

[151] Ferenc Huszár. How (not) to train your generative model: Scheduled sampling, likelihood, adversary? arXiv:1511.05101, 2015.

[152] Peter J. Huber. Robust estimation of a location parameter. *Annals of Mathematical Statistics*, 35(1):73–101, 1964.

[153] Qingsong Wen, Liang Sun, Xiaomin Song, Jingkun Gao, Xue Wang, and Huan Xu. Time series data augmentation for deep learning: A survey. arXiv:2002.12478, 2020.

[154] K. Greff, R. K. Srivastava, J. Koutník, B. R. Steunebrink, and J. Schmidhuber. LSTM: A search space odyssey. *IEEE Transactions on Neural Networks and Learning Systems*, 28(10):2222–2232, 2017.

[155] Ian J Goodfellow, Jonathon Shlens, and Christian Szegedy. Explaining and harnessing adversarial examples. In *Proceedings of the International Conference on Learning Representations (ICLR)*, pages 1–11, San Diego, CA, 2015.

[156] Adam Paszke, Sam Gross, Francisco Massa, Adam Lerer, James Bradbury, Gregory Chanan, Trevor Killeen, Zeming Lin, Natalia Gimelshein, Luca Antiga, Alban Desmaison, Andreas Kopf, Edward Yang, Zachary DeVito, Martin Raison, Alykhan Tejani, Sasank Chilamkurthy, Benoit Steiner, Lu Fang, Junjie Bai, and Soumith Chintala. Pytorch: An imperative style, high-performance deep learning library. In *Proceedings of the 32nd International Conference on Neural Information Processing Systems (NIPS)*, pages 8024–8035. Curran Associates, Inc., 2019.

[157] Steven Diamond and Stephen Boyd. CVXPY: A Python-embedded modeling language for convex optimization. *Journal of Machine Learning Research*, 17 (83):1–5, 2016.

[158] Martin S Andersen, Joachim Dahl, and Lieven Vandenberghe. CVXOPT: A python package for convex optimization, 2013. URL cvxopt.org.

[159] Andrew Makhorin. GNU linear programming kit, 2012. URL gnu.org/software/glpk/.

초 록

본 논문에서는 전력망 내 에너지자원들의 운영에 있어 안정성과 효율을 향상시키기 위한 통계분석 및 제어분석 방법과 그 결과를 서술한다. 더욱 상세하게는 인공신경망 기반 발전량 예측 결과의 불확정성을 고려한 가상발전소 전력시장 비용 최적화 모델예측제어를 목표로 한다.

제2장에서는 대한민국 전역에 분포한 태양광발전소들의 모니터링 데이터에 대한 분석 결과를 서술한다. 원시 데이터 내에 존재하는 오류들이 목록화되며, 그 원인과 증상에 따라 분류된다. 일반적으로 발생 가능한 데이터 오류들이 통계분석 결과에 미치는 영향을 확인하기 위해, 인공신경망 기반 통계적 태양광발전소 발전량 예측 모델의 성능에 대한 오류 데이터의 영향이 평가된다.

제3장에서는 전력망 내 에너지저장장치에 대한 제어 방법론을 제시한다. 상업용 건물 부하, 태양광발전소 발전, 에너지저장장치 충방전 운전을 포함하는 가상발전소 또는 마이크로그리드가 계량기 후단에 위치한 전력 소비원이자 발전원으로 제시된다. 에너지저장장치를 위한 경제적 급전계획 문제는 혼합정수 선형계획법 형태로 수식화된다. 최적화 목표는 시간대별 요금제하에서 미래 부하와 발전량 예측 불확실성을 고려한 마이크로그리드 경제적 이득 최대화이며, 피크 제어에 대한 목표 역시 보조서비스 형태로 적용 가능하다. 최적화 문제 해결을 통해 도출된 충방전 제어 스케줄은 마이크로그리드 내 부하와 발전량 예측에 대한 불확실성에도 불구하고 경제적 이득을 강건하게 보장할 수 있다.

제4장에서는 특수 조건하에서의 에너지저장장치 하루 전 시간대별 운전 스케줄 도출 방법론을 제시한다. 태양광발전소와 에너지저장장치를 물리적 또는 가상으로 연결한 집합전력자원이 고려된다. 집합전력자원과 전력망 사이의 전력 거래

는 일반적인 시간대별 요금제하에서 이루어진다. 전력망 보조서비스에 해당하는 불균형 요금제가 대한민국 전력시장에서의 분산자원 중개사업자 인센티브 제도 형태로 추가 고려된다. 해당 제도 하에서 집합전력자원은 전일 예측 또는 결정된 운전 스케줄과 실제 스케줄 사이의 오차율에 따라 추가적인 인센티브를 부여받을 수 있다. 집합자원을 위한 에너지관리시스템은 시간대별 요금제와 인센티브 각각에 따른 경제적 이득을 최대화하기 위하여 정확한 예측 기능과 강건한 스케줄 도출 기능을 제공한다.

제안되는 RNN 기반 태양광발전소 발전량 예측 모델은 개방회로 형태의 학습 과정과 폐회로 형태의 사용 방식 사이의 차이를 줄이기 위해 CNN 기반 식별기를 적용한다. 모델 학습 과정에 적용되는 이 GAN 개념은 하루 전 도출한 시간대별 운전 스케줄이 안정적이도록 지원한다. 제안되는 에너지저장장치를 위한 강건 스케줄 도출 모델은 남아있는 예측 오차를 박스 형태의 불확실성 집합으로 처리하여, 도출된 제어 스케줄의 경제적 최적성과 강건성을 보장한다. 스케줄 도출 모델은 간결한 혼합정수 선형계획법 형태로 수식화되어 전력 거래 수익과 인센티브 수익 양쪽 모두를 고려한 빠른 실시간 최적화가 가능하다.

주요어: 에너지관리, 혼합정수 선형계획법, 인공신경망, 비용최적화, 예측, 태양광발전소, 에너지저장장치.

학　번: 2019-30142